Analysis of the upward through-going muons with Kamiokande-III

Takanori Hara
Osaka Univ.

November 20, 1996

Acknowledgements

Prof. Y.Nagashima moved me into particle physics and gave me a chance to participate in Kamiokande experiment. Also he taught me a lot of common sense inside physics. I would like to express my great appreciation to him.

I gratefully acknowledge the helpful advice of Prof. T.Yamanaka, Prof. J.Haba and Dr. M.Hazumi. They always supported and encouraged me.

I am deeply idebted to Prof. Y.Totsuka for his valuable advice. I learned the essence of experiment and an attitude toward physics from him.

I wish to thank Prof. K.Nakamura, Prof. Y.Suzuki and Prof. T.Kajita. Their many suggestions were very useful for me.

Prof. M.Nakahata and Dr. K.Inoue gave me instructions for using the computer at the experimental site, Kamioka. I am particularly grateful to them cordially.

I would like to thank Prof. A.Suzuki for a lot of useful discussions.

I must also thank all the other Kamiokande-III collaborators for their help with the experiments. Paricular thanks go to Prof. M.Mori and Dr. Y.Oyama. They helped me on many aspects. Without their supports, I could not accomplish my analysis.

I owe thanks to my colleagues Dr. H.Hanai, Y.Yamamoto, A.Sakai, T.Ishizuka, M.Koga, S.Hatakeyama and wish to express my gratitude to Dr. T.Nakaya. They gave me useful discussions and supported me on various occasions.

My thanks go to D.Tatsumi and other graduate students in Nagashima group. Especially, I wish to express my deeply appreciation to T.Yamaguchi and A.Kusano. They always cared about me and assisted with my analysis.

I thank the cooperation of Kamioka Mining and Smelting Company.

At the last, I would like to express my great thanks to Dr. M.Takita. He taught me physics, statistics, hardware and software and I learned from him the whole of the experiments. I will never forget his kindness and useful instructions.

Abstract

The flux and its zenith angular dependence of the upward through-going muons (with its track length longer than 7 m) produced in the surrounding rock layers near the detector by atmospheric neutrinos is measured by the Kamiokande detctor. A total of 373 events are observed, of which 185 events and 188 events are recorded during Kamiokande-II (1115 days) and Kamiokande-III (1332 days) experimental periods, respectively. It is found that the zenith angle dependence of the observed upward through-going muons is consistent with the assumption of neutrino oscillation (Honda's atmospheric neutrino flux and CTEQ parton distribution model are used). The result agrees well with previous analysis made by Kamiokande using "contained events". Furthermore, the observed average flux is evaluated to be $\Phi_{obs} = (1.98 \pm 0.10(\text{stat}) \pm 0.03(\text{exp.sys})) \times 10^{-13}\text{cm}^{-2}\text{s}^{-1}\text{sr}^{-1}$, which is compared to an expected value of $\Phi_{theo} = (2.20^{+0.39}_{-0.34}) \times 10^{-13}\text{cm}^{-2}\text{s}^{-1}\text{sr}^{-1}$. The observation is in apparent agreement with the prediction, but it requires more studies to reduce the theoretical uncertainty.

Contents

Chapter 1

Introduction

1.1 Atmospheric neutrinos

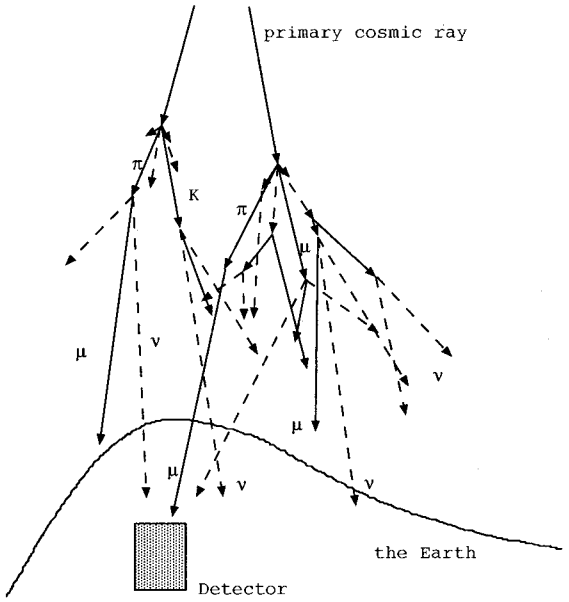

Figure 1.1: Schematic view of atmospheric neutrino production mechanism

The earth is continuously bombarded by primary cosmic rays, i.e., protons and nuclei. When they reach the Earth's atmosphere, they interact with its costituents particles, creating a shower of pions and kaons. A charged pion decays into a muon and a muon neutrino. The muon, in turn, decays in flight into an electron, at the same time producing another muon neutrino and an electron neutrino. Thus, a typical neutrino production mechanism maybe illustrated as follows.

$$
\begin{array}{lllllll}
p & + & N & \longrightarrow & p & + & N' + \pi^+ \\
 & & & & & & \downarrow \\
 & & & & & & \mu^+ + \nu_\mu \\
 & & & & & & \downarrow \\
 & & & & & & e^+ + \overline{\nu}_\mu + \nu_e
\end{array}
$$

A kaon produced by primary cosmic rays also decays, and generates neutrinos similarly.

$$K^+ \longrightarrow \mu^+ \quad \nu_\mu$$

$$K_L^0 \longrightarrow \pi^- \quad \mu^+ \quad \nu_\mu$$
$$\pi^+ \quad \mu^- \quad \overline{\nu}_\mu$$
$$\pi^- \quad e^+ \quad \nu_e$$
$$\pi^+ \quad e^- \quad \overline{\nu}_e$$

As is easily seen, typically two muon neutrinos are created for each electron neutrino. So the ratio of muon neutrinos to electron neutrinos is roughly $\nu_\mu + \overline{\nu}_\mu : \nu_e + \overline{\nu}_e = 2 : 1 \lesssim 1$ GeV[1] This ratio increases with the energy reaching about 10 : 1 at 100 GeV. This is because energetic muons reach the surface of the earth before they decay and are absorbed in the Earth.

1.2 Outstanding problem of the atmospheric neutrino

A detector to observe the atmospheric neutrinos is typically placed deep underground. The neutrinos, interacting weakly with the matter, reach the detector easily while all other particles are mostly absorbed in the Earth. When they reach the detector, some of them interact with the material inside the detector producing electrons or muons. They either escape or stop inside. Those that range out and stop inside the detector (see Fig. 1.2) shall be called "fully-contained events" hereafter. The typical energy of the neutrinos which cause fully-contained events are about 1 GeV. When the produced electrons and muons escape from the detector as shown in Fig. 1.3, they shall be called "partially-contained events". In this case, the mean energy of parent neutrinos is $\sim$ 10 GeV.

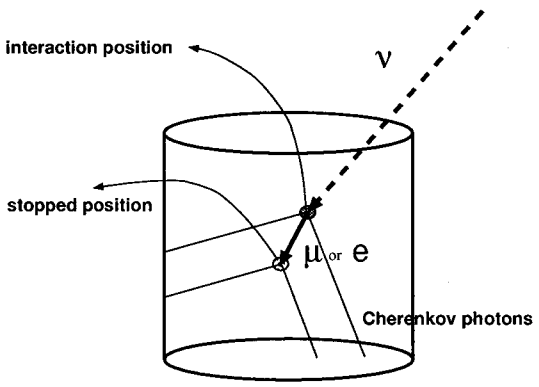

Figure 1.2: Schematic view of a "fully-contained event"

In 1988, Kamiokande group observed a smaller $(\nu_\mu + \overline{\nu}_\mu)/(\nu_e + \overline{\nu}_e)$ ratio[2] than the expected value in fully-contained events [5], [6]. This discrepancy was later confirmed by another experiments IMB [7], [8]

[1]The K/π ratio is about 0.1 at this energy range and muons produced in K decay can also decay in flight. The contribution of ν_e or $\overline{\nu}_e$ directly generated from K is only $\sim$3 % [1].

[2]In the case of the absolute value of $(\nu_\mu + \overline{\nu}_\mu)$ or $(\nu_e + \overline{\nu}_e)$, the total error is estimated as 15 %$\sim$20 % at $E_\nu \sim$1 GeV. Furthermore, the observation is also affected by the uncertainty of the neutrino cross section and the consequent uncertainty is estimated as 25 %$\sim$30 %. Therefore, the experimental data are in agreement with the theoretical value. However, in the case of the $(\nu_\mu+\overline{\nu}_\mu)/(\nu_e+\overline{\nu}_e)$ ratio is not affected by the uncertainty of primary fluxes and models of meson production. And the uncertainty of neutrino cross section is canceled out. The error is estimated $\lesssim$5 % below 30 GeV for $(\nu_\mu + \overline{\nu}_\mu)/(\nu_e + \overline{\nu}_e)$ [2], [3], [4].

and Soudan II [9]. While some other groups saw apparently no discrepancy (Fréjus [10] and Nusex [11]), they suffer from poor statistics and/or large systematic errors (summarized in Table 1.1).

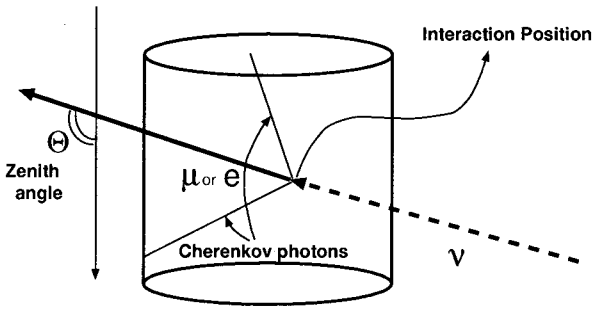

Figure 1.3: Schematic view of the "partially-contained event"

Recently, this ratio was remeasured by the Kamiokande experiment using partially-contained events [12]. The observed $(\nu_\mu + \overline{\nu}_\mu)/(\nu_e + \overline{\nu}_e)$ ratio is again smaller than expected. The discrepancy is called "atmospheric neutrino problem" and is the main theme of the present thesis.

Important features of these results are

- At low energies ($E_\nu \sim 1$ GeV), the observed ratio, $(\nu_\mu+\overline{\nu}_\mu)/(\nu_e+\overline{\nu}_e)$, is smaller than the expectation. This result indicates either a deficit in $(\nu_\mu + \overline{\nu}_\mu)$ or abnormal excess in flux of $(\nu_e + \overline{\nu}_e)$.
- At middle energies ($E_\nu \sim 10$ GeV), the observed ratio is also smaller than the expected value. The zenith angle distribution of $(\nu_\mu + \overline{\nu}_\mu)/(\nu_e + \overline{\nu}_e)_{data}/(\nu_\mu + \overline{\nu}_\mu)/(\nu_e + \overline{\nu}_e)_{theo}$ suggests possible neutrino oscillations[3] or some yet-unknown new physics. Here, the zenith angle, Θ, is the muon incident angle relative to the detector and the downward direction is given by $\cos\Theta = 1$.

They are summarized in Table 1.1.

Experiment	$(\nu_\mu + \overline{\nu}_\mu)/(\nu_e + \overline{\nu}_e)_{data}/(\nu_\mu + \overline{\nu}_\mu)/(\nu_e + \overline{\nu}_e)_{theo.}$
Kamiokande	$0.60^{+0.07}_{-0.06} \pm 0.05$
	$0.57^{+0.08}_{-0.07} \pm 0.07^a$
IMB	$0.54 \pm 0.05 \pm 0.12$
Soudan II	$0.69 \pm 0.19 \pm 0.09$
Nusex	$0.99^{+0.35}_{-0.25}$
Fréjus	$0.87 \pm 0.16 \pm 0.08^a$
	$1.06 \pm 0.18 \pm 0.15$

Table 1.1: Results on contained-event analysis of various experiments. Ratios with a superscript a are obtained from partially-contained event analysis and the others derived from fully-contained events.

1.3 Motivation of this thesis

Having observed the discrepancy in both fully-contained and partially-contained events, the next logical step is to investigate "through-going muons", namely those that are produced by neutrinos of

[3] $\nu_\mu \leftrightarrow \nu_x$ oscillations are discussed in section 1.5, 1.6.

even higher energy. However, not all through-going muons are of neutrino origin. Some of them are components of cosmic rays directly produced in the atmosphere as described in Section 1.1. Therefore, we classify through-going muons into several categories (see Fig. 1.4).

Energetic atmospheric ν_μ or $\overline{\nu}_\mu$ traveling through the Earth interacts with rock layers surrounding the detector and produce muons. Muons heading upward are defined as "upward-going muons" and those going downward as "downward-going muons" (④, ③ in Fig. 1.4). Though neutrino induced muons can be observed with the detector, downward-going muons are difficult to differentiate from cosmic-ray muons (①). On the contrary, upward-going muons can be considered neutrino induced, since the flux of the cosmic-ray going upward is negligible (②).

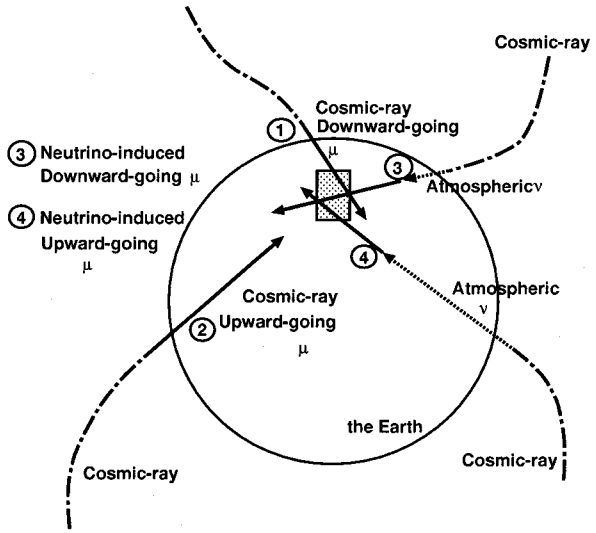

Figure 1.4: Various types of muons and neutrino-induced events.

From now on, we define "upward-going muons" as neutrino-induced upward-going muons (④). Those energetic enough to pass through the detector (see Fig. 1.5) are defined as "upward through-going muons". The mean energy of the parent neutrino producing them is roughly 100 GeV.

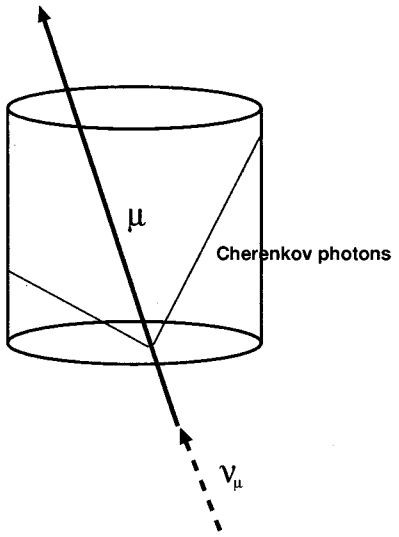

Figure 1.5: Schematic view of the "upward through-going muon event".

If $\nu_\mu \leftrightarrow \nu_x$ oscillations is the origin of the atmospheric neutrino problem, the flux of ν_μ will change as a function of the propagation length (L) and the energy (E_ν). Though the observed data suggests possible neutrino oscillation at $E_\nu \lesssim 10$ GeV, it is unknown whether the ν_μ flux decrease at higher energies or not. Therefore the experimental ν_μ flux at high energy region needs to be studied. Upward through-going muons are useful to search for neutrino oscillations at high energy regions which are not detectable by means of contained events. The zenith angle distribution of upward through-going muons is specially sensitive to the neutrino oscillation, since the propagation length changes with the zenith angle (10 km$\lesssim L \lesssim$13000 km). It is very important to examine a possible distortion of the zenith angle distribution.

1.4 Mass and mixing of the neutrino

In this world, the matter is composed of quarks and leptons which are classified into three generations or families by their flavor as is shown in Table 1.2.

	1st generation	2nd generation	3rd generation
quarks	u	c	t
	d	s	b
leptons	e	μ	τ
	ν_e	ν_μ	ν_τ

Table 1.2: Generations of fermions

Among the matter, there exist four types of fundamental interactions which consist of gravitational, elecromagnetic, weak and strong interactions. They are mediated by gauge bosons which are shown in Table 1.3.

Interaction	Gravitational	Electromagnetic	Weak	Strong
Gauge boson	graviton	γ	$W^\pm, Z^0$	g
Spin-parity	2^+	1^-	1^-,1^+	1^-
Mass (GeV)	0	0	80$\sim$90	0
Range (m)	∞	∞	10^{-18}	$\leq 10^{-15}$

Table 1.3: Classification of the gauge bosons

All fermions (matter constituents) except the neutrinos which come in three species as shown in Table 1.2 are now known to have finite masses. Many experiments have attempted to measure neutrino masses, but so far none have succeed to establish a finite value solidly.

	m_{ν_e}	m_{ν_μ}	m_{ν_τ}
mass	$<$ 7.2 eV	$<$ 160 keV	$<$ 24 MeV

Table 1.4: The best bound of m_ν

The most stringent upper limit on the ν_e mass, $m_{\nu_e} < 7.2$eV(95%C.L.) [13], was derived from precision measurements of the end-point energy spectrum of tritium β-decay. The best bound on $m_{\nu_\mu} < 160$ keV

at 90%C.L. [14] comes from measurements of the momentum of muons produced in the decay of pions at rest. In the case of m_{ν_τ}, the mass limit $m_{\nu_\tau} < 24$ MeV was obtained by analyzing the invariant mass spectrum of the decay products in $\tau^- \rightarrow 3\pi^- 2\pi^+ \nu_\tau$ [15]. (summarized in Table 1.4)

Observed neutrinos, ν_l ($l = e, \mu, \tau$), are called flavor eigenstates. They are not necessarily identical to mass eigenstates ν_i (i=1,2,3). If they are different, the neutrino flavor eigenstates are described by superpositions of different neutrino mass eigenstates.

$$\nu_l = \sum U_{li} \nu_i \tag{1.1}$$

Where U_{li}'s are unitary matrix elements and their equivalent in the quark sector is called Kobayashi-Maskawa matrix [16]. In the two flavor mixing case, for example ν_e and ν_μ, the mixing scheme becomes simpler and is described as follows,

$$\begin{pmatrix} \nu_e \\ \nu_\mu \end{pmatrix} = U \begin{pmatrix} \nu_1 \\ \nu_2 \end{pmatrix} = \begin{pmatrix} \cos\theta & \sin\theta \\ -\sin\theta & \cos\theta \end{pmatrix} \begin{pmatrix} \nu_1 \\ \nu_2 \end{pmatrix} \tag{1.2}$$

where $\sin\theta$ ($0 \leq \theta \leq \pi/2$) is the mixing strength between flavor eigenstates ν_e and ν_μ in the weak interaction.

From now on, we restrict our discussion to the two flavor mixing case. The reason is simplicity, but is a common practice in this field.

1.5 Neutrino oscillation

If the neutrinos ($\nu_l; l = e, \mu, \tau$) produced in the weak interaction are superpositions of mass-eigenstate neutrinos ($\nu_i; \nu_1, \nu_2, \nu_3$) with the non-degenerate masses of m_{ν_i}, flavor-eigenstate neutrinos will evolve in time, leading to neutrino oscillations from one flavor to another. The possibility of neutrino oscillation was proposed in 1960's by Maki [17] and Pontecorvo [18]. The deficit of flux could result if only one species of the neutrino is observed. This is a possible explanation of the atmospheric neutrino anomaly.

Neutrino oscillations (in two flavor mixing) are in general characterized by one mixing strength $\sin^2 2\theta_v$[†] between flavor eigenstates ν_e and ν_μ in the weak interaction, and one mass difference squared $\Delta m^2 (= m_2^2 - m_1^2)$ between neutrino mass eigenstates ν_1 and ν_2.

From Eq. 1.2, the wave functions of the flavor eigenstates are represented as,

$$|\nu_e\rangle = \cos\theta_v |\nu_1\rangle + \sin\theta_v |\nu_2\rangle \tag{1.3}$$

$$|\nu_\mu\rangle = -\sin\theta_v |\nu_1\rangle + \cos\theta_v |\nu_2\rangle \tag{1.4}$$

Time evolution of a state $|\nu(t)\rangle$ with momentum p_ν may be written as a superposition of $|\nu_e\rangle$ and $|\nu_\mu\rangle$,

$$|\nu(t)\rangle = \nu_e(t)|\nu_e\rangle + \nu_\mu(t)|\nu_\mu\rangle \tag{1.5}$$

Here, the time evolution of mass eigenstates can be written as,

$$|\nu_i(t)\rangle = |\nu_i(0)\rangle e^{-iE_i t}, \quad i = 1 \text{ or } 2 \tag{1.6}$$

[†]The suffix v is attached to θ in order to differentiate vacuum oscillation from matter oscillation to be described later.

The propagation in space-time of flavor eigenstates is determined by the Schrödinger equation. Using Eq. 1.3, Eq. 1.4 and Eq. 1.6, ν_e and ν_μ obey the following equation;

$$\begin{aligned} i\frac{d}{dt}\begin{pmatrix}\nu_e\\ \nu_\mu\end{pmatrix} &= \begin{pmatrix}\cos\theta_v & \sin\theta_v\\ -\sin\theta_v & \cos\theta_v\end{pmatrix} i\frac{d}{dt}\begin{pmatrix}\nu_1\\ \nu_2\end{pmatrix} \\ &= \begin{pmatrix}\cos\theta_v & \sin\theta_v\\ -\sin\theta_v & \cos\theta_v\end{pmatrix}\begin{pmatrix}E_1 & 0\\ 0 & E_2\end{pmatrix}\begin{pmatrix}\cos\theta_v & -\sin\theta_v\\ \sin\theta_v & \cos\theta_v\end{pmatrix}\begin{pmatrix}\nu_e\\ \nu_\mu\end{pmatrix} \end{aligned} \tag{1.7}$$

One can subtract $(E_1+E_2)/2$ multiple of the unit matrix from Eq. 1.7, since it will not change $|\nu_e|^2$ and $|\nu_\mu|^2$. Besides, for the ultra-relativistic neutrinos, an approximation, $E_i \simeq p_\nu + m_i^2/2p_\nu$ (i =1 or 2) could be applied. Doing this to make the matrix traceless gives;

$$i\frac{d}{dt}\begin{pmatrix}\nu_e\\ \nu_\mu\end{pmatrix} = \begin{pmatrix} -\left(\frac{\pi}{L_v}\right)\cos 2\theta_v & \left(\frac{\pi}{L_v}\right)\sin 2\theta_v \\ \left(\frac{\pi}{L_v}\right)\sin 2\theta_v & \left(\frac{\pi}{L_v}\right)\cos 2\theta_v \end{pmatrix}\begin{pmatrix}\nu_e\\ \nu_\mu\end{pmatrix} \tag{1.8}$$

$$\equiv M_v\begin{pmatrix}\nu_e\\ \nu_\mu\end{pmatrix} \tag{1.9}$$

where M_v is defined as the mass matrix and $L_v = 4\pi p_\nu/|\Delta m^2|$ is called the vacuum oscillation length. Time evolution of $|\nu_e(t)\rangle$ and $|\nu_\mu(t)\rangle$ can be derived by solving the differential equation Eq. 1.9 under the initial condition $\nu_e(0)=1$, $\nu_\mu(0)=0$ at t=0. The solutions are,

$$|\nu_e(t)\rangle = \left\{\cos 2\theta_v \sin\left(\frac{\pi}{L_v}\right)t + i\cos\left(\frac{\pi}{L_v}\right)t\right\}\nu_e(0) + \left\{\sin 2\theta_v \sin\left(\frac{\pi}{L_v}\right)t\right\}\nu_\mu(0) \tag{1.10}$$

$$|\nu_\mu(t)\rangle = -\left\{\sin 2\theta_v \sin\left(\frac{\pi}{L_v}\right)t\right\}\nu_e(0) + \left\{\cos 2\theta_v \sin\left(\frac{\pi}{L_v}\right)t - i\cos\left(\frac{\pi}{L_v}\right)t\right\}\nu_\mu(0) \tag{1.11}$$

The probability, P_v, that a neutrino born as ν_e at the source remains ν_e at a distance $L(\simeq ct$, c ; light velocity) is

$$P_v(\nu_e \to \nu_e) = |\langle\nu_e(0)|\nu_e(t)\rangle|^2 = 1 - \sin^2 2\theta_v \sin^2\left(\frac{\pi L}{L_v}\right) \tag{1.12}$$

Alternatively this is expressed as;

$$P_v(\nu_e \to \nu_e) = 1 - \sin^2 2\theta_v \sin^2\left(\frac{1.27\Delta m^2 L}{p_\nu}\right) \tag{1.13}$$

$$L_v = 2.48\text{km}\left(\frac{p_\nu}{1\text{GeV/c}}\right)\left(\frac{\Delta m^2}{1\text{eV}^2}\right)^{-1} \tag{1.14}$$

where the mass difference squared Δm^2 and momentum p_ν are expressed in unit of $(\text{eV})^2$ and GeV/c, respectively.

It should be noted that the above formulae are also valid for neutrino oscillations between antineutrinos under the assumption of the CP invariance.

In the case $L \gg L_v$, in other words if $\Delta m^2 \gg p_\nu/L$, the value of $\sin^2\left(\frac{1.27\Delta m^2 L}{p_\nu}\right)$ averages out to $\sim 1/2$ because of violent oscillation. In this case the experiment can decide the value of $\sin^2 2\theta_v$. When $L \ll L_v$ or when $\Delta m^2 \ll p_\nu/L$, the probability is expressed as a function of $\sin^2 2\theta_v\left(\frac{1.27\Delta m^2 L}{p_\nu}\right)$, hence

for large mixing angle of $\sin^2 2\theta_v \approx 1$, the experiment can explore small Δm^2 region governed by the value of p_ν/L.

In the case of underground experiments, taking $L \simeq 13000$ km (diameter of the earth) and $p_\nu \sim 1$ GeV (typical momentum of atmospheric neutrinos), Δm^2 region of down to 10^{-4} eV^2 for large mixing angle can be explored (see also Table 1.5).

1.6 Matter oscillation

When neutrinos propagate through matter, ν_e behavior is different from ν_μ or ν_τ. Neutral current interactions caused by Z^0 exchange occur to every flavor neutrino. However, only ν_e have charged current interactions due to W exchange with the electrons which exist aplenty in normal matter (see Fig. 1.6).

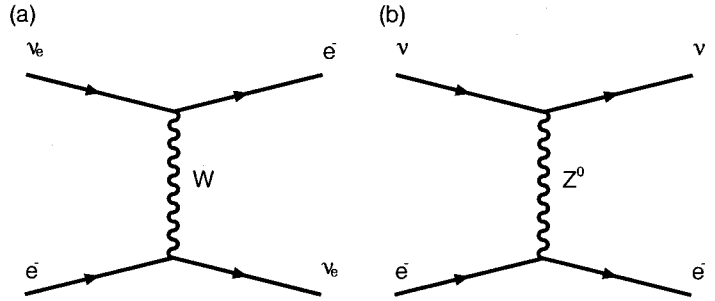

Figure 1.6: Charged current and neutral current interactions of ν

As noted by Wolfenstein [19], neutrino oscillations in matter can be affected by these interactions. Furthermore, Mikheyev and Smirnov suggested that this effect should significantly enhance neutrino oscillation when the resonance conditions in matter are satisfied, even if the intrinsic mixing angle, $\sin^2 2\theta_v$, is quite small [20]. This effect is called "MSW"(Mikheyev-Smirnov- Wolfenstein) effect and is active only on $\nu_e \leftrightarrow \nu_\mu$ or $\nu_e \leftrightarrow \nu_\tau$ oscillations but never on $\nu_\mu \leftrightarrow \nu_\tau$ oscillation.

In the following, the $\nu_e \leftrightarrow \nu_\mu$ matter oscillation will be discussed. Formulae in $\nu_e \leftrightarrow \nu_\tau$ matter oscillation can be obtained simply by replacing appropriate variables. In matter, the flavor eigenstates ν_e and ν_μ are expressed in terms of two mass eigenstates, ν_{1m} and ν_{2m}, analogously to Eq. 1.3 and Eq. 1.4.

$$|\nu_e\rangle = \cos\theta_m|\nu_{1m}\rangle + \sin\theta_m|\nu_{2m}\rangle \tag{1.15}$$

$$|\nu_\mu\rangle = -\sin\theta_m|\nu_{1m}\rangle + \cos\theta_m|\nu_{2m}\rangle \tag{1.16}$$

where the parameter θ_m is the effective mixing angle in matter.

An analogue of Schrödinger equation Eq. 1.8 can be written as,

$$i\frac{d}{dt}\begin{pmatrix}\nu_e\\ \nu_\mu\end{pmatrix} = \begin{pmatrix} -\left(\frac{\pi}{L_m}\right)\cos 2\theta_m & \left(\frac{\pi}{L_m}\right)\sin 2\theta_m \\ \left(\frac{\pi}{L_m}\right)\sin 2\theta_m & \left(\frac{\pi}{L_m}\right)\cos 2\theta_m \end{pmatrix}\begin{pmatrix}\nu_e\\ \nu_\mu\end{pmatrix} \tag{1.17}$$

where, L_m is defined as oscillation length in matter. These processes are just the same as described in the previous section.

Alternatively, the evolution equation in matter can be expressed as

$$i\frac{d}{dt}\begin{pmatrix}\nu_e\\ \nu_\mu\end{pmatrix} = [M_v + R_m]\begin{pmatrix}\nu_e\\ \nu_\mu\end{pmatrix} \tag{1.18}$$

where R_m represents an additional potential in matter induced by ν_e-e charged current interaction and M_v is the vacuum oscillation matrix defined in Eq. 1.9. R_m could be written as

$$R_m = \begin{pmatrix}\pm\sqrt{2}GN_e(x) & 0\\ 0 & 0\end{pmatrix}, \qquad x = ct \tag{1.19}$$

where $N_e(x)$ is the electron density in the matter, G is the Fermi coupling constant. A plus sign and a minus sign correspond to $\nu_e - e^-$ and $\overline{\nu}_e - e^-$ case, respectively [19].

Transforming the matrix in its traceless form as Eq. 1.9;

$$i\frac{d}{dt}\begin{pmatrix}\nu_e\\ \nu_\mu\end{pmatrix} = \begin{pmatrix} -\left(\frac{\Delta m^2}{4p_\nu}\right)\cos 2\theta_v \pm \frac{GN}{\sqrt{2}} & \left(\frac{\Delta m^2}{4p_\nu}\right)\sin 2\theta_v \\ \left(\frac{\Delta m^2}{4p_\nu}\right)\sin 2\theta_v & \left(\frac{\Delta m^2}{4p_\nu}\right)\cos 2\theta_v \mp \frac{GN}{\sqrt{2}}\end{pmatrix}\begin{pmatrix}\nu_e\\ \nu_\mu\end{pmatrix} \tag{1.20}$$

Comparing this matrix with Eq. 1.17, L_m and $\sin^2 2\theta_m$ are given as below,

$$L_m = \frac{L_v}{\sqrt{1 \mp 2\left(\frac{L_v}{L_0}\right)\cos 2\theta_v + \left(\frac{L_v}{L_0}\right)^2}} \tag{1.21}$$

$$\sin^2 2\theta_m = \frac{\sin^2 2\theta_v}{\sin^2 2\theta_v + (L_v/L_0 \mp \cos 2\theta_v)^2} \tag{1.22}$$

$$L_0 = 2\pi/\sqrt{2}GN = 1.624 \times 10^4 \mathrm{km}/\rho \tag{1.23}$$

where $\rho = N/(6.02 \times 10^{23})$ is the electron density in unit of Avogadro's number per cm^3.

The probability that a neutrino born as ν_e at the source remains ν_e at a distance L considering the matter effect, $P_m(\nu_e \to \nu_e)$, is written in a similar form to Eq. 1.12 in vacuum;

$$P_m(\nu_e \to \nu_e) = 1 - \sin^2 2\theta_m \sin^2\left(\frac{\pi L}{L_m}\right) \tag{1.24}$$

This formula, however, is valid only in a region where the matter density is approximately constant. The complicated shape of the terrestrial density, as shown in Fig. 1.7, prevents an analytical approach to the solution of Eq. 1.18. Therefore, the equation is numerically solved by computer techniques.

Assuming Δm^2 is positive[4], Eq. 1.22 shows that the neutrino mixing is enhanced for neutrinos at $L_v/L_0 = \cos 2\theta_v$, in other words, when the resonance condition is satisfied, even if the intrinsic mixing strength, $\sin^2 2\theta_v$, is small. This is the key point of the MSW effect. Numerically this resonance condition is written as

$$1.53 \times 10^{-4} \times \frac{P(\mathrm{GeV/c}) \cdot \rho(/\mathrm{cm}^3)}{\Delta m^2(\mathrm{eV}^2)} = \cos 2\theta_v \tag{1.25}$$

On the contrary, the MSW effect always suppresses antineutrino oscillation for $\Delta m^2 > 0$.

[4]In general, mass of a particle belonging to 1st generation is lighter than that of 2nd generation. So we can easily assume that ν_e mass is lighter than ν_μ mass, if neutrino has finite mass. Furthermore, it is natural to presume that mass eigenstates $\nu_i;(\nu_1,\nu_2,\nu_3)$ roughly correspond to flavor eigenstates $\nu_l;(\nu_e,\nu_\mu,\nu_\tau)$, i.e. $\nu_1 \simeq \nu_e$, $\nu_2 \simeq \nu_\mu$. Therefore, $\Delta m^2 (= m_2^2 - m_1^2)$ is assumed to be positive in this thesis.

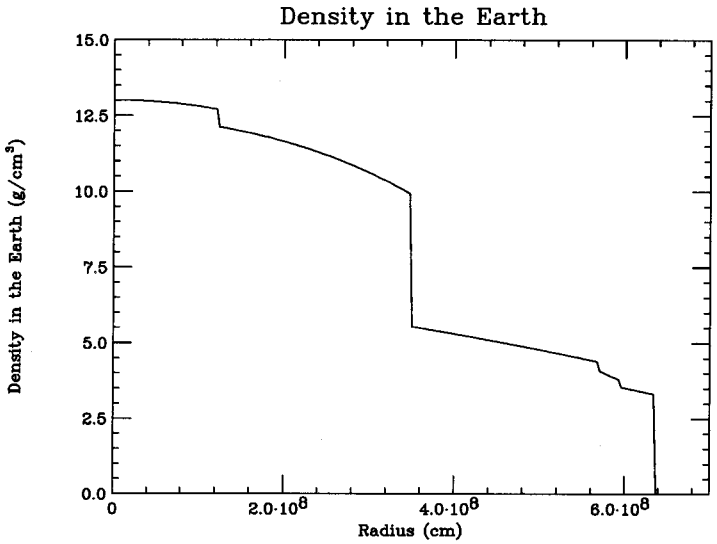

Figure 1.7: The radial distribution of terrestrial density

1.7 Present experimental status of neutrino oscillations

Many experiments are carried out to search for neutrino oscillations using various neutrino sources. As is clear from Eq. 1.12 and Eq. 1.24, one of the parameters which judges the sensitivity of an experiment to neutrino oscillations is L/p_ν. The experimental condition is optimal if $\Delta m^2 L/p_\nu \simeq O(1)$. In other words, for exploring lower neutrino masses, one needs a longer L and a smaller p_ν, keeping a reasonable counting rate. Various neutrino sources are summarized in Table 1.5, together with the typical observation distance L which can be achieved, and the typical mass difference squared Δm^2 to which they are sensitive (Assuming the best possible experimental conditions, small statistical errors or large mixing angles).

ν source			E_ν (MeV)	L (m)	Δm^2 (eV^2)
Artificial Neutrino Source	=	Reactor($\overline{\nu}_e$)	1	10^2	10^{-2}
		Meson Factory($\nu_e, \nu_\mu, \overline{\nu}_\mu$)	40	10^2	10^{-1}
		Accelerator($\nu_\mu, \overline{\nu}_\mu$)	10^3	10^4	10^{-1}
Natural Neutrino Source	=	Atmospheric($\nu_e, \overline{\nu}_e, \nu_\mu, \overline{\nu}_\mu$)	$10^3 \sim 10^5$	10^7	$10^{-4} \sim 10^{-2}$
		Solar[5](ν_e)	$0.1 \sim 10$	10^{11}	$10^{-12} \sim 10^{-10}$

Table 1.5: Sensitivity of various neutrino sources to neutrino oscillations

Regarding the $\nu_e \leftrightarrow \nu_\mu$ oscillation, reactor experiments excluded $10^{-2} \lesssim \Delta m^2 \lesssim 10^{-1}\text{eV}^2$ [21]. Although accelerator experiments are less sensitive to low mass region than those by reactors and have not quite reached the region around $\Delta m^2 < 10^{-2}\text{eV}^2$, $\nu_e \leftrightarrow \nu_\mu$ appearance experiments have achieved sensitivities to $\sin^2 2\theta_v$ values much smaller ($\sim 3 \times 10^{-3}$) than those reached at reactors ($\gtrsim 10^{-1}$) [22], [23], [24], [25], [26].

All the solar neutrino experiments have reported a deficit in solar neutrino flux compared with theoretical predictions in astrophysics [27], [28], [29], [30]. In other words, the solar neutrino experiments provide indications in favor of neutrino oscillations. Interpretation of the deficit in solar neutrino flux as

[5]Solar neutrinos are produced in the fusion reactions inside the sun.

due to vacuum oscillation gives a sensitive Δm^2 region listed in Table 1.5. Use of $\nu_e - \nu_\mu$ matter oscillation allows us to give constraints on different Δm^2 region and very small mixing strength ($\sin^2 2\theta_v \gtrsim 10^{-3}$). Combination of the past solar neutrino experiments left two allowed regions in $\Delta m^2 - \sin^2 2\theta_v$ plane. One is $\Delta m^2 \sim 10^{-5}$, $\sin^2 2\theta_v \sim 10^{-2}$ and the other is $\Delta m^2 \sim 10^{-5}$, $\sin^2 2\theta_v \sim 0.8$, shown in Fig. 1.8(a).

In the case of $\nu_\mu \leftrightarrow \nu_\tau$ oscillations, searches for ν_μ disappearance are made by experiments at meson factories [31], [32], which give negative results. The best constraint on $\sin^2 2\theta_v$ is obtained by the accelerator experiment [33]. The $\nu_\mu \leftrightarrow \nu_\tau$ oscillation can not be searched for by either reactor experiments or the solar neutrino experiments, because neutrinos used as source consists only of $\overline{\nu}_e$ or ν_e, respectively (see Table. 1.5).

There is a gap in Δm^2 around $10^{-2} \sim 10^{-3}\mathrm{eV}^2$ that can be accessed by neither accelerator experiments nor solar neutrino observations. The atmospheric neutrino is in a unique position to cover this region.

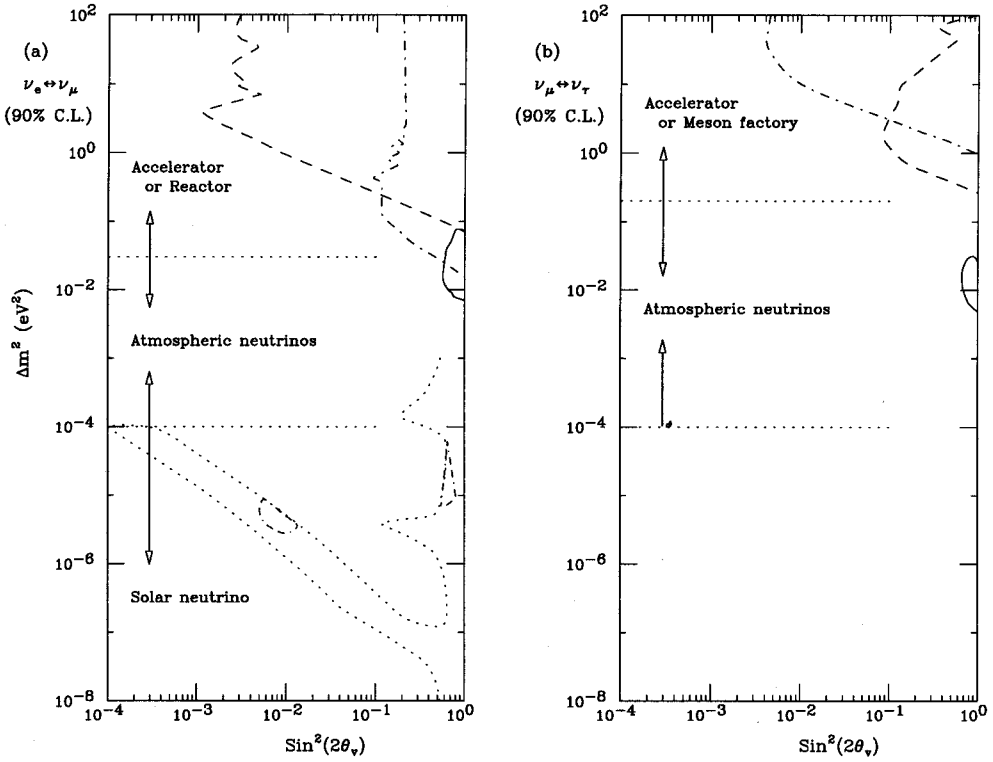

Figure 1.8: Present experimental status of neutrino oscillations. (a):$\nu_e \leftrightarrow \nu_\mu$ oscillation and (b):$\nu_\mu \leftrightarrow \nu_\tau$ oscillation. For (a), the dashed, dot-dashed and dotted lines are derived from accelerator, reactor and solar neutrino experiments. Two areas inside the dot-dash-dashed line are the allowed regions derived from solar neutrino experiments. The solid line in the atmospheric neutrino region corresponds to contained events' result. For (b), the dot-dashed, dashed and solid line correspond to the accelerator, the meson factory and the atmospheric neutrino experiments. The $\nu_\mu \leftrightarrow \nu_\tau$ oscillation can not be explored by the solar neutrino experiments.

Chapter 2

The Kamiokande-III detector

2.1 Ring-imaging water Cherenkov detector

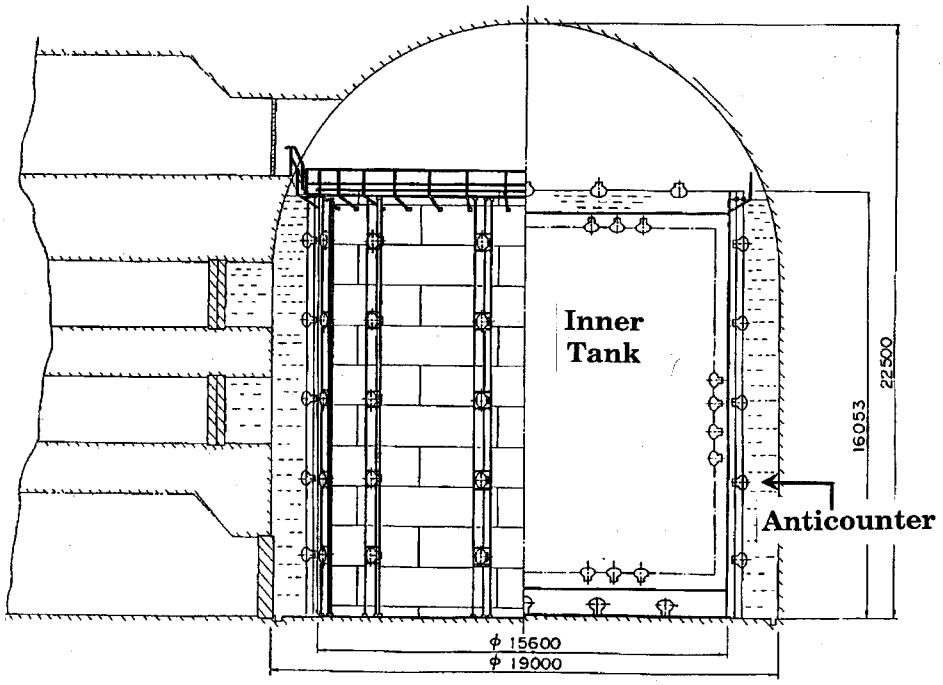

Figure 2.1: Schematic view of the Kamiokande-III detector

The Kamiokande-III detector is an upgraded version of the Kamiokande detector which is originally built to detect proton decays. The experimental site of the Kamiokande-III is located 1000 m (2700 meters of water equivalent) underground in the Kamioka mine of Gifu prefecture at 36.42°N, 137.31°E (25.8°N in geomagnetic latitude), about 250 km west of Tokyo in Japan.

The underground site was chosen to reduce the cosmic-ray background. The cosmic-ray background at sea level ($\sim$ 1 event/cm^2/min) is very serious for both trigger system and subsequent off-line analysis.

The Kamiokande-III detector is a cylindrical large ring-imaging water Cherenkov calorimeter as shown in Fig. 2.1. A ring-imaging water Cherenkov detector detects Cherenkov lights emitted in a massive detector volume of water by charged particles, with photomultiplier tubes (PMTs). In a steel tank 15.6 mϕ (in diameter) $\times$ 16 m (in height), a total amount of 3000 metric tons of water are contained. It is

composed of an inner detector and an outer anticounter. The inner main detector is 14.4 m in diameter $\times$ 13.1 m in height, which contains 2142 metric tons of water. A total of 947 photomultiplier tubes (PMTs) of 50 cm in diameter are mounted on the tank walls. The PMTs are arrayed 2-dimensionally facing inward on the tank surfaces with density of 1 PMT/1 m^2 on the top and bottom planes and 1 PMT/0.945 m^2 on the barrel of the inner detector. The total photosensitive area of PMTs covers 25 % of the entire inner surfaces of the detector.

The principle of particle detection is as follows. A charged particle propagating in water emits Cherenkov photons, when its velocity (v) exceeds the light velocity in water (c/n);

$$n\beta > 1, \qquad \beta \equiv \frac{v}{c} \tag{2.1}$$

where n (=1.344) is the refraction index of water. The light emission process is analogous to the shock wave production. Cherenkov photons are emitted in a circular cone with a half opening angle of θ to the particle trajectory,

$$\cos\theta = \frac{1}{n\beta} \tag{2.2}$$

In the case of the relativistic limit (β=1), θ has an asymptotic value of 41.9°. The spectrum of Cherenkov lights is quantum-mechanically calculated by Tam and Frank [34] and the number of photons emitted per unit path length per unit wave length $dN/dxd\lambda$ is,

$$\frac{dN}{dxd\lambda} = 2\pi\frac{\alpha}{\lambda^2}\left(1 - \frac{1}{n^2\beta^2}\right) \tag{2.3}$$

where α is the fine structure constant, x the path length of the charged particle and λ the wave length of Cherenkov lights. The threshold momentum of Cherenkov light emission depends on its mass due to the condition of Eq. 2.1.

In the case of atmospheric neutrinos, a typical reaction (quasi-elastic scattering) is as follows,

$$\nu + N \rightarrow l + N'$$

where ν is the incident neutrino, N and N' are nucleons, l is a lepton associated with the flavor of the incident neutrino (e or μ).

This reaction is depicted in Fig. 2.2. An incident neutrino (denoted by the dotted arrow) enters the detector and produces a lepton (an electron or a muon : corresponding to the solid arrow) by the quasi-elastic neutrino interaction. The Cherenkov light photons emitted by the secondary lepton are caught by PMTs. The lepton trajectory is reconstructed by timing information and the shape of the doughnut ring-image. The lepton energy is determined by charge information, i.e., total number of photoelectrons.

2.2 Operation of Kamiokade detector

Kamioka Nucleon Decay Experiment (acronymed as "Kamiokande") started data-taking in July 1983 and continued the operation until November 1985, for the purpose of detecting possible nucleon decay and atmospheric neutrinos. The experiment during this period was called Kamiokande-I [35], [36]. At the end of Kamiokande-I, an anticounter was constructed in order to eliminate cosmic-ray muons and γ-rays from surrounding rock.

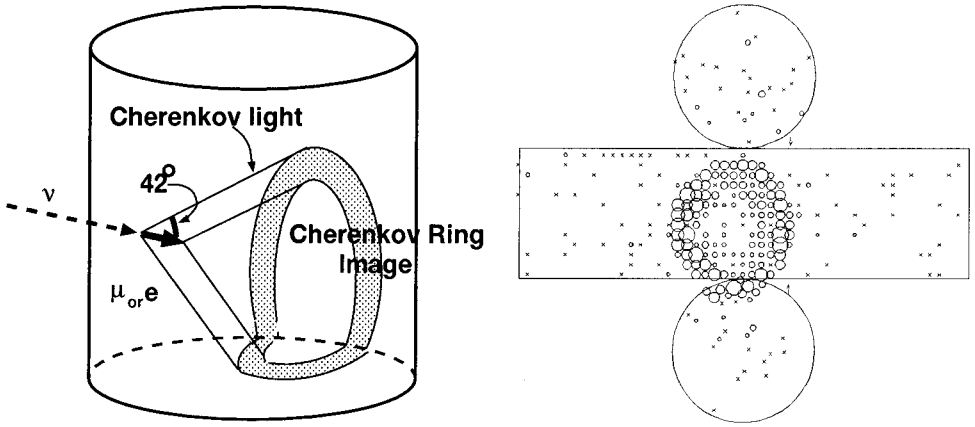

Figure 2.2: Schematic of the detection principle and the exploded view of the detector

In November 1985, Kamiokande-II [37] started. Kamiokande-II aimed at detecting not only nucleon decays and atmospheric neutrinos, but also low-energy neutrinos (~10MeV) such as ^{8}B solar neutrinos [38], neutrino bursts from supernovae [39], [40] and supernova-induced relic neutrinos [41]. In fact, a neutrino burst from supernova (SN1987a) was firstly detected by Kamiokande-II [39], which also succeeded in observing solar ^{8}B neutrinos [42], [43]. Kamiokande-II ended in April 1990 to replace dead PMTs and to install new electronics.

Afterward, Kamiokande-III started in December 1990 and is still running. The total data taking time integrated over Kamiokande-III is 1.22×10^8 seconds (or 1418 days) and the total detector live time is 1.15×10^8 seconds (or 1332 days).

2.3 Anticounter

The anticounter, which is also a water Cherenkov detector, was constructed aiming at two major purposes.

(a) Vetoing entering cosmic-ray mouns

Entering cosmic-ray muons are easily identified by requiring a suitable amount of signals in the anticounter.

(b) Shielding neutral particles

Neutral particles of external origin, such as γ-rays and neutrons, also sneak into the detector, but they are effectively reduced by the water in the anticounter.

Figure 2.1 shows schematic view of the anticounter. The top and bottom parts of the anticounter were constructed inside the main inner tank, but the barrel part of the anticounter was made in the cavity space between the main tank and the cavity wall. The cavity wall was coated with rubber-asphalt to make it waterproof.

Typical thickness of the water in the anticounter section is 1.2 m, 0.8 m and 2 m for the bottom, top and barrel part, respectively. The PMTs are mounted with density of 1 PMT/9 m^2. The inner surfaces of the anticounter are completely covered with aluminum reflective sheets to compensate for the relatively poor light collection efficiency, owing to the lower PMT density. However, these reflective sheets make timing information of the anticounter useless.

2.4 50 cm-in-diameter PMT

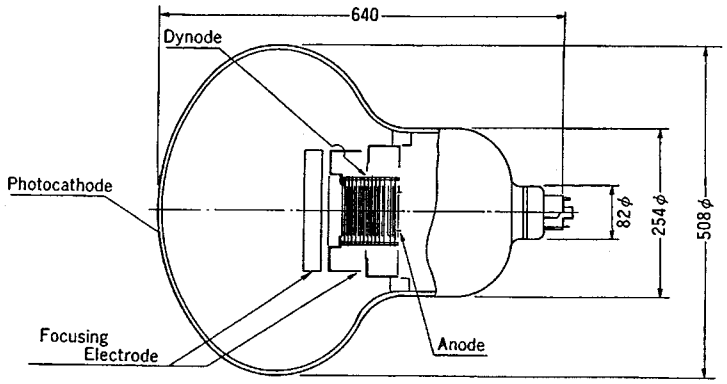

Figure 2.3: Structure of the 50 cmϕ PMT

The 50 cm-in-diameter PMTs were specially developed for this experiment by Hamamatsu Photonics Co. in cooperation with members of the collaboration.

The structure of the 50 cmϕ PMT is shown in Fig. 2.3, while its specifications are summarized in Table 2.1.

Photo-cathode area	50 cm in diameter
Shape	Hemispherical
Window material	Pyrex glass (4$\sim$5mm)
Phot-cathode material	Bialkali
Dynodes	13 stages, Venetian blind
Quantum efficiency	22% typical at λ=420nm
Gain	10^7 at $\sim$2000Volt
Dark current	150nA at gain=10^7
Dark pulse rate	15kHz at gain=10^7
Cathode non-uniformity	less than 20%
Anode non-uniformity	less that 40%
Transit time	90nsec typical at gain=10^7
Transit time spread	σ=4.7nsec at 1p.e. pulse

Table 2.1: Specifications of the Hamamatsu 50 cmϕ PMT.

The spectral dependence of its quantum efficiency is shown in Fig. 2.4, which exhibits the characteristics typical of the bi-alkali photocathode. The relative Cherenkov light spectrum passing through 15 m of pure water is also shown in Fig. 2.4. These two curves have a similar shape, thus assuring efficient detection of Cherenkov light photons.

Between Kamiokande-II and Kamiokande-III periods, 120 PMTs of 50 cm in diameter, which were being improved, i.e., semi-final version for the forthcoming Super-Kamiokande experiment, were replaced dead PMTs of Kamiokande-II. The number of the dynode stages of the new PMT is optimized to 11 stages, and mainly due to this improvement, the timing resolution becomes less than 3 nsec (1σ) at single

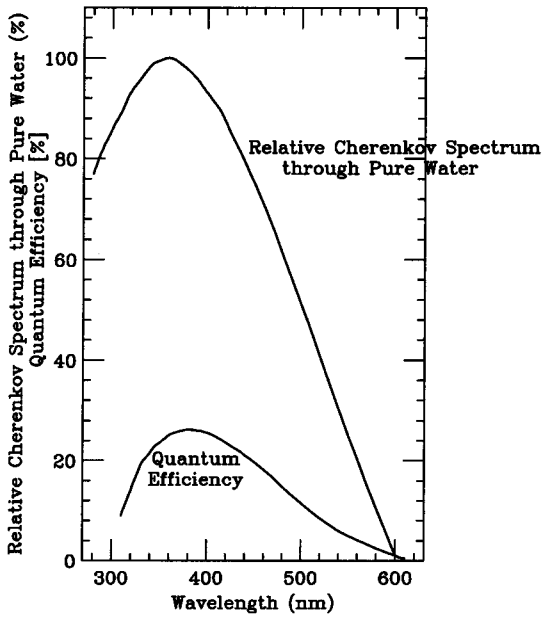

Figure 2.4: Spectral dependence of the quantum efficiency of 50 cmϕ PMT. Also shown is the relative Cherenkov spectrum through 15 m thick pure water.

photoelectron pulse height (in Kamiokande-II, the timing resolution of PMTs was ~5 nsec).

Because of the long distance between the photocathode and the first dynode, the 50 cmϕ PMT is sensitive to magnetic fields. Even the geomagnetic field (0.45 gauss) causes a problem in the total energy measurement and in the event reconstruction. In order to compensate for the geomagnetic field, the following two independent magnetic shields were employed.

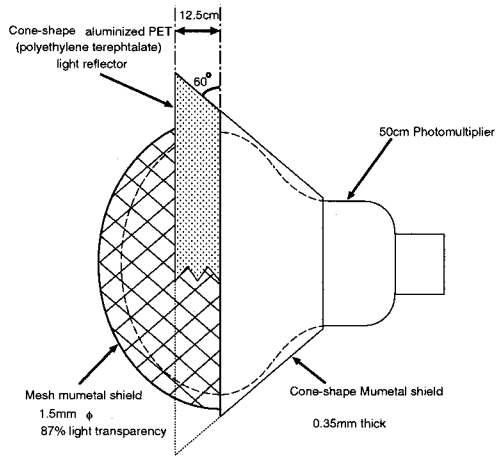

Figure 2.5: 50 cmϕ PMT with a magnetic shield and a reflector

(a) Each PMT is covered with the special magnetic shield as shown in Fig. 2.4. It consists of two parts. The front is a hemispherical mesh made of μ-metal which transmits 87 % of the total incident light, while the back is a cone-shaped μ-metal. This gives a shielding factor of 3 to 8 depending on the relative orientation of the PMT with respect to the geomagnetic field.

(b) A system of current networks were constructed around the cavity walls surrounding the detector, shown in Fig. 2.6, for the global cancellation of the geomagnetic field. The typical strength of the geomagnetic field near the PMT was measured to be 0.1 gauss.

By means of these two compensations, the residual magnetic field inside a PMT is reduced to less than 0.03 gauss.

Furthermore, in order to collect Cherenkov photons more efficiently, a light reflector was attached to each inner PMT as shown in Fig. 2.4. They are made from aluminized PET (polyethylene terephtalate) sheet, of which reflection efficiency is about 80 %. As a result, the effective photo-coverage area increased from 20 % to 25 %.

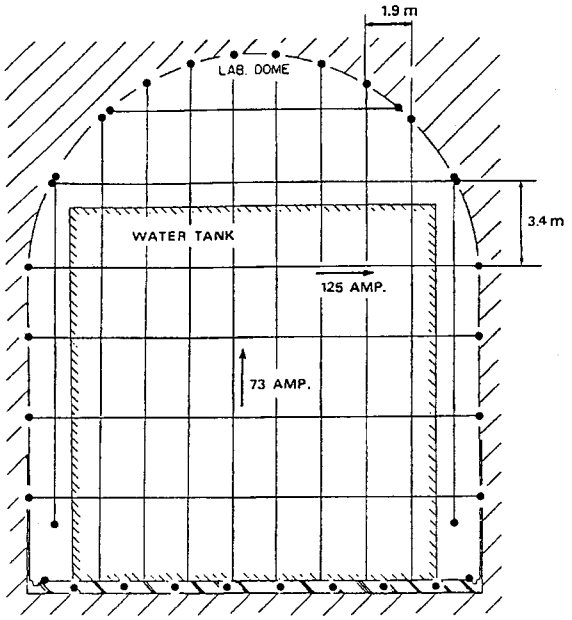

Figure 2.6: A current network around the cavity walls to compensate for the geomagnetic field in the detector.

2.5 Water purification system

For a large water Cherenkov detector, the water must be kept as transparent as possible in order to collect many Cherenkov photons. Therefore, the water purification system is installed.

As is schematically shown in Fig. 2.7, the water purification system for the inner tank is composed of the following 6 elements,

- A 5-10 μm filter (F2)
- A deionization system
- A Uranium removal system
- A 1.2 μm filter (F3)
- An ultra-violet sterilizer
- A 0.6 μm filter (F4, F5)

The water in the inner tank circulates at a flow rate of 4.5 tons/hour. The water attenuation length measured by cosmic-ray muons is 55 m (see Appendix A).

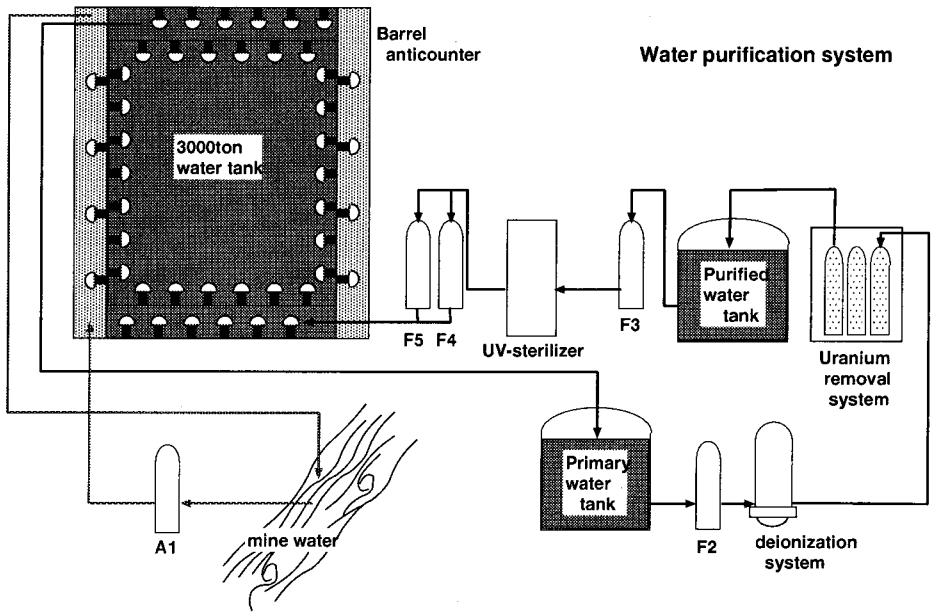

Figure 2.7: Schematic description of the water purification system in the Kamiokande III. A1 (5 μm filter) is used for the anticounter and F2 (5-10 μm filter), F3 (1.2 μm filter), F4 and F5 (0.6 μm filter) for the inner detector.

On the other hand, the fresh mine water is constantly fed to the barrel anticounter from the bottom through a 5 μm filter (A1) at a rate of $\sim$10 tons/hour, due to the water leakage through the cavity wall insufficiently coated with rubber asphalt. The overflow water goes back to the underground water stream.

2.6 Trigger system

In Kamiokande-III, all events of which energy is above 5.0 MeV are triggered. The signal from each PMT is divided into three (see Fig. 2.8). One of them is sent to a discriminator which judges whether the PMT is hit or not and a rectangle pulse (100 nsec width, -2.5 mV height) is generated. The threshold level of the discriminator is set to -36.6 mV, which roughly corresponds to 0.2 photoelectrons. All discriminator outputs are summed up and the pulse height of the summed signal corresponds to the number of hit PMTs. An event trigger is created when it exceeds 20 hit PMTs (master threshold -50 mV), which corresponds to 5.0 MeV for an electron. The second of divided signals is fed to ADC[1] to measure the energy deposited inside the detector. The remaining signal is delayed 200 nsec and sent to a TDC[2] by a discriminator as a stop pulse to measure relative timing information.

The trigger rate is roughly 1 Hz. A large part of triggered events are low-energy events, for instance, β-rays from radioactivities in the detector water and the external γ-rays from the surrounding rock. These events are the main background against the analysis of ^{8}B solar neutrinos and relic neutrinos from supernovae. The remaining events are downward-going cosmic-ray muons ($\sim$0.37 Hz). The triggering efficiency for a muon having energies more than 200 MeV (corresponding to an electron with energy

[1]ADC is an analog-to-digital converter which converts an analog information to a digital number.

[2]TDC is a time-to-digital converter which converts a time information to a digital number.

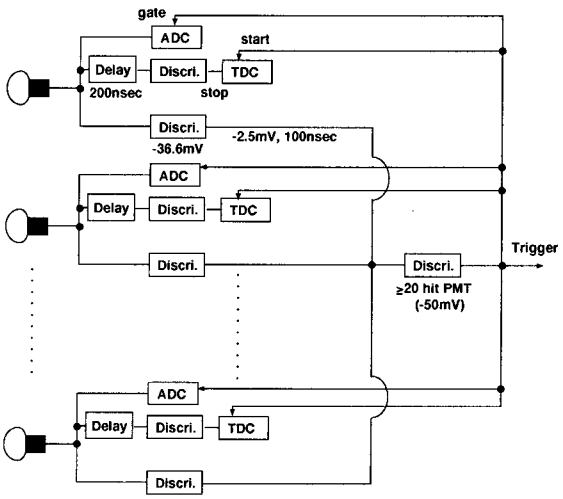

Figure 2.8: Schematic for trigger system and electronics in Kamiokande-III

$E \simeq 30$ MeV) is estimated to be ~100 %. The measured trigger efficiency for an electron in Kamiokande-III is shown in Fig. 2.9.

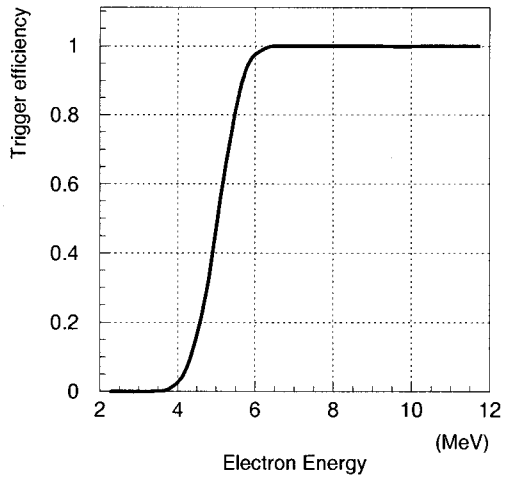

Figure 2.9: Trigger efficiency of the Kamiokande-III detector. The solid curve represents the efficiency for an electron.

2.7 Typical Event

A typical downward through-going muon observed in the Kamiokande-III detector is shown in Fig. 2.10, which depicts an exploded view of the cylindrical Kamiokande-III detector. The area of each little circle is proportional to the recorded number of photoelectrons by each PMT, which is normalized by the total number of photoelectrons observed in the inner detector. The cylindrical anticounter is also depicted at the upper left corner in Fig. 2.10.

Among muons, some enter the detector and stop inside the detector. Such muons are categorized as stopping muons. With some of them, a decay electron is also accompanied. Figure 2.11 shows a typical

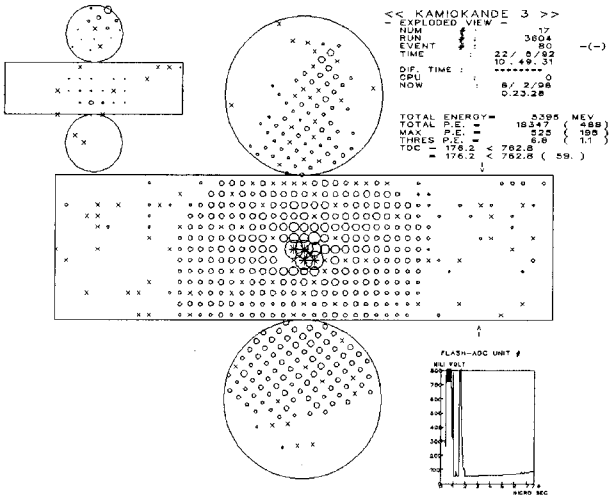

Figure 2.10: A typical downward through-going cosmic-ray muon event. A muon enters on the top part of the detector and exits to the barrel part. The top part and the barrel part of the anticounter are also hit by the Cherenkov photons emitted by the muon.

stopping muon event (a) and an accompanied μ-decay electron (b).

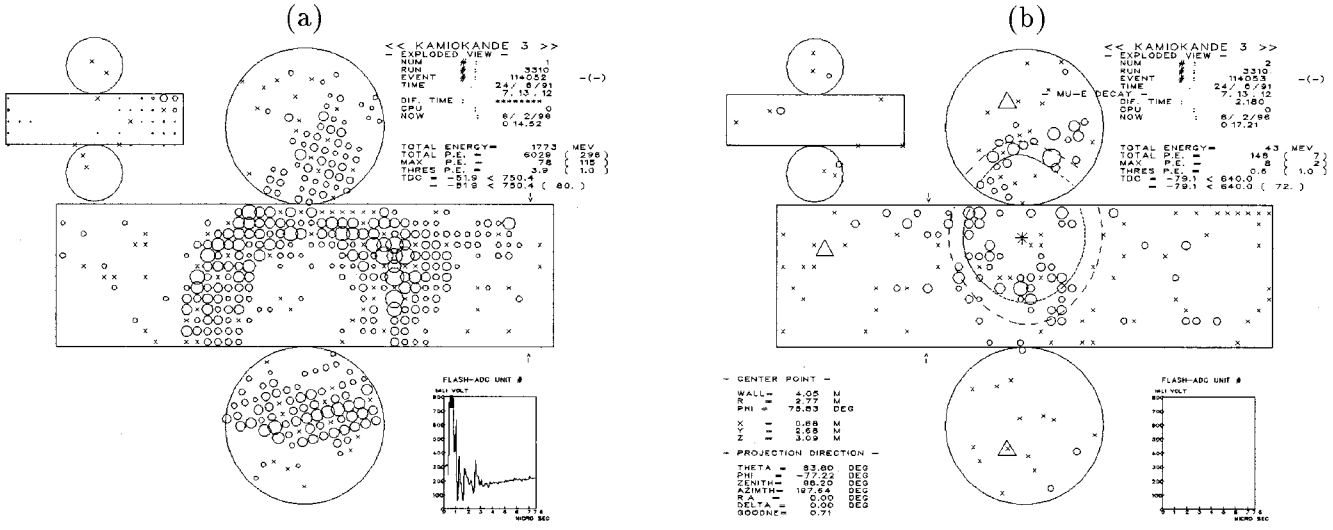

Figure 2.11: Typical events of stopping muon (a) and successive μ-decay electron (b).

As described previously, neutrino-induced contained events are also detected at a rate of $\sim$1 event/4 days. Figure 2.12 shows typical contained events. These contained events are classified as electron or muon events by the diffuseness of thier Cherenkov ring pattern. For instance, Fig. 2.12(a) is identified as an electron event caused by the $\nu_e N \rightarrow eN'$ reaction and Fig. 2.12(b) as a muon event produced by the $\nu_\mu N \rightarrow \mu N'$ reaction.

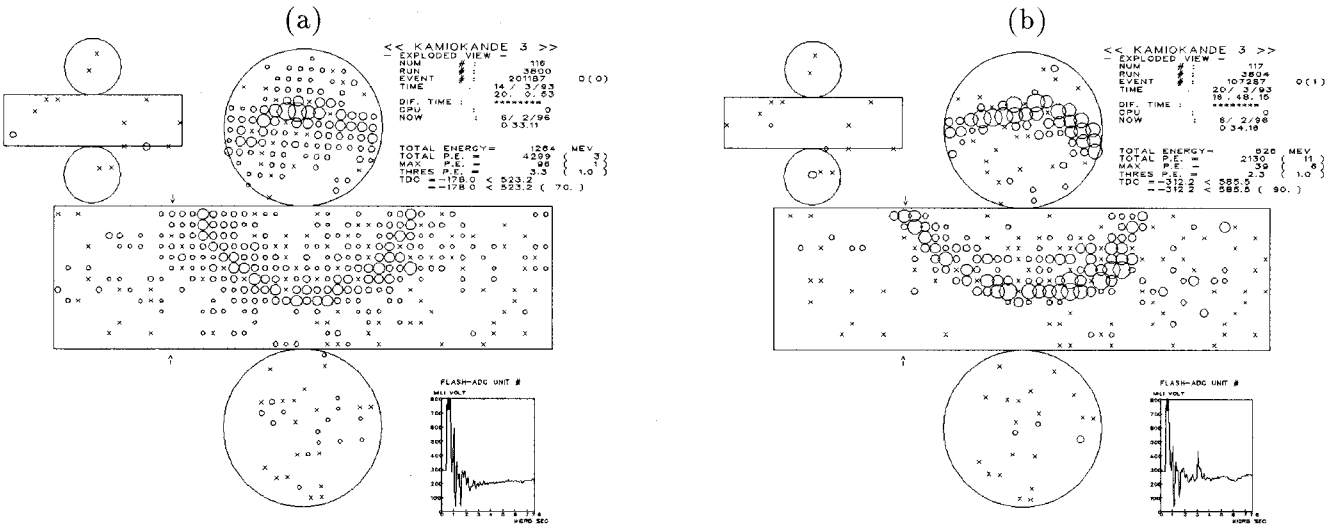

Figure 2.12: A ν_e-induced contained event (a) and a ν_μ-induced contained event (b).

Chapter 3

Expected upward through-going muon flux

To compare the observed upward through-going muon flux against the expectation with or without the neutrino oscillation, one has to establish a method to calculate the expected fluxes. In this chapter, the method to calculate the expected flux will be described in detail.

3.1 Calculation of upward through-going muon flux

Upward-going muons are produced by the interaction of atmospheric neutrinos with the matter surrounding the detector. Muons produced far away do not reach the detector. Those muons that do reach the detector have traveled in the rock losing their energy.

The procedure described was initialy developed by M.Honda and M.Mori when they calculated the upward-going muon flux from SN1987A. Some parts were modified in order to adapt to the atmospheric neutrino case.

The production cross section of the muons which are generated by parent neutrinos of energy E_ν is given by

$$\frac{d^2\sigma}{dxdy} \cdot \frac{d^2\phi_\nu(E_\nu, \cos\Theta_\nu)}{dE_\nu d\Omega} \tag{3.1}$$

where $d^2\sigma/dxdy$ is the differential charged current cross section as a function of the Bjorken scaling parameters, x and y (to be defined in Section 3.3). The zenith angle Θ_ν is the neutrino incident angle relative to the detector (upward direction is given by $\cos\Theta_\nu = -1.$). $d^2\phi_\nu(E_\nu, \cos\Theta_\nu)/dE_\nu d\Omega$ is the differential spectrum of the parent neutrinos as a function of the neutrino energy and the zenith angle.

If we define $g(X, E_\mu, E'_\mu)$ as the probability that a muon generated with energy E_μ survives with energy larger than E'_μ after traveling the thickness of $X(\mathrm{g/cm^2})$, then the muon flux at the detector with energy larger than E'_μ is given by

$$\frac{d\phi_\mu(E'_\mu, \cos\Theta_\mu)}{d\Omega} = \int_0^\infty N_A dX \int_{E_\mu}^\infty dE_\nu \int_0^1 dy \int_0^1 dx \cdot \frac{d^2\sigma}{dxdy} \cdot \frac{d^2\phi_\nu(E_\nu, \cos\Theta_\nu)}{dE_\nu d\Omega} \cdot g(X, E_\mu, E'_\mu) \tag{3.2}$$

Here, Θ_μ is the zenith angle of the induced muon and N_A is Avogadro's number. Although, Θ_μ is a convolution of Θ_ν and the production angle $\Delta\theta_{\nu\mu}$, it is assumed that $\Theta_\mu = \Theta_\nu$. This angular uncertainty

is included in the systematic errors of the experiment and will be discussed in Section 5.3. In the following calculation, both Θ_μ and Θ_ν are denoted as Θ.
The function $g(X, E_\mu, E'_\mu)$ can be written as

$$g(X, E_\mu, E'_\mu) = \vartheta(R(E_\mu, E'_\mu) - X) \tag{3.3}$$

where $R(E_\mu, E'_\mu)$ is a range that the muon travels while its energy decreases from E_μ to E'_μ, and ϑ is the step function;

$$\vartheta(x) = \begin{cases} 1 & \text{if } x \geq 0 \\ 0 & \text{if } x < 0 \end{cases} \tag{3.4}$$

The integral over X, $\int_0^\infty \vartheta(R(E_\mu, E'_\mu) - X)dX$ can be simply replaced by $R(E_\mu, E'_\mu)$, and $d\phi_\mu(E'_\mu, \cos\Theta)/d\Omega$ is reduced to be

$$\frac{d\phi_\mu(E'_\mu, \cos\Theta)}{d\Omega} = \int_{E_\mu}^\infty dE_\nu \int_0^1 dy \int_0^1 dx \cdot \frac{d^2\sigma}{dxdy} \cdot \frac{d^2\phi_\nu(E_\nu, \cos\Theta)}{dE_\nu d\Omega} \cdot R(E_\mu, E'_\mu) \cdot N_A \tag{3.5}$$

Since the neutrino flux and the muon range do not depend on the scaling parameter x, and the integral over y is independent of the neutrino energy spectrum, Eq. 3.5 can be transformed as follows,

$$\begin{aligned} \frac{d\phi_\mu(E'_\mu, \cos\Theta)}{d\Omega} &= \int_{E_\mu}^\infty \left[\int_0^1 \left[\int_0^1 \frac{d^2\sigma}{dxdy}dx\right] \cdot N_A \cdot R(E_\mu, E'_\mu)dy\right] \frac{d^2\phi_\nu(E_\nu, \cos\Theta)}{dE_\nu d\Omega}dE_\nu \\ &= \int_{E_\mu}^\infty \left[\mathcal{P}(E_\nu, E'_\mu) \cdot \frac{d^2\phi_\nu(E_\nu, \cos\Theta)}{dE_\nu d\Omega}\right] dE_\nu \end{aligned} \tag{3.6}$$

Where the function $\mathcal{P}(E_\nu, E'_\mu)$ is defined as,

$$\mathcal{P}(E_\nu, E'_\mu) = N_A \int_0^1 \left[\left[\int_0^1 \frac{d^2\sigma}{dxdy}dx\right] \cdot R(E_\mu, E'_\mu)\right] dy \tag{3.7}$$

It is interpreted as the probability that the neutrinos of energy E_ν are observed as muons at the detector with energy larger than E'_μ, hence this function is named as the "observation probability".

This equation is very useful if one wants to calculate the upward through-going muon flux for variety of assumptions on the neutrino energy spectrum. Since the neutrino cross sections and the muon range are already included in the function $\mathcal{P}(E_\nu, E'_\mu)$, the muon flux with energy larger than E'_μ can be obtained by a single integral, once the neutrino flux is given for a case in study. The effect of neutrino oscillation can easily be incorporated into the formula, since it only modulates the neutrino flux (as a function of Δm^2 and θ_v).

As ν_μ has a different reaction cross section from $\overline{\nu}_\mu$, Eq. 3.6 should be replaced in the real application with:

$$\frac{d\phi_\mu(E'_\mu, \cos\Theta)}{d\Omega} = \int_{E_\mu}^\infty \left[\mathcal{P}_{\nu_\mu}(E_\nu, E'_\mu)\frac{d^2\phi_{\nu_\mu}(E_\nu, \cos\Theta)}{dE_\nu d\Omega} + \mathcal{P}_{\overline{\nu}_\mu}(E_\nu, E'_\mu)\frac{d^2\phi_{\overline{\nu}_\mu}(E_\nu, \cos\Theta)}{dE_\nu d\Omega}\right] dE_\nu \tag{3.8}$$

The distinction between μ^+ and μ^- is not necessary, because the Kamiokande-III detector can not discriminate μ^+ from μ^-.

3.2 Atmospheric neutrino flux

The energy spectrum of atmospheric neutrinos can be calculated starting from differential energy spectrum of primary cosmic rays and be qualitatively expressed as:

$$\frac{dF_\nu}{dE} \propto E^{-2.7} \tag{3.9}$$

Actual energy spectrum has a little steeper slope, mostly due to larger absorption cross sections of pions and kaons at higher energies.

For a quantitative calculation of the flux of atmospheric neutrinos, a detailed understanding of interaction of incoming primary cosmic rays with atmospheric nuclei is required. Furthermore the differential energy spectrum and chemical composition (H, He, CNO nuclei and so on) of the primary cosmic rays are needed. Various experiments are carried out to investigate the characteristics of promary cosmic-ray, but in present the uncertainty of the experimental primary cosmic-ray energy spectrum is ~15 %. Many physicists calculate the flux of the atmospheric neutrinos by using the various experimental data. The main uncertainty is caused by that of the primary cosmic-ray flux. However, the atmospheric neutrino at E_ν ~300 GeV by using the observed muon flux, of which spectrum is wellknown. Therefore, the uncertaint of the neutrino flux at higher energy can be reduced more effectively than that of low energy region.

The atmospheric neutrino flux has been caclulated by a number of physicists recently. Butkevitch et al [44] and Lipari [1] calculated it ranging from around 1 GeV to above 100,000 GeV. The calculations by Gaisser et al [45] and Honda et al [2] are available from low energies (less than 1 GeV) to about 3,000 GeV. The results except for Honda's flux are calculated by analytical method, while Honda's flux is estimated by Monte Carlo method. Their results are avialable as a form of tables of ν_μ, $\overline{\nu}_\mu$, ν_e, $\overline{\nu}_e$ fluxes as a function of neutrino energy and zenith angle. Figure 3.1 shows a sample of $(\nu_\mu + \overline{\nu}_\mu)$ flux.

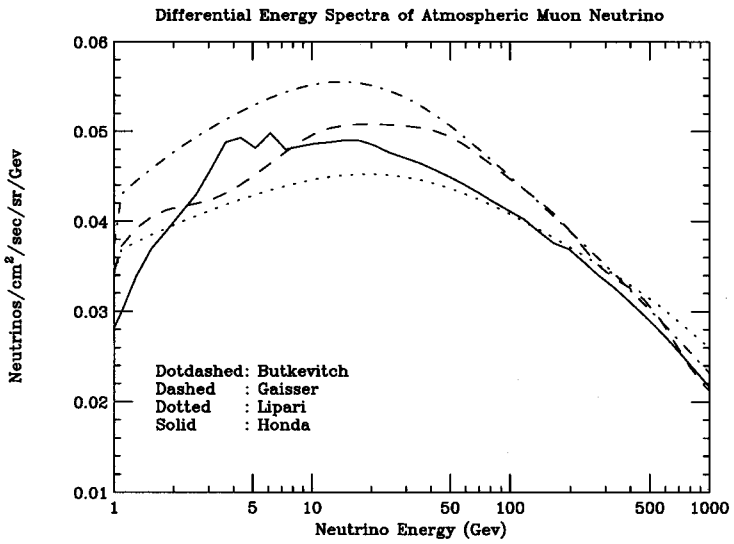

Figure 3.1: The atmospheric neutrino flux given by different authors. The ordinate is the differential flux multiplied by E^3 in order to clarify the differences.

Figure 3.2 shows angular distributions on the atmospheric muon neutrinos $(\nu_\mu + \overline{\nu}_\mu)$ at energies 1 GeV, 10 GeV and 100 GeV, respectively. The angular distributions vary between nadir and the horizon, due

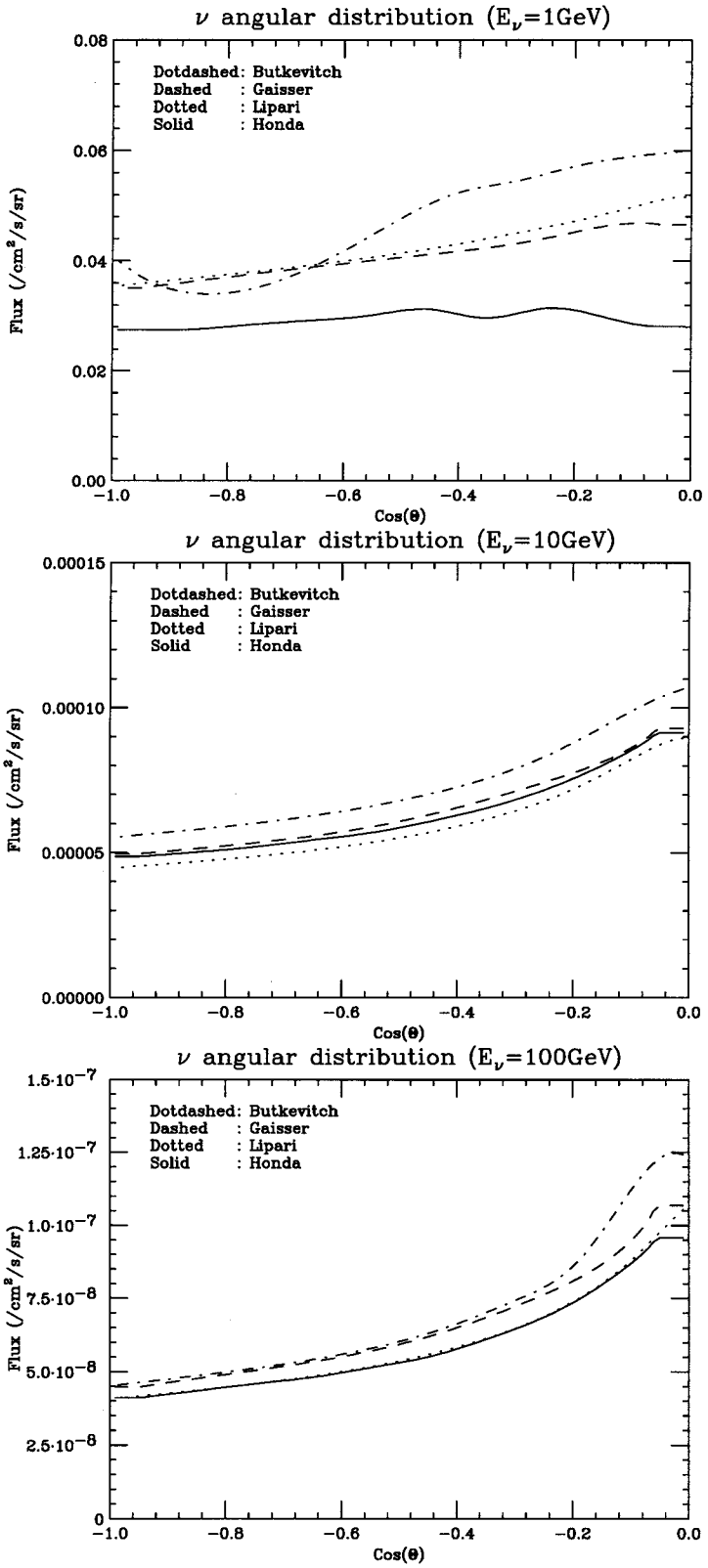

Figure 3.2: Angular distributions of the atmospheric muon neutrinos (ν_μ+ $\overline{\nu}_\mu$) at energies E_ν=1 GeV, 10 GeV and 100 GeV,respectively.

to the increase in decay length in the horizontal geometry.

3.3 Charged current cross section

To calculate the expected upward through-going muon flux, the cross section of the charged current neutrino interaction with rock is needed. The relevant physical process is:

$$\nu_\mu(\overline{\nu}_\mu) + N \rightarrow \mu^-(\mu^+) + anything$$

where N represents a nucleon in the rock. The differential charged current cross section for this process is expressed in terms of the Bjorken scaling parameter, $x = Q^2/2M\mathcal{V}$[‡] and $y = 1 - (E_\mu/E_\nu)$,

$$\frac{d^2\sigma}{dxdy} = \frac{G^2 M E_\nu}{\pi} \frac{M_W^4}{(M_W^2 + Q^2)^2} \left[y^2 x F_1 + \left(1 - y - \frac{Mxy}{2E_\nu}\right) F_2 \pm \left(y - \frac{y^2}{2}\right) x F_3 \right] \tag{3.10}$$

where the last term is positive for ν and negative for $\overline{\nu}$, Q^2 is the absolute value of invariant momentum transfer squared between the incident neutrino and outgoing muon, $\mathcal{V} = \mathrm{E}_\nu - \mathrm{E}_\mu$ is the energy loss in the laboratory frame, M and M_W are the nucleon and the intermediate $W^\pm$ boson masses, G is the Fermi constant, and $F_1(x, Q^2)$, $F_2(x, Q^2)$ and $F_3(x, Q^2)$ are the structure functions given by quark momentum (normalized to one) distribution functions.

For $\nu_\mu p(n) \rightarrow \mu^- X$,

$$F_2 = 2xF_1 = 2x\left[f_d(f_u) + f_s + f_b + f_{\overline{u}}(f_{\overline{d}}) + f_{\overline{c}} + f_{\overline{t}}\right] \tag{3.11}$$

$$F_3 = 2\left[f_d(f_d) + f_s + f_b - f_{\overline{u}}(f_{\overline{d}}) - f_{\overline{c}} - f_{\overline{t}}\right] \tag{3.12}$$

And for $\overline{\nu}_\mu p(n) \rightarrow \mu^+ X$

$$F_2 = 2xF_1 = 2x\left[f_u(f_d) + f_c + f_t + f_{\overline{d}}(f_{\overline{u}}) + f_{\overline{s}} + f_{\overline{b}}\right] \tag{3.13}$$

$$F_3 = 2\left[f_u(f_d) + f_c + f_t - f_{\overline{d}}(f_{\overline{u}}) - f_{\overline{s}} - f_{\overline{b}}\right] \tag{3.14}$$

The quark distributions employed in this analysis are calculated by Eichten et al (EHLQ) [46], Owens [47], CTEQ collaboration [48] and Martin et al (MRS) [49]. These quark distribution models are parametarized by using the various experimental data. Therefore, models depend on the experimental results used in their calculation and fitting methods.

Figure 3.3 shows the charged current cross sections calculated by the various quark distribution models with the experimental data.

3.4 Muon range in the rock

The knowledge of muon energy loss is also required to calculate the expected upward through-going muon flux, since the muon energy loss determines the produced muon range.

[‡]Not to be confused with ν.

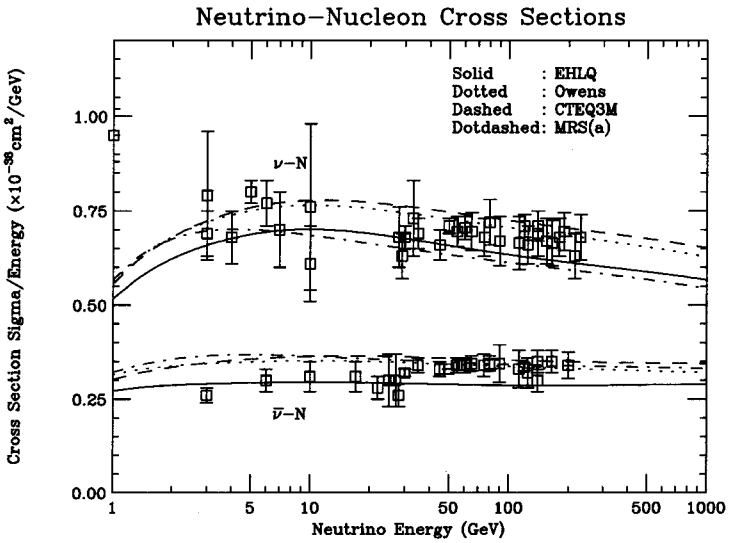

Figure 3.3: The charged current neutrino-nucleon cross sections. Data points are compiled by Particle Data Group [50].

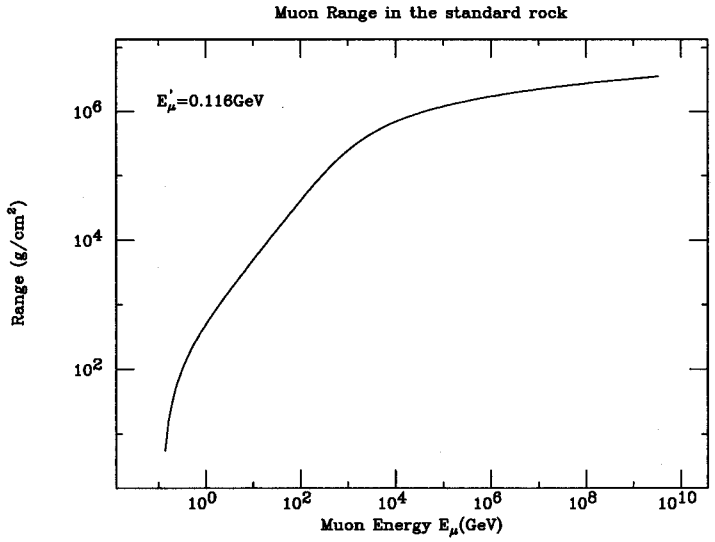

Figure 3.4: The range of the muon in the standard rock.

The numerical result calculated by Lohmann et al [51] in the energy range 1 $\sim$ 10000 GeV are employed in this analysis. In the calculation, the energy loss by ionization, bremsstrahlung, direct pair production and photonuclear interactions are carefully taken into considerations. The muon energy loss is estimated for several kinds of materials. Among them, the energy loss in the standard rock[1] is chosen.

The muon range, R, is a function of initial energy, E_i, and final energy, E_f, and is defined as a distance that the muon travels while the muon loses its energy from E_i to E_f. For the through-going muons, the initial energy, E_i is set to the muon energy at production (E_μ) and E_f is set to E'_μ which is the minimum energy deposited in the detector. A result (in this case, E'_μ is set to a constant, 0.116 GeV, and E_μ is changed) is shown in Fig. 3.4:

$$R(E_\mu, E'_\mu) = \int_{E_\mu}^{E'_\mu} \frac{-dE}{dE/dX} \tag{3.15}$$

3.5 Calculated upward through-going muon flux

As was mentioned in section 3.2, four flux models calculated by Butkevitch, Gaisser, Lipari and Honda, are employed in this analysis. For the neutrino-nucleon interaction cross sections, another four distributions i.e., EHLQ, Owens, CTEQ and MRS models are adopted. Therefore, 16 different flux models are obtained.

To compare the theoretical models with the data, smearing due to finite resolution of the measurements has to be taken into account. Detailed discussion of the smearing will be given in section 5.3. The final value of the expected flux includes these effects and the result is shown in Fig. 3.5 as a function of zenith angle Θ.

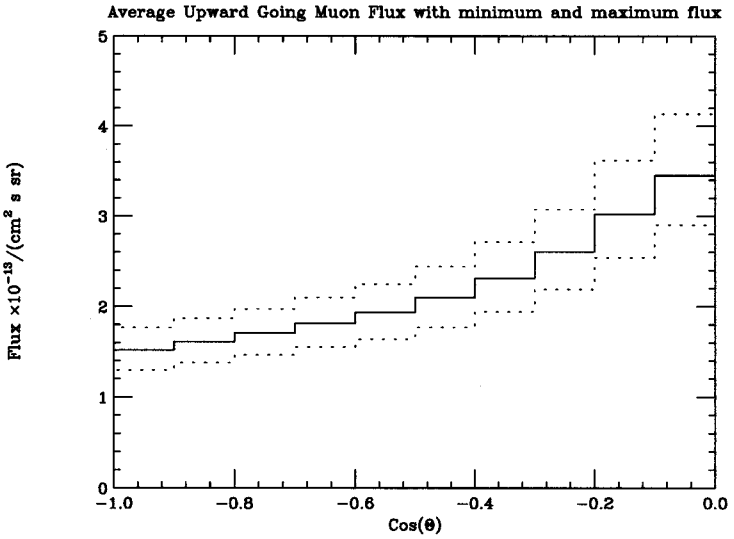

Figure 3.5: The average of the expected upward through-going muon flux (solid). The minimum and the maximum values of various models are drawn together (dotted).

Table 3.1 summarizes the expected total muon fluxes integrated over the zenith angle acceptance ($-1 \leq \cos\Theta \leq -0.04$) employed in this analysis.

[1]The density of the standard rock is $\sim$2.7 g/cm^3.

Taking the average of all the models, we obtaine as the total expected flux is $(2.20^{+0.39}_{-0.34}) \times 10^{-13}\mathrm{cm}^{-2}\,\mathrm{s}^{-1}\mathrm{sr}^{-1}$, where the errors indicate the difference between the maximum (minimum) and the average. Consequently the systematic error of theoretical origin in the absolute value of the expected upward through-going muons is estimated to be ± 18 %.

	EHLQ	Owens	CTEQ	MRS
Butkevitch	2.19	2.44	2.58	2.27
Gaisser	2.08	2.32	2.45	2.15
Lipari	1.98	2.21	2.33	2.04
Honda	1.86	2.07	2.20	1.94

Table 3.1: Upward through-going muon flux for the Kamiokande detector. The unit is $\times 10^{-13}\mathrm{cm}^{-2}\mathrm{s}^{-1}\mathrm{sr}^{-1}$

Hereafter, Honda's flux, CTEQ cross sections and Lohmann's calculation for the muon energy loss will be used. The reasons are that the calculated flux is very similar to the average value and Honda's flux takes recent experimental results into considerations and coveres a wide energy range from 30 MeV up to 3,000 GeV.

Chapter 4

Event selection

The Kamiokande-III detector started data-taking in December 1990, and is still in operation now. The data sets used in this analysis are taken from December 1990 to May 1995 corresponding to 1332-day detector livetime. A total of 1.43×10^8 events were recorded during this data-taking period. Figure 4.1 shows the algorithm of event selection and these selection processes will be introduced successively.

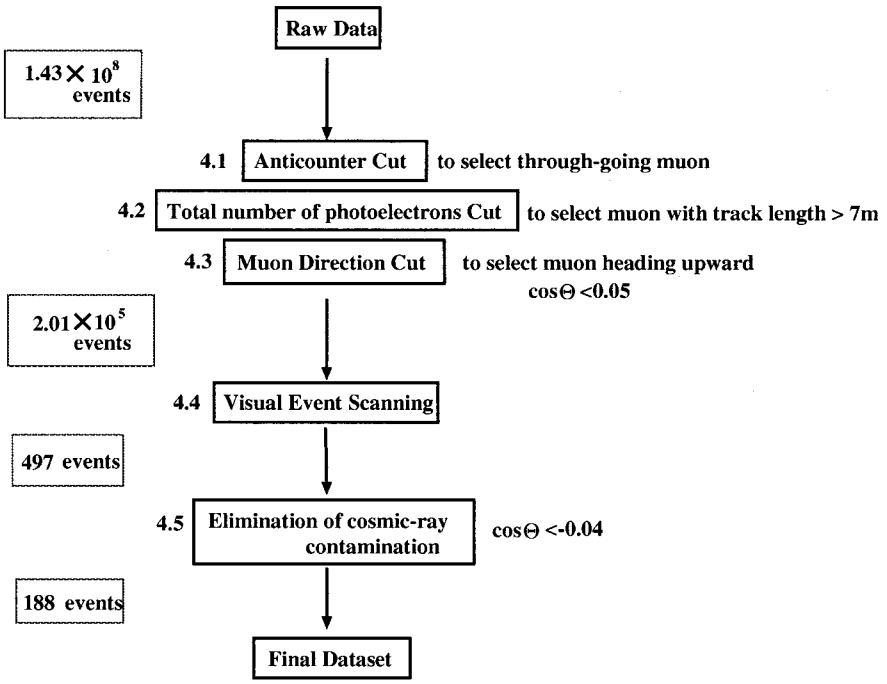

Figure 4.1: Algorithm of event selection. The numbers left of the square corresponds to section number

4.1 Anticounter cut

This cut selects through-going muons from raw data.

The Kamiokande-III detector has a 4π solid-angle water Cherenkov anticounter, which is divided into three parts, i.e., top, bottom and barrel parts. The anticounter tags incoming and outgoing muons.

Typical through-going muons hit two parts of the anticounter, one at the entrance and the other at the exit (Fig. 4.2). On the other hand, stopping muons hit only one part of the anticounter as shown in

Fig. 4.3.

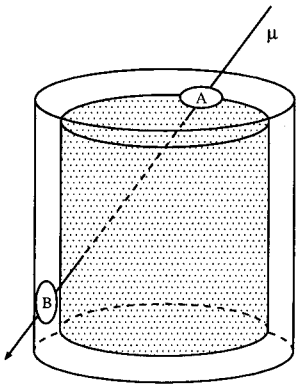

Figure 4.2: The hit pattern in the anticounter for through-going muons. In this case, the entering muon hits "A" on the top part of the anticounter, and hits "B" on the barrel part of the anticounter when it exits the detector.

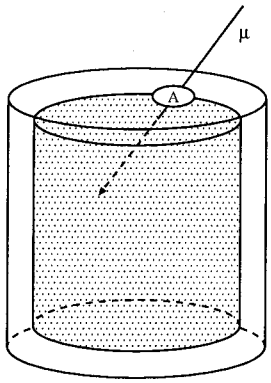

Figure 4.3: The hit pattern in the anticounter for stopping muons. In this case, the entering muon hits only "A" on the top part of the anticounter because the entering muon stops inside the detector.

When the following three requirements are satisfied, it is considered that a muon hits one part of the anticounter. These cuts mainly reduce random trigger generated by either PMT noise or by isotopes in the material.

- Total number of photoelectrons in a part of the anticounter $\geq$ 20 p.e. (see Fig. 4.4)
- Number of hit PMT in the same part of the anticounter $\geq$ 5
- Maximum number of photoelectrons/PMT in an event in the same part of the anticounter $\geq$ 5 p.e.

An event with two hits at two different parts of the anticounter is saved as a through-going muon.

4.2 Toatal number of photoelectron cut

Figure 4.5 shows a correlation between the total number of photoelectrons and the corresponding muon track length in the detector. This plot is made by sampling downward through-going muon data sets. For muons with short track length, the spatial reconstruction becomes ambiguous to identify as muons. The track length of minimum 7 m was chosen as the requirement. A selection criterion that the total number of photoelectrons of the event should be larger than 6000 p.e. is imposed to ensure minimum muon track length of 7 m.

Moreover, an upper limit is also set at 40000 p.e.. As is seen Fig. 4.6, almost all (99.8 %) through-going muon events produce a total number of photoelectrons under this upper limit. Multiple muons or muons accompanied with bremsstralung and/or hadronic showers are removed by this cut.

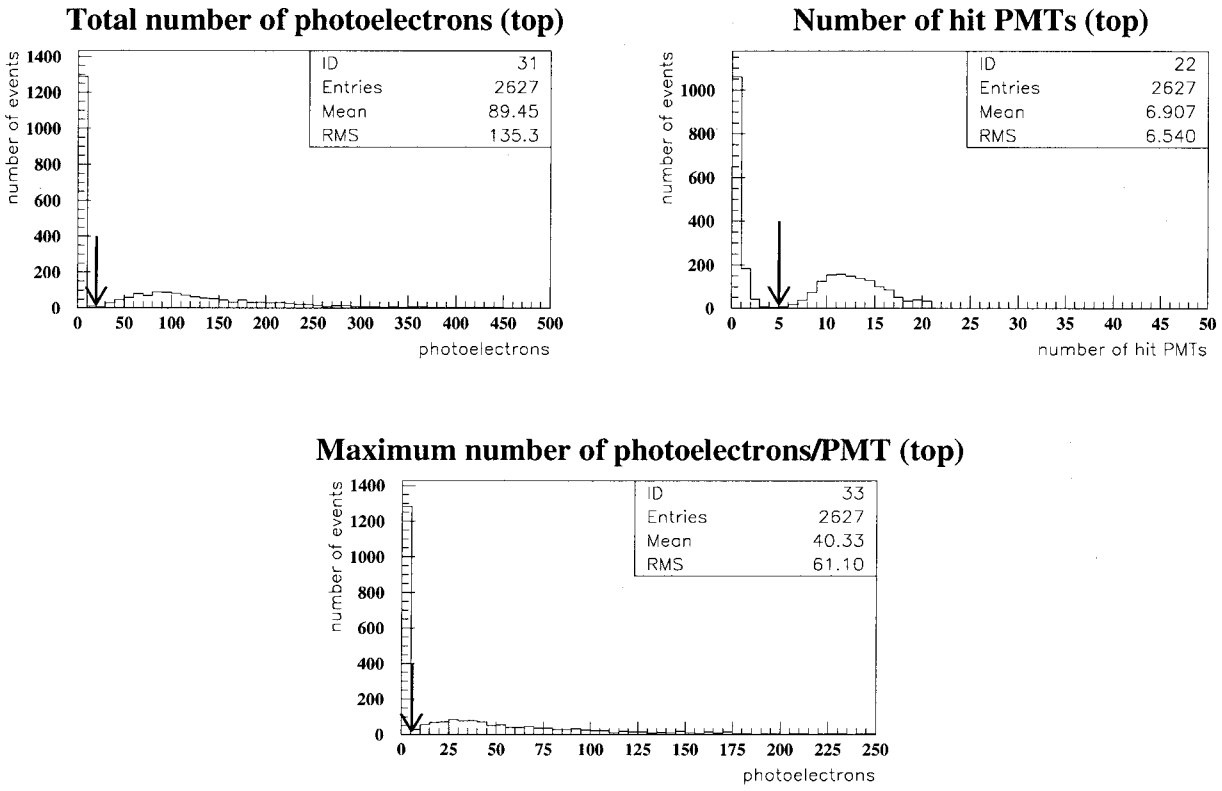

Figure 4.4: Anticounter information of top and barrel parts. The informations of another parts (barrel, bottom) are similar to this.

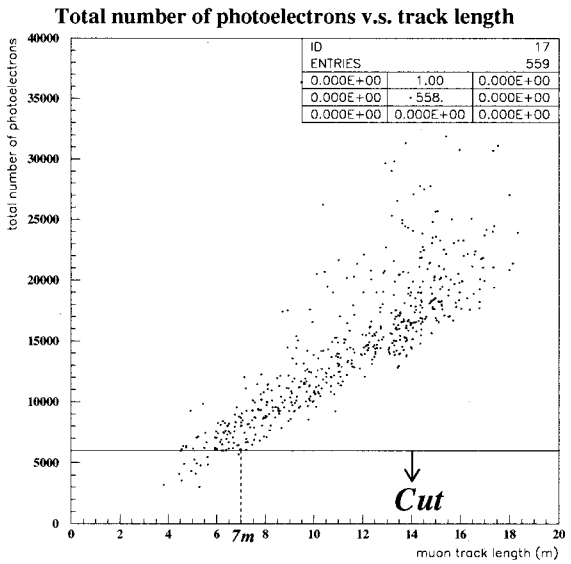

Figure 4.5: Correlation between total number of photoelectrons and the corresponding track length

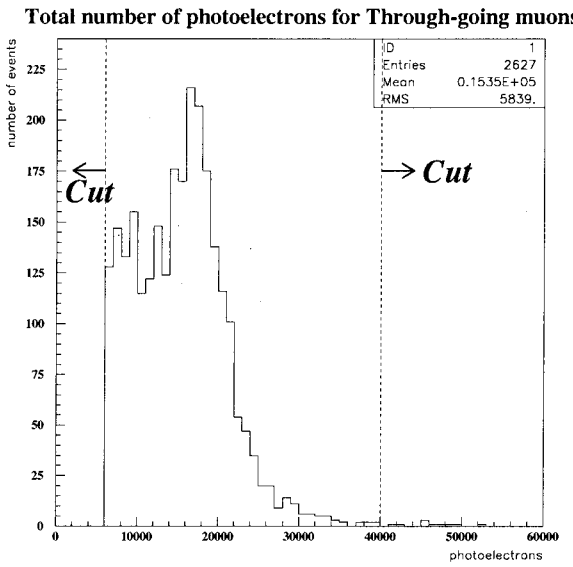

Figure 4.6: total number of photoelectrons for through-going muons yielding more than 6000 p.e.

In brief, selection criterion for the total number of photoelectrons in the inner detector is summarized as below.

$$6000\text{p.e.} \leq (\text{Total number of Photoelectrons}) \leq 40000\text{p.e.}$$

4.3 Muon direction cut

The rate of upward through-going muons detected in Kamiokande-III is about 1 event/week. To eliminate abundant downward-going muons (at 0.37 Hz), pre-reduction process (described in Appendix B) is applied as the first step and then the muon direction is required to be heading upward.

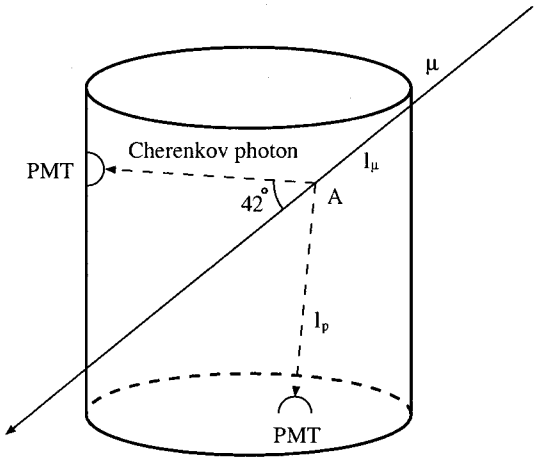

Figure 4.7: Schematic of a positional correlation between a muon and emitted Cherenkov photons

If a track is assumed to be produced by a muon, the expected photon arrival time to the i-th PMT, t_i, can be calculated in the following way. The positional correlation between a muon and a PMT within the Cherenkov cone is schematically shown in Fig. 4.7.

The muon which travels a distance l_μ with almost the light velocity c emits Cherenkov light photons along the track. The emitted photon travels a distance l_p with a velocity c/n and arrives at the PMT, where $n(= 1.344)$ is the refraction index of water. Therefore, the photon arrival time to the i-th PMT is calculated by;

$$t_i = t_0 + \frac{l_\mu}{c} + \frac{n \cdot l_p}{c} \tag{4.1}$$

where t_0 is the time when the muon enters the detector. Then t_i is compared with the measured arrival time T_i recorded by the i-th PMT. If the track reconstruction is successful and the time resolution of each PMT is negligibly small, $t_i - T_i$, should be 0 for all the PMTs inside the Cherenkov cone. However, the mean value of $t_i - T_i$ slightly shifts from 0 as is seen in Fig. 4.8. This is because the entering time of the muon can be known only from the nearest hit PMT and suffers a relatively large uncertainty.

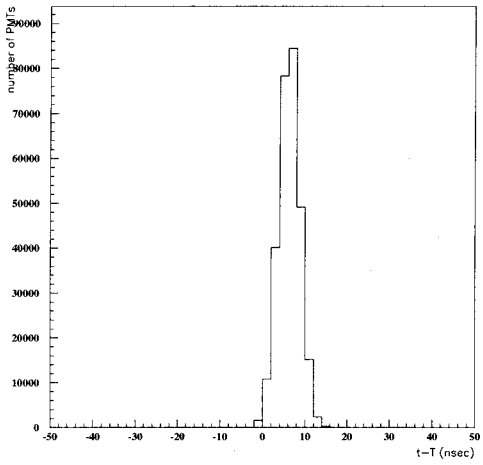

Figure 4.8: Difference between the expected photon arrival time (t_i) and the actual PMT response time deduced from TDC data (T_i) for reconstructed cosmic-ray downward through-going muon data. The mean value of $t_i - T_i$ is slightly shifted from 0, because the time of the muon entrance can be known only from the nearby PMT and has a relatively large uncertainty.

The width of the $t_i - T_i$ distribution is a good estimator to evaluate the track reconstruction quality. The width of the $t_i - T_i$ distribution, σ_T, is defined as;

$$\sigma_T = \sqrt{\frac{\Sigma_i^N (t_i - T_i - \bar{t}_0)^2}{N - 1}} \tag{4.2}$$

where $\bar{t}_0 \equiv \overline{(t_i - T_i)}$ is the mean value of the distribution and N is the total number of the PMTs used in this calculation. Initially, the entrace point of the muon was assumed as the earliest hit PMT and its direction as a vector drawn from it to the PMT which recorded the maximum number of photoelectrons. The two variables are iteratively varied till the minimum σ_T is reached.

To examine whether this reconstruction method is valid or not, another parameter, W_{pe}, is introduced. It is defined as the ratio of the sum of the total number of photoelectrons inside the Cherenkov cone to that deposited in the inner detector. Scattering plot of $\cos\Theta$ vs. W_{pe} are shown in Fig. 4.9 for the downward going muon data (a) and simulated upward going muon (b).

From Fig. 4.9, the events satisfying the following both conditions are cut.

$$W_{pe} > 0.8$$

and

$$\cos\Theta > 0.05$$

where Θ is the zenith angle with $\cos\Theta = 1$ corresponding to downward-going events.

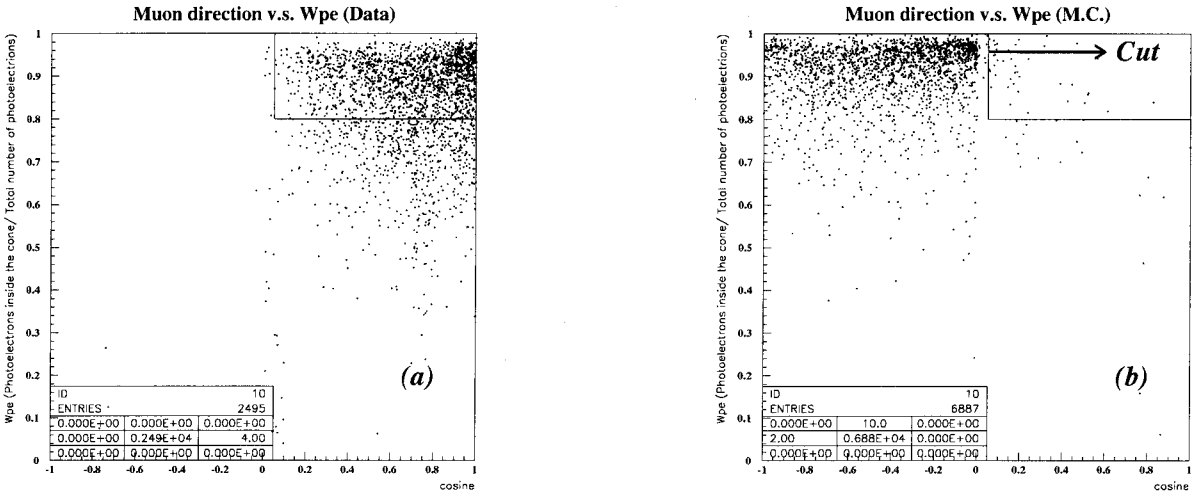

Figure 4.9: The ratio of total photoelectron within the Cherenkov cone to the total photoelectron recorded in the inner detector. (a) is for the downward cosmic-ray muon data and (b) is for the Monte Carlo upward muon events.

4.4 Visual event scanning

A total of 2.01 $\times$ 10^5 events passed through the previous data reduction steps. Despite the cut $\cos\Theta$ <0.05, the remaining events still contains a great number of downward going muons.

They contain

1. Single-track downward-going muons with nearly horizontal direction as seen in Fig. 4.10 or with relatively short track length (See Fig. 4.11) or edge-clipping muons shown in Fig. 4.14. ~70 %
2. Downward-going muons accompanied with bremsstrahlung or hadronic showers as one sees in Fig. 4.12. ~15 %
3. Multiple muon events as shown in Fig. 4.13. ~10 %
4. Muon events accompanied with hadronic shower produced by muon interacting with water in the anticounter, as shown in Fig. 4.15.~5 %
5. True upward through-going muons as shown in Fig. 4.16, Fig. 4.17.

In other words, 99.9 % of surviving events are still downward-going muons. To eliminate these events and single out upward going muons, visual scan by physicists on the display was necessary. In the visual scan, only muons with clearly downward direction were eliminated. However, muons with almost horizontal direction including those suspicious of slightly downward going were retained.

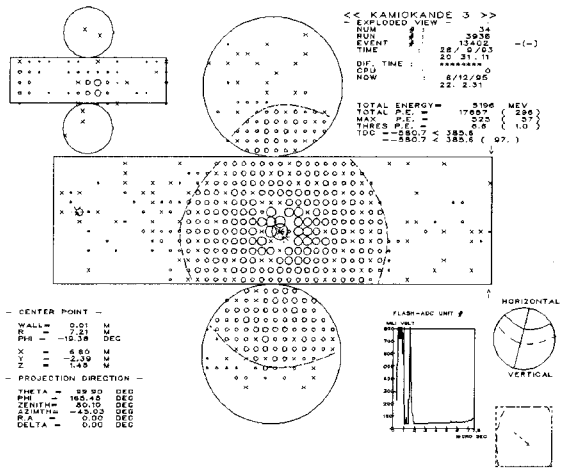

Figure 4.10: Nearly horizontal downward-going muon event

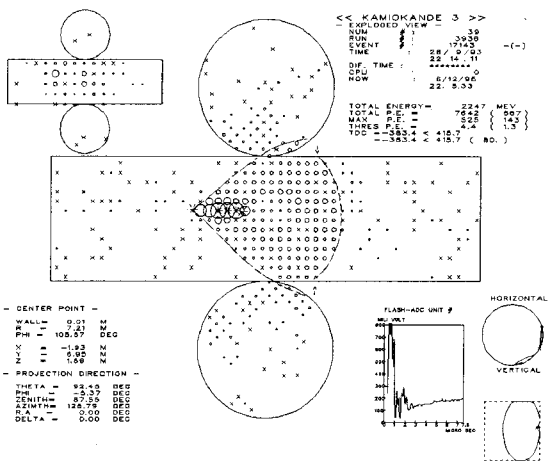

Figure 4.11: Nearly horizontal downward-going muon with relatively short track length

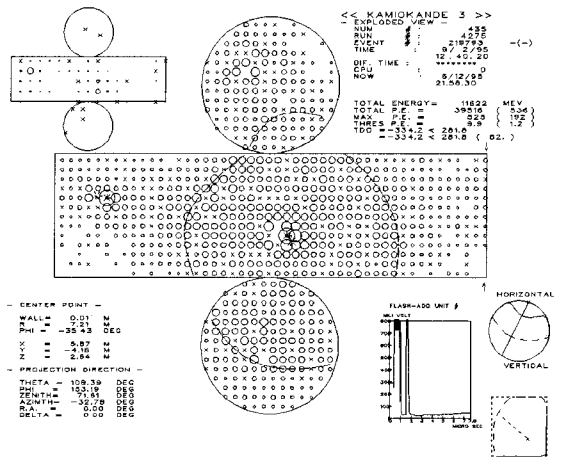

Figure 4.12: Downward-going muon with bremsstrahlung

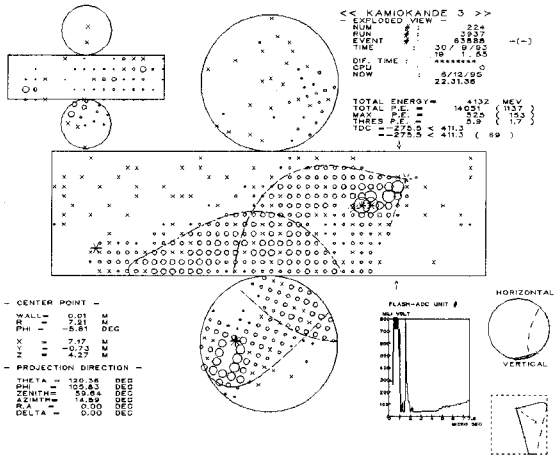

Figure 4.13: Downward-going multiple muon event

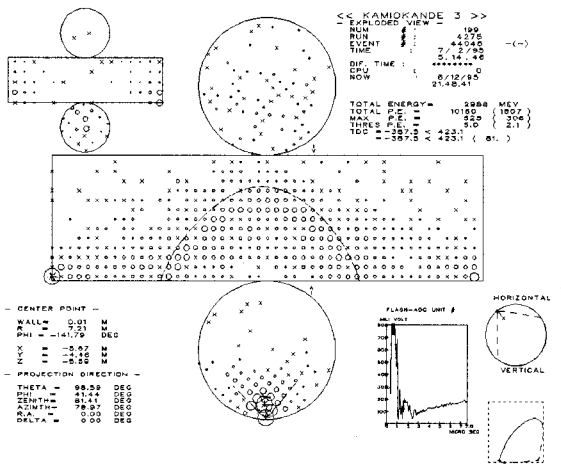

Figure 4.14: Detector edge-clipping muon event

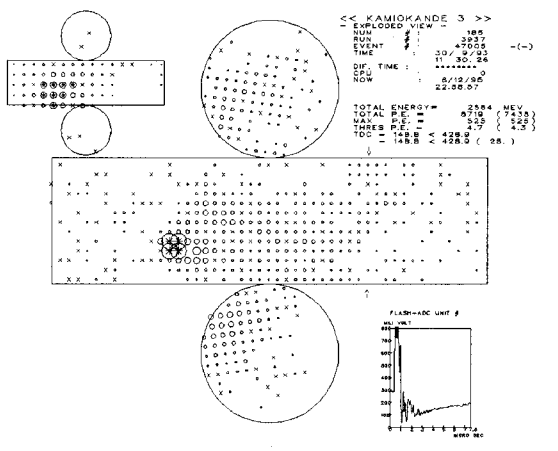

Figure 4.15: The event accompanied with hadronic shower produced by a cosmic ray muon interacting water in the anticounter.

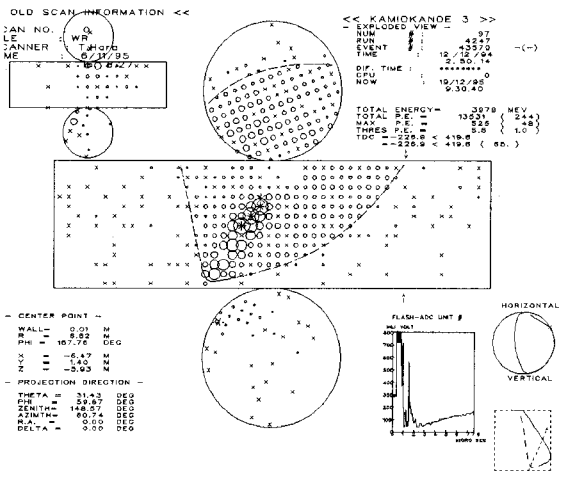

Figure 4.16: Typical upward through-going muon

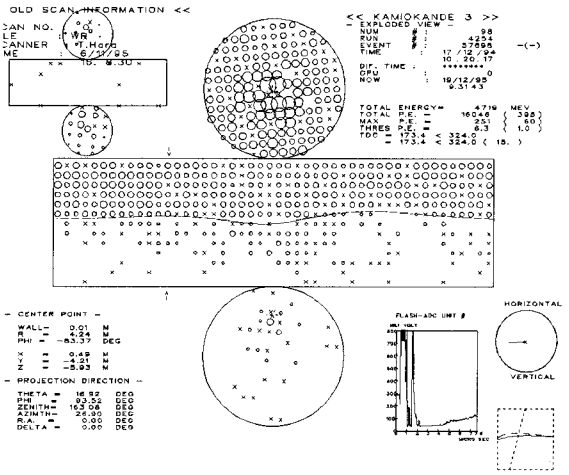

Figure 4.17: Another typical upward through-going muon event

4.5 Elimination of nearly horizontal cosmic-ray downward-going muon

During the eye scan, the muon direction was redefined manually by physicist using the display. A point at the earliest firing PMT and another one at hit PMT which recorded the maximum number of photoelectrons are set manually by physicists as the muon's entrance and exit position candidates respectively. And these processes are repeated so as to match the expected ring image to the real one. This process is called as "manual reconstruction" in the present thesis.

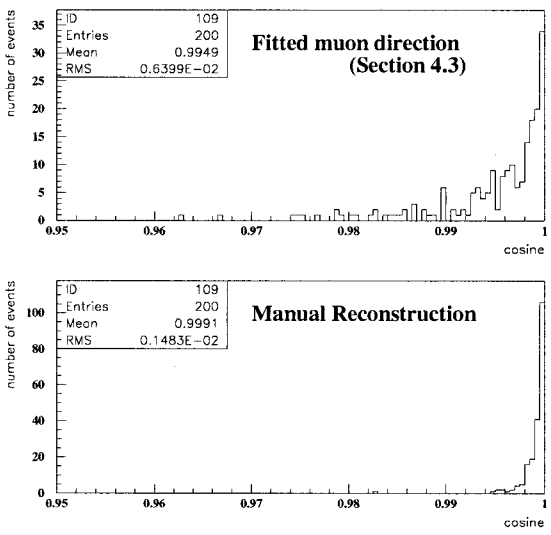

Figure 4.18: Deflected angle distribution. The horizontal axis is the cosine of the deflected angle.

To check the validity of manual reconstruction, simulated upward-going muons are reconstructed manually, and the cosine of the deflected angle (angle between generated muon direction and that defined by manual reconstruction) is shown in Fig. 4.18. For comparison, a result which is made by fitting the same simulated events by means of computer method used in section 4.3 is also shown. Figure 4.18

shows that manual reconstruction is superior to computer fitting. The angular resolution of the manual reconstruction is estimated to be $\sim 2°$ by Monte Carlo simulation. Muons with track length significantly shorter than 7 m make the spatial reconstruction ambiguous. This is the reason mentioned before to require minimum track length of 7 m (see section 4.2).

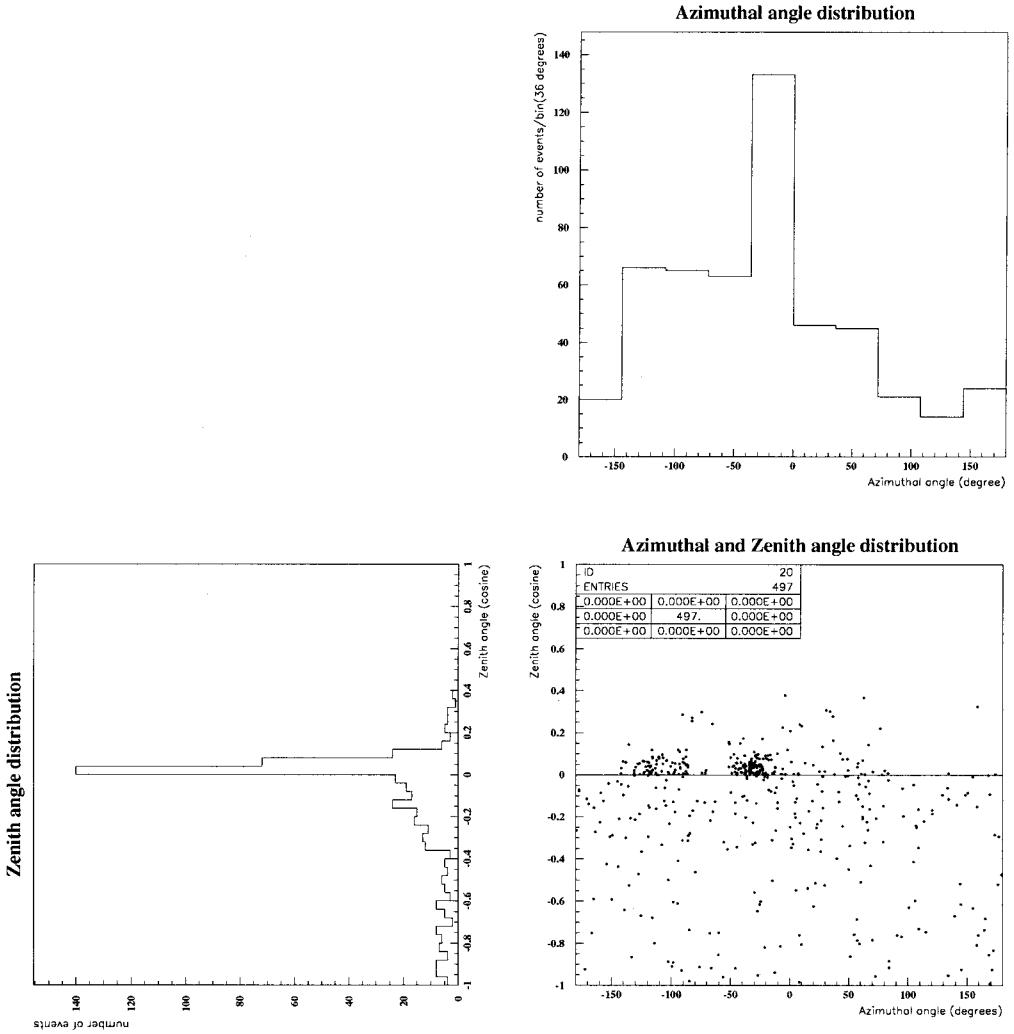

Figure 4.19: The azimuthal and zenith angle distribution of the surviving events after the track length cut (> 7 m). The upper and the left figures are projections of the scattered plot to each axis.

Figure 4.19 shows the correlation between tha azimuthal angle and the zenith angle of surviving events. As is seen in Fig. 4.19, the azimuthal angle (muon direction relative to the north. 0° and 90° correspond to the north and the west, respectively) distribution of upward through-going muon candidates indicates an apparent non-uniformity. This reflects the configuration of the ground above and nearby detector. The Kamiokande-III detector is located 1000 m underground not from the flat ground, but from the top of a mountain (1368 m). The thickness of rock overburden (defined as the distance from the detector to the surface) varies as a function of azimuth as shown in Fig. 4.20. The cosmic-ray muon flux falls off very sharply as the rock overburden increases. In the direction where the rock overburden is thinner (see ⓐ relative to ⓑ in Fig. 4.20), more muons can reach the detector.

The contribution of direct cosmic-ray muons from below should be negligible (see Fig. 4.20 ⓒ), whereas that of neutrino-induced muons (see Fig. 4.20 ⓓ) should be isotropic with respect to the azimuthal angle.

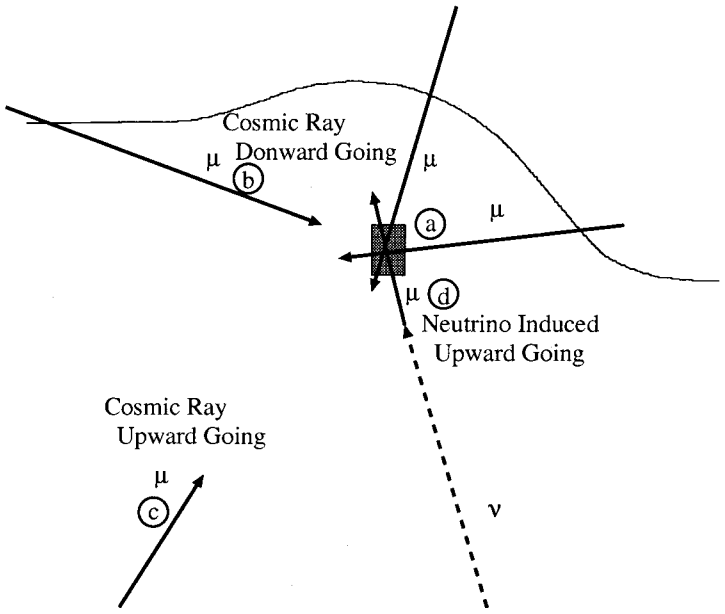

Figure 4.20: Various types of muons which head toward the detector. ⓐ :The cosmic-ray downward-going muons can reach the detector when the overburden rock layers are thin. ⓑ :The heavy overburden prevents the cosmic-ray downward-going muon from reaching the detector. ⓒ :Cosmic-ray upward-going muons, produced on the opposite side of the Earth, propagate so long a distance that they range out before reaching the detector. ⓓ :Only neutrino-induced upward-going muons can arrive at the detector and be detected as "upward-going muon".

Looking back at Fig. 4.19, we see that the anisotropy in the azimuthal angle distribution exists only in the downward angle region ($\cos\Theta > 0$). This is illustrated in Fig. 4.21, where zenith angle distributions in two different azimuthal angle regions are displayed.

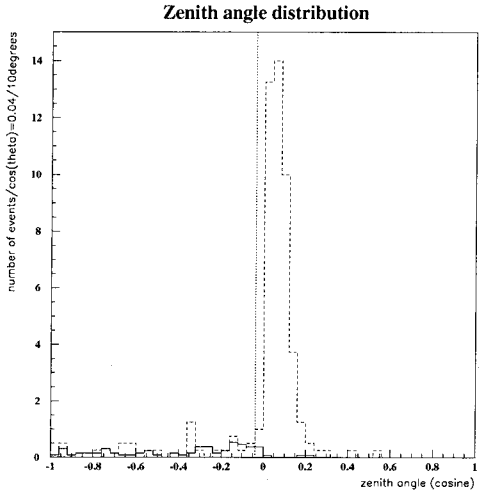

Figure 4.21: Zenith angle distribution of the surviving events after track length cut (>7 m). The solid line represents the events having azimuthal angle $-50° < \phi < -10°$. While the dashed line stands for events having $\phi > 80°$ or $\phi < -150°$. Each bin is normalized to number of events/10° (azimuthal angle).

Considering the resolution tail of angle determination ($\Delta\theta \sim 2°$), the following tighter selection is applied:

$$\cos\Theta \leq -0.04 \tag{4.3}$$

Figure 4.22 shows that the azimuthal distribution of the surviving events after cuts on track length (>7 m) and $\cos\Theta > -0.04$ is flat as expected.

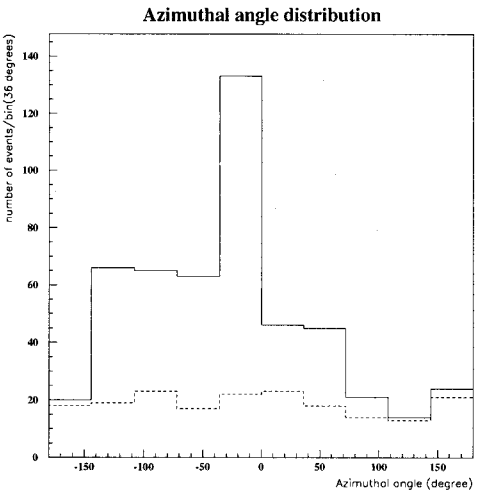

Figure 4.22: Azimuthal distribution before (solid line) and after (dashed line) $\cos\Theta < -0.04$ selection

After this selection, a total of 188 upward through-going muons are observed during the Kamiokande-III data-taking period (1332 detector livedays). Figure 4.23 and 4.24 shows the azimuthal angle distribution and the zenith angle distribution of the observed events.

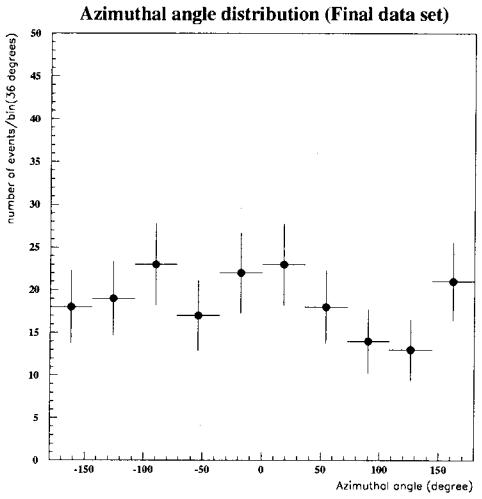

Figure 4.23: Azimuthal distribution of final data set

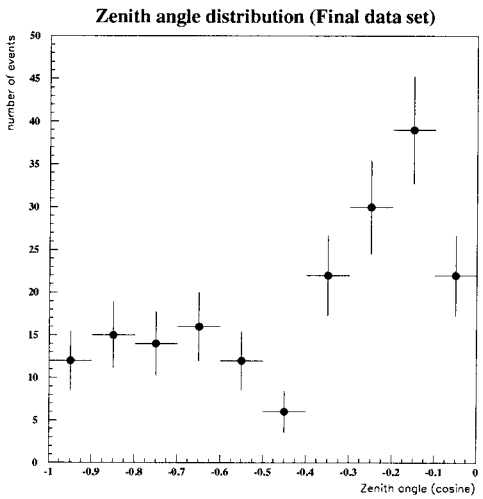

Figure 4.24: Zenith distribution of final data set

4.6 Survival efficiency

The survival efficiency, $\varepsilon(\Theta)$, for upward through-going muons in each reduction steps is estimated by a Monte Carlo simulation. To estimate the zenith angle dependence of the survival efficiency, the region $-1 \leq \cos\Theta \leq 0$ is divided into 10 bins. Each bin corresponds to 0.2π steradian or an interval of 0.1 in $\cos\Theta$, where Θ is the zenith angle. Due to the symmetry of the detector configuration with respect to upward- and downward-going events, the validity of the Monte Carlo program can be checked using the real cosmic-ray downward through-going muons.

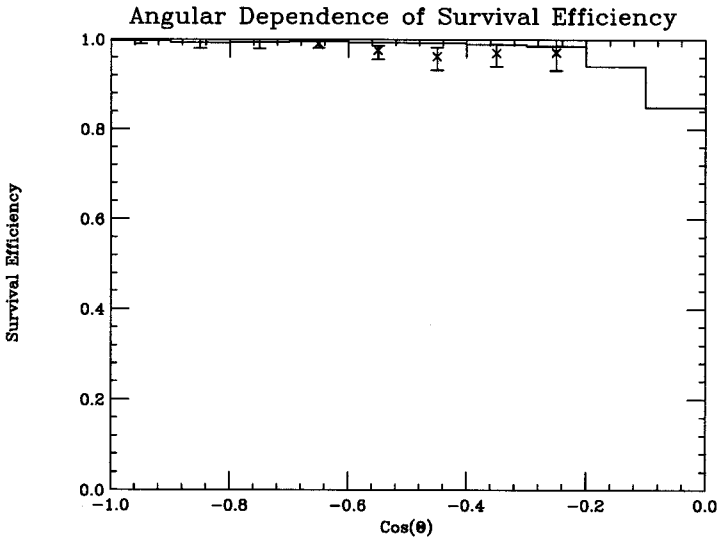

Figure 4.25: Angular dependece of the survival efficiency. The histogram stands for Monte Carlo events and the points with error bar corresponds to the downward through-going muons (real data).

The survival efficiency estimated by the Monte Carlo events for $\cos\Theta > 0.2$ is in good agreement with the estimation by the real data within statistics.

To check the scanning efficiency, another analysis group searched for upward-going muons from raw data by using different reduction software (including event scanning), independently. Comparing their muon events with those in this thesis, almost all events matched with each other. The disaccord was caused by events which were lost before event scanning. Therefore, the scanning efficiency was assumed to be $\simeq$100 %.

The zenith angle dependence of the survival efficiencies is shown in Table 4.1 and Fig. 4.25.

$\cos\Theta$	-0.95	-0.85	-0.75	-0.65	-0.55	-0.45	-0.35	-0.25	-0.15	-0.05
$\varepsilon(\Theta)$	0.997	0.993	0.994	0.996	0.993	0.992	0.989	0.985	0.940	0.849

Table 4.1: Angular dependence of the survival efficiencies for upward-going muons

Chapter 5

Observed upward through-going muon flux

A total of 188 upward through-going muons are observed by the Kamiokande-III detector during 1332 detector live days. A conversion of the obtained number to a flux requires the effective area of the detector which the muons have passed. In this chapter, extraction of the effective area of the detector for upward through-going muons is presented, and the observed flux is calculated based on the final data set given in the last chapter.

5.1 Effective area

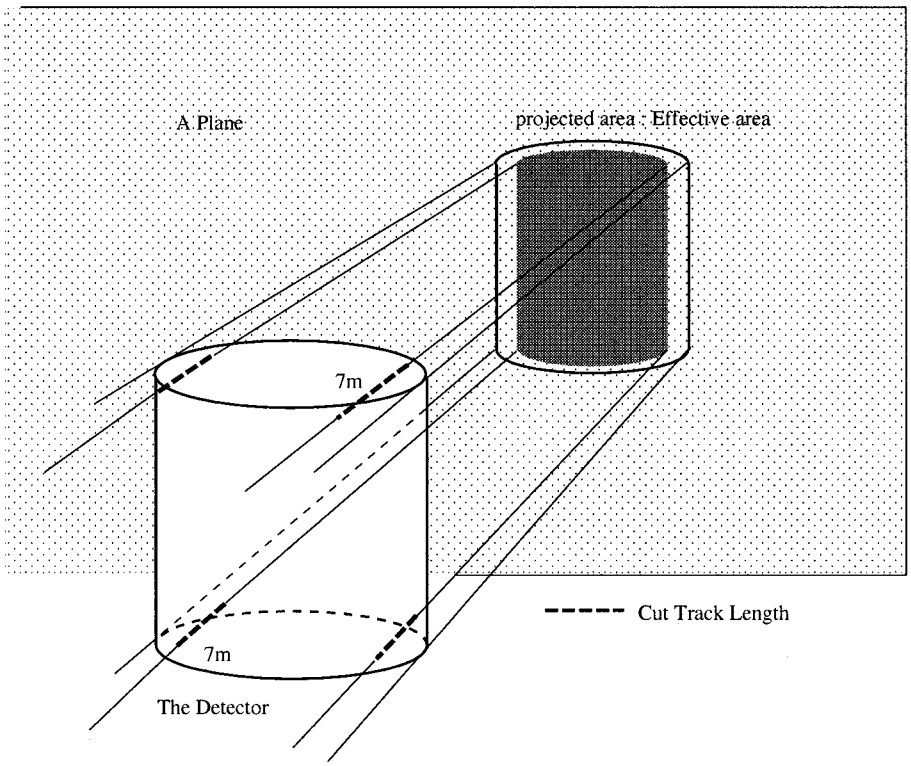

Figure 5.1: Schematics of the effective area for upward through-going muons

The effective area seen by a muon from a given direction is obtained by projecting the detector onto a plane perpendicular to the direction of the muon track. The requirement of the minimum track length (discussed in Section 4.5 and [53]) has to be taken into account. A schematic illustration of the effective area is presented in Fig. 5.1.

The calculation method is as follows. For a given direction, a large hypothetical plane perpendicular to the direction is set behind the detector. Two-dimensinal grid points are defined on this plane with every 10 cm step, and a vertical line is drawn from each point to the detector. If the intersecting length of this line through the inner detector is longer than 7 m, the corresponding grid point is registered as valid. The process is repeated for all the grid points and the effective area is defined as (the total number of valid grid points)$\times$ (100 cm^2). The resultant effective area as a function of zenith angle, $S(\Theta)$ is shown in Fig. 5.2. The average effective area is roughly 150 m^2.

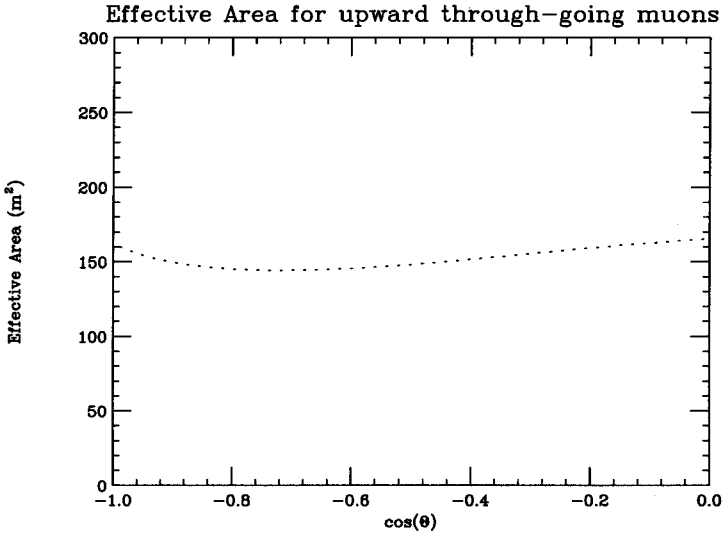

Figure 5.2: Zenith angle dependence of the effective area for upward through-going muons with track length longer than 7 m.

5.2 Calculation of upward through-going muon flux

Given the detector live time, T, the effective area for upward through-going muons, $S(\Theta)$, and the survival efficiency, $\varepsilon(\Theta)$, which has already been presented in Section 4.6, the average flux of upward through-going muons is calculated by the formula:

$$\Phi_{average} = \frac{1}{2(1-0.04)\pi T} \cdot \sum_{j}^{N} \frac{1}{\varepsilon(\Theta_j) \cdot S(\Theta_j)} \tag{5.1}$$

where the suffix j stands for each event number, $2(1-0.04)\pi$ (see Eq. 4.3) is the total solid angle covered by the detector for upward through-going muons. N corresponds to the total number of observed muon events (188 events). The statistical error of the average flux, $\sigma_{average}$, is given by $\sigma_{average} = \Phi_{average}/\sqrt{N}$.

The observed muon flux averaged over employed solid angle corresponding to $-1.0 \leq \cos\theta \leq -0.04$ in this analysis is ,

$$\Phi_{average} = (1.82 \pm 0.13(\text{stat})) \times 10^{-13}\text{cm}^{-2}\text{s}^{-1}\text{sr}^{-1}$$

The expected flux of $(2.20^{+0.39}_{-0.34}) \times 10^{-13}\mathrm{cm}^{-2}\mathrm{s}^{-1}\mathrm{sr}^{-1}$ as given in Section 3.5 is in agreement with the observed flux.

The zenith angle dependence is shown in Fig. 5.3, together with the expected flux.

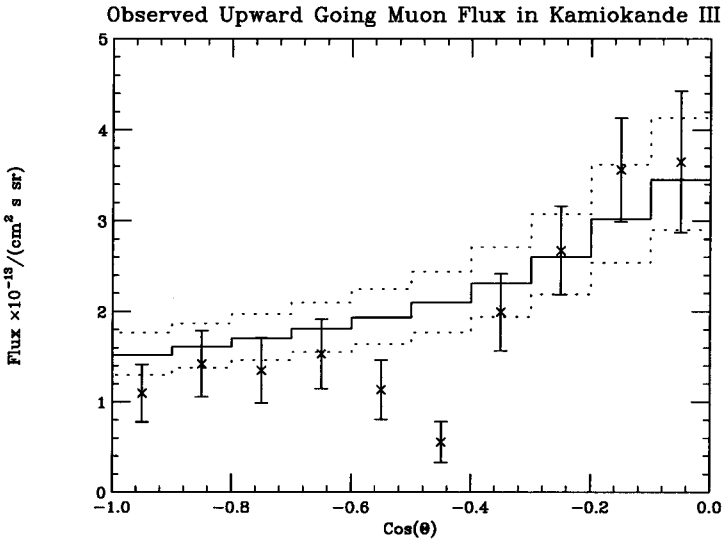

Figure 5.3: The differential flux of the observed upward through-going muons in Kamiokande-III. The solid histogram is the expected flux and the dotted histograms are the range of model variation.

The statstical errors, σ_i, in the i-th bin shown in Fig. 5.3 is calculated as

$$\sigma_i = \left(\frac{d\Phi_\mu}{d\Omega}\right)^i / \sqrt{N_i} \tag{5.2}$$

where N_i is the number of events in the i-th bin.

5.3 Systematic errors of the observed upward through-going muon flux

The main source of the experimental systematic error originates from uncertainties in the angle between the muon direction determined experimentally and the parent neutrino direction. Figure 5.4 shows a schematic view of the source of the angular uncertainties. $\Delta\theta_{\nu\mu}$ stands for μ production angle relative to ν direction in the neutrino-nucleon interaction. $\Delta\theta_{mul}$ for deflection by multiple scatterings in the rock and $\Delta\theta_{rec}$ for the uncertainty in the μ track reconstruction.

$\Delta\theta_{\nu\mu}$ depends on the parent neutrino energy and $\Delta\theta_{mul}$ depends on the muon energy. Both are unknown, for we can only measure the muon energy deposited in the detector. Therefore, the Monte Carlo technique was introduced in order to estimate this uncertainties. The details of the Monte Carlo simulation are described in Appendix C.

$\Delta\theta_{\nu\mu}$ is approximately given by [54]:

$$\Delta\theta_{\nu\mu} \sim 2.6^\circ \sqrt{\frac{100(\mathrm{GeV})}{E_\nu}} \tag{5.3}$$

where, E_ν stands for the parent neutrino energy. $\Delta\theta_{mul}$ is estimated approximately as follows:

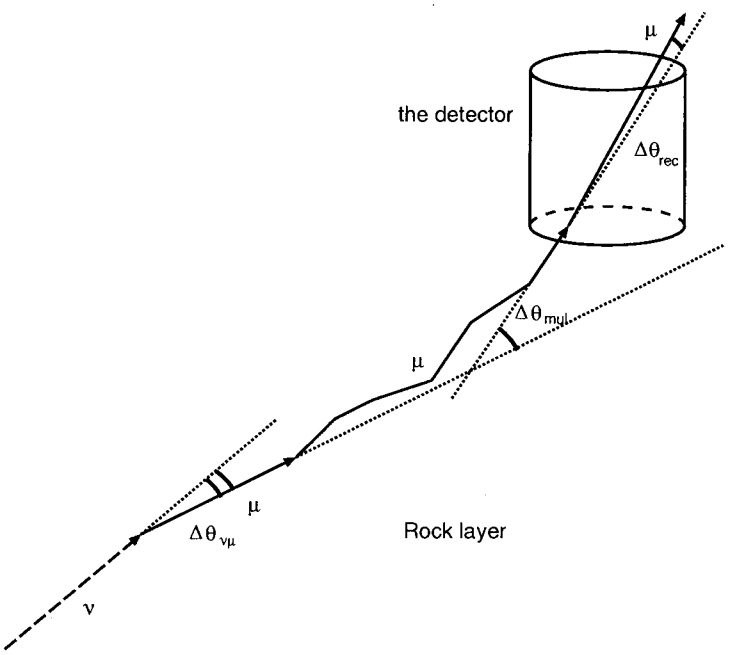

Figure 5.4: Definition of angular uncertainties, which affects the observed upward-going muon flux as systematic errors. $\Delta\theta_{\nu\mu}$ stands for the angle between ν_μ and μ produced via charged current neutrino-nucleon interaction. $\Delta\theta_{mul}$ correspond to the deflected angle caused by Coulomb multiple scatterings of the muon traversing through the rock. $\Delta\theta_{rec}$ stands for the angular uncertainty due to track reconstruction.

$$\Delta\theta_{mul} = \frac{13.6\text{MeV}}{\beta c p_\mu(\text{MeV/c})}\sqrt{\frac{x(\text{cm})}{X_0(\text{cm})}}\left[1 + 0.038\ln\frac{x(\text{cm})}{X_0(\text{cm})}\right] \tag{5.4}$$

where, p_μ and X_0(=10.5 cm) correspond to muon momentum and radiation length of the standard rock, respectively.

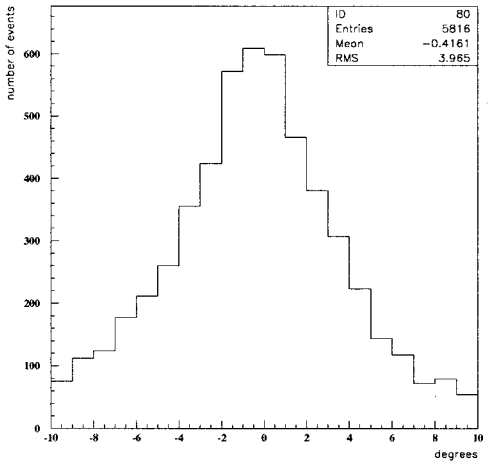

Figure 5.5: The deviation of the muon direction from the parent neutrino direction using the Monte Carlo events.

Adopting these approximations, Monte Carlo events are generated (see Appendix C).

Figure 5.5 shows the deviation of muon direction in the detector from the parent neutrino direction. The 1σ deviation, $\sqrt{\Delta\theta_{\nu\mu}^2 + \Delta\theta_{mul}^2}$, is roughly 4.1°.

The deviation between the reconstructed track direction and the real muon direction, $\Delta\theta_{rec}$, is studied using Monte Carlo events, too. The generated muon events go through the same procedure as the real events and the result is compared with the input. $\Delta\theta_{rec}$ is estimated to be 2.1° (1σ width) [53].

These angular uncertainties affect the average upward through-going muon flux by 1.6 %.

Other conceivable systematic sources are summarized in Table 5.1 together with $\Delta\theta$ $(= \sqrt{\Delta\theta^2_{\nu\mu} + \Delta\theta^2_{mul} + \Delta\theta^2_{rec}})$.

Error source	Error (%)
$\sqrt{\Delta\theta^2_{\nu\mu} + \Delta\theta^2_{mul} + \Delta\theta^2_{rec}}$	1.6
survival efficiency	0.2
7 m track length cut	0.5
live time	0.4
effective area	0.3
PMT gain	$\ll 1$
water transparency	$\ll 1$

Table 5.1: List of systematic errors

Taking these systematic errors into account, the observed average flux of upward through-going muons becomes

$$\Phi_{average} = (1.82 \pm 0.13(\text{stat}) \pm 0.03(\text{exp.sys})) \times 10^{-13}\text{cm}^{-2}\text{s}^{-1}\text{sr}^{-1}$$

5.4 Combined result of Kamiokande-III & Kamiokande-II

Finally, we combine the Kamiokande-III data with that of Kamiokande-II data [55] to get better statistics. During the Kamiokande-II experimental period (1115 detector live days), the total number of the observed upward through-going muons, whose zenith angle ($\cos\Theta$) lies between -1 and -0.04, is 185. The combined average flux is calculated as follows,

$$\Phi = \sum_{j=1}^{N} \left(\frac{1}{\varepsilon_2(\Theta_j)T_2 + \varepsilon_3(\Theta_j)T_3} \right) \cdot \frac{1}{S(\Theta_j)2(1-0.04)\pi}$$

where suffix 2 and 3 refer to Kamiokande-II and -III and other parameters are defined in Eq. 5.1. The result becomes,

$$\Phi = (1.98 \pm 0.10(\text{stat}) \pm 0.03(\text{exp. sys.})) \times 10^{-13}\text{cm}^{-2}\text{s}^{-1}\text{sr}^{-1}$$

The experimental systematic error in Kamiokande-II has not been estimated. It is assumed equal to that in Kamiokande-III, since the $\Delta\theta_{\nu\mu}$ and $\Delta\theta_{mul}$ are detector-independent and $\sqrt{\Delta\theta^2_{\nu\mu} + \Delta\theta^2_{mul}}$ (4.1°) is two times larger than $\Delta\theta_{rec}$ (2.1°).

The angular distribution of the combined result is shown in Fig. 5.6. This combined result[1] will be used for the analysis in terms of neutrino oscillations.

[1]From now on, the combined result is represented as "Kamiokande II+III" result.

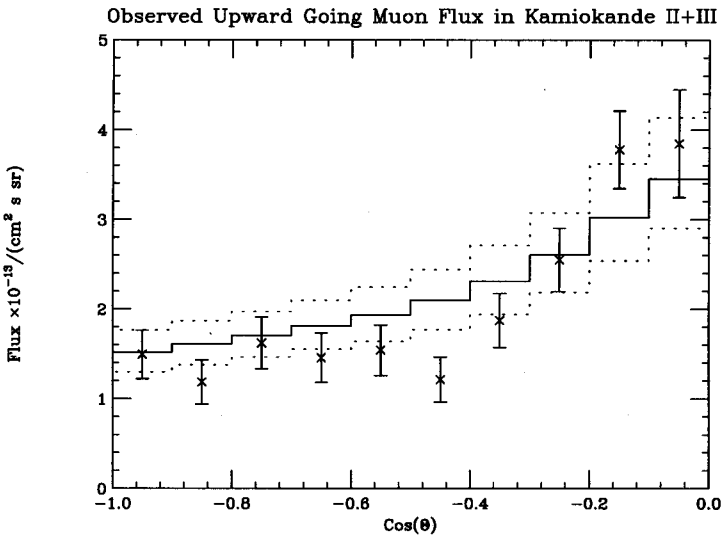

Figure 5.6: Angular distribution of upward through-going muon flux observed in Kamiokande II+III. The solid histogram shows the expected average upward through-going muon flux and the dotted line shows the range of model variation.

Chapter 6

Result and discussions

The observed upward through-going muon flux (which will be referred simply as the flux unless otherwise stated) by the Kamiokande II+III detector and corresponding expected flux were presented in Chapter 3 and 5, respectively. In this chapter, possible neutrino oscillation hypothesis will be tested using the upward through-going muons.

6.1 Upward through-going muon flux with neutrino oscillations

The observed flux in Kamiokande II+III is found to be $(1.98 \pm 0.10(\text{stat}) \pm 0.03(\text{exp.sys})) \times 10^{-13}\text{cm}^{-2}$ $\text{s}^{-1}\text{sr}^{-1}$, while the expected flux is $(2.20^{+0.39}_{-0.34}) \times 10^{-13}\text{cm}^{-2}\text{s}^{-1}\text{sr}^{-1}$. They are in good agreement within the theoretical uncertainty. For a more detailed analysis to use the differential flux, a method to calculate an expected flux distorted by neutrino oscillations should be established. The $\nu_\mu \leftrightarrow \nu_\tau$ oscillation is discussed first, and the $\nu_e \leftrightarrow \nu_\mu$ case will be described subsequently.

The probability that a neutrino born in matter as ν_μ remains ν_μ at distance L is given by

$$P_m(\nu_\mu \to \nu_\mu) = |\langle \nu_\mu | \nu_\mu(t) | \nu_\mu \rangle|^2 = 1 - \sin^2 2\theta_v \cdot \sin^2 \left(\pi \frac{L}{L_m} \right) \tag{6.1}$$

and L_m is defined in Eq. 1.21. For atmospheric neutrinos produced on the opposite side of the Earth, the propagation length, $L(\text{km})$, can be written as

$$L = 2R|\cos\Theta| \tag{6.2}$$

where R is the radius of the Earth (6371km) and Θ is the zenith angle of the neutrino arrival direction. Then, the muon neutrino flux from the opposite side of the Earth will be given by $d^2\phi_{\nu_\mu}(E_\nu, \cos\Theta)/dE_\nu d\Omega \cdot P_m(\nu_\mu \to \nu_\mu)$ instead of $d^2\phi_{\nu_\mu}(E_\nu, \cos\Theta)/dE_\nu d\Omega$. The oscillations in the air (vacuum) is neglected because travel distance is small.

The upward through-going muon flux without neutrino oscillations is already given (cf. Section 3.1) by

$$\frac{d\phi_\mu(E'_\mu, \cos\Theta)}{d\Omega} = \int_0^\infty \left[\mathcal{P}(E_\nu, E'_\mu) \cdot \frac{d^2\phi_{\nu_\mu}(E_\nu, \cos\Theta)}{dE_\nu d\Omega} \right] dE_\nu \tag{6.3}$$

If neutrino oscillations take place, the flux will be modified as:

$$\frac{d\phi_\mu(E'_\mu,\cos\Theta)_{osc}}{d\Omega} = \int_0^\infty \left[\mathcal{P}_{\nu_\mu}(E_\nu,E'_\mu)\cdot\left(\frac{d\phi_{\nu_\mu}(E_\nu,\cos\Theta)}{dE_\nu d\Omega}\cdot P_m(\nu_\mu\to\nu_\mu) + \frac{d\phi_{\nu_e}(E_\nu,\cos\Theta)}{dE_\nu d\Omega}\cdot P_m(\nu_e\to\nu_\mu)\right) + \mathcal{P}_{\overline{\nu}_\mu}(E_\nu,E'_\mu)\cdot\left(\frac{d\phi_{\nu_\mu}(E_\nu,\cos\Theta)}{dE_\nu d\Omega}\cdot P_m(\overline{\nu}_\mu\to\overline{\nu}_\mu) + \frac{d\phi_{\overline{\nu}_e}(E_\nu,\cos\Theta)}{dE_\nu d\Omega}\cdot P_m(\overline{\nu}_e\to\overline{\nu}_\mu)\right)\right] dE_\nu \tag{6.4}$$

In the case of $\nu_\mu \leftrightarrow \nu_\tau$ oscillation, $P_m(\nu_\mu\to\nu_\mu) = P_m(\overline{\nu}_\mu\to\overline{\nu}_\mu)$, while $P_m(\nu_\mu\to\nu_\mu) \neq P_m(\overline{\nu}_\mu\to\overline{\nu}_\mu)$ in the case of $\nu_e \leftrightarrow \nu_\mu$ oscillation as described in Section 1.6.

6.2 Method of flux comparison

The zenith angle distribution of the observed flux $\left(\frac{d\Phi_\mu}{d\Omega}\right)^i_{exp}$ was presented with its errors in Fig. 5.6. The expected flux for a given set of Δm^2 and $\sin^2 2\theta_v$ is calculated by Eq. 6.4 and the same binning is applied.

To test the validity of the oscillation hypothesis, a χ^2 is calculated as

$$\chi^2 = \min\left[\sum_{i=1}^{10}\left(\frac{\left(\frac{d\Phi_\mu}{d\Omega}\right)^i_{exp} - \alpha\left(\frac{d\Phi_\mu}{d\Omega}\right)^i_{osc}}{\sigma_i}\right)^2 + \left(\frac{\alpha-1}{\sigma_\alpha}\right)^2\right] \tag{6.5}$$

where σ_i is the statistical error of $\left(\frac{d\Phi_\mu}{d\Omega}\right)^i_{exp}$ (Eq. 5.2) in the i-th bin, α is an absolute normalization factor of the expected flux. Although the nature of the uncertainty in α is unknown, it is presumed that α obeys a Gaussian distribution with one standard error σ_α.

The absolute normalization error σ_α was estimated to be ± 18 % as is discussed in Section 3.5. Then, the minimium $\chi^2(\chi^2_{min})$ on the $\Delta m^2 - \sin^2 2\theta_v$ plane is searched for. The region with

$$\chi^2(\Delta m^2, \sin^2 2\theta_v) < \chi^2_{min} + 4.6 \tag{6.6}$$

is allowed at 90 % C.L. and the corresponding contour is drawn on the $\Delta m^2 - \sin^2 2\theta_v$ plane[1].

6.3 Implication of neutrino oscillations

6.3.1 Kamiokande-III data

$\nu_e \leftrightarrow \nu_\mu$ oscillation

In the case of $\nu_e \leftrightarrow \nu_\mu$ oscillation, the MSW effect should be taken into considerations. Assuming Δm^2 is positive as discussed in the footnote of Section 1.6, the MSW effect enhances neutrino oscillations for neutrinos and suppress them for antineutrinos, as is seen in Eq. 1.22. The radial distribution of the

[1]Characteristics of χ^2 distribution with multi free parameters is discussed in [52].

terrestrial density ρ_{Earth} ranging from 2.6 to 13 g/cm^2 was shown in Fig. 1.7. The relation $\rho_e = 0.5\rho_{Earth}$ is assumed in every part of the Earth.

The minimum χ^2 (χ^2_{min}=27.51) takes place at $\Delta m^2 = 3.17 \times 10^{-2}$eV^2, $\sin^2 2\theta_v = 0.30$ and α=0.85. The zenith angle distribution for the best fit parameters is shown in Fig. 6.1 together with the observed flux and the 90 % C.L. excluded region contours are drawn in Fig. 6.2.

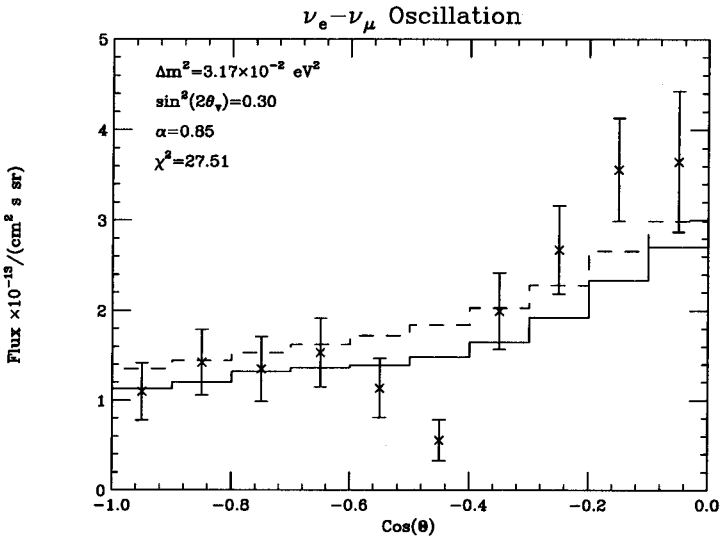

Figure 6.1: Zenith angle distribution with $\nu_e \leftrightarrow \nu_\mu$ oscillation taken into account (solid). Data : Kamiokande-III only. The null oscillation case (dashed line) is also shown for comparison. These histograms are fitted to the data under each assumption.

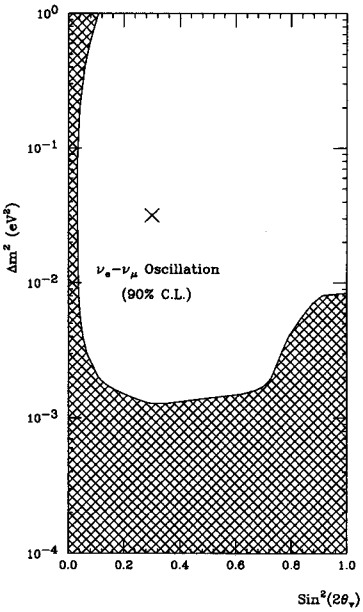

Figure 6.2: The excluded regions at 90 % C.L. obtained from the Kamiokande-III result drawn on the ($\sin^2 2\theta_v$, Δm^2) plane for $\nu_e \leftrightarrow \nu_\mu$ oscillation. Statistical and systematic errors are taken into account. The cross point represents the best fit point and the cross-hatched area is the excluded region derived by this analysis.

Though the χ^2 gives 27.51 for 9 degree-of-freedom[2], this is caused by the data point of which zenith angle is $-0.5 < \cos\Theta < -0.4$. From Fig. 4.25 and Table 4.1, the survival efficiency for upward through-going muons in this bin is ~100 %. Therefore, this dip is considered as the statistical fluctuation. In this case, it is need to increase statistic.

$\nu_\mu \leftrightarrow \nu_\tau$ oscillation

In the case of $\nu_\mu \leftrightarrow \nu_\tau$ oscillations, it is sufficient to merely consider vacuum oscillations described in Chapter 1. The minimun χ^2 (χ^2_{min} = 24.13) occurs at $\Delta m^2 = 7.00 \times 10^{-3}$eV^2, $\sin^2 2\theta_v = 1.00$ and

[2]10 independent bins minus 1, since the average value for each data point is used as a constraint.

α=1.06. The zenith angle distribution of $\alpha(d\Phi_\mu/d\Omega)^i_{osc}$ for the best fit parameters is shown in Fig. 6.8 together with the experimental data. Since vertically upward-going atmospheric neutrino propagates longer distance than horizontally one, the flux of vertically upward-going muon is more susceptible to the effect of neutrino oscillation. Therefore, the zenith angle dependence with oscillation assumption is steeper than that without oscillation.

The zenith angle distribution for the best fit parameters is shown in Fig. 6.3 together with the observed flux and Fig. 6.4 shows the excluded region at 90 % C.L. for $\nu_\mu \leftrightarrow \nu_\tau$ oscillation.

Though the χ^2 gives 24.13 for 9 degree-of-freedom, this is considered as the result of the statistical fluctuation, again.

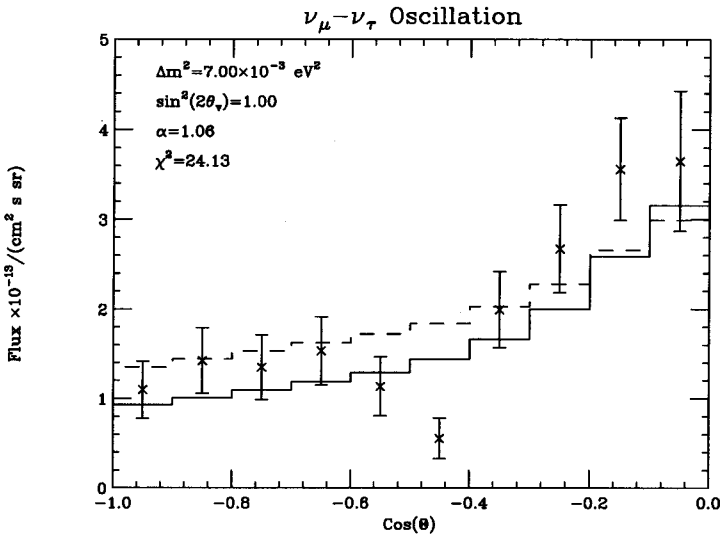

Figure 6.3: Zenith angle distribution with $\nu_\mu \leftrightarrow \nu_\tau$ oscillation taken into account. Data : Kamiokande-III only. The solid and dashed histograms represent the $\nu_\mu \leftrightarrow \nu_\tau$ oscillation and the null oscillation, respectively. These histograms are fitted to the data under each assumption.

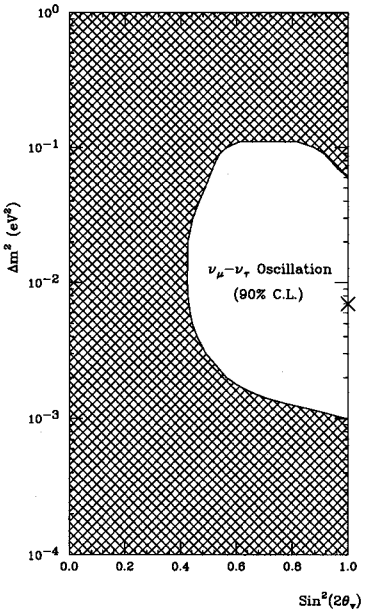

Figure 6.4: The excluded regions at 90 % C.L. obtained from the Kamiokande-III result drawn on the ($\sin^2 2\theta_v$, Δm^2) plane for $\nu_\mu \leftrightarrow \nu_\tau$ oscillation. The cross point represents the best fit point and the cross-hatched area is the excluded regions derived by this analysis.

6.3.2 Comparison with Kamiokande-II

In the previous analysis of the upward through-going muons in the Kamiokande-II [53], the angular uncertainties were not taken into considerations and the selection criteria for the zenith angle was set to $\cos\Theta < 0.0$ as compared to Kamiokande-III $\cos\Theta < -0.04$. In order to reduce the statistical fluctuation,

it is required to combine Kamiokande-II results and those from Kamiokande-III. Therefore we selected the upward-going muons recorded during the Kamiokande-II period, of which $\cos\Theta$ is less than -0.04, and reanalyzed them, taking angular uncertainties into account.

The results derived with Kamiokande-II data alone are shown in Fig. 6.5. Only the large $\Delta m^2(\sim 1\mathrm{eV}^2)$ and large mixing angle ($\sin^2 2\theta \sim 1.0$) region was excluded. By combining the Kamiokande II and III data, the statistics was doubled and the zenith angle distribution was obtained.

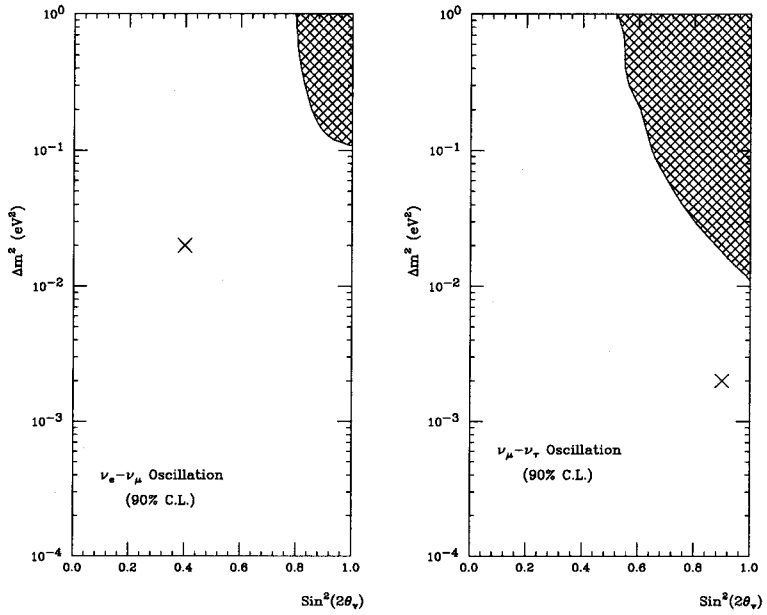

Figure 6.5: The excluded regions at 90 % C.L. obtained from the Kamiokande-II result. Errors are only statistical. The cross point represents the best fit point and the hatched area stands for the excluded region.

6.3.3 Kamiokande II+III combined result

$\nu_e \leftrightarrow \nu_\mu$ oscillation

The minimum χ^2 (χ^2_{min}=13.71) takes place at $\Delta m^2 = 3.17 \times 10^{-2}\mathrm{eV}^2$, $\sin^2 2\theta_v = 0.33$ and α=1.02. The zenith angle distribution for the best fit parameters is shown in Fig. 6.6 together with the observed flux.

The probability that the χ^2 gives at 13.71 for 9 degree-of-freedom is ~14 %.

The 90 % C.L. excluded region contours are drawn in Fig. 6.7. We found that the large mixing angle ($\sin^2 2\theta \simeq 1.0$) and the large Δm^2 ($10^{-1} < \Delta m^2 < 1\mathrm{eV}^2$) region is excluded. This result is consistent with the previous Kamiokande results using "contained events".

$\nu_\mu \leftrightarrow \nu_\tau$ oscillation

The minimun χ^2 ($\chi^2_{min} = 11.25$) occurs at $\Delta m^2 = 2.80 \times 10^{-3}\mathrm{eV}^2$, $\sin^2 2\theta_v = 1.00$ and α=1.13. The zenith angle distribution of $\alpha(d\Phi_\mu/d\Omega)^i_{osc}$ for the best fit parameters is shown in Fig. 6.8 together with the experimental data. The probability that the χ^2 gives 11.25 for 9 degree-of-freedom is ~26 %.

Figure 6.9 shows the excluded region at 90 % C.L. for $\nu_\mu \leftrightarrow \nu_\tau$ oscillation. We found that the zenith angle dependence is in favor of the oscillation hypothesis and supports the previous Kamiokande results

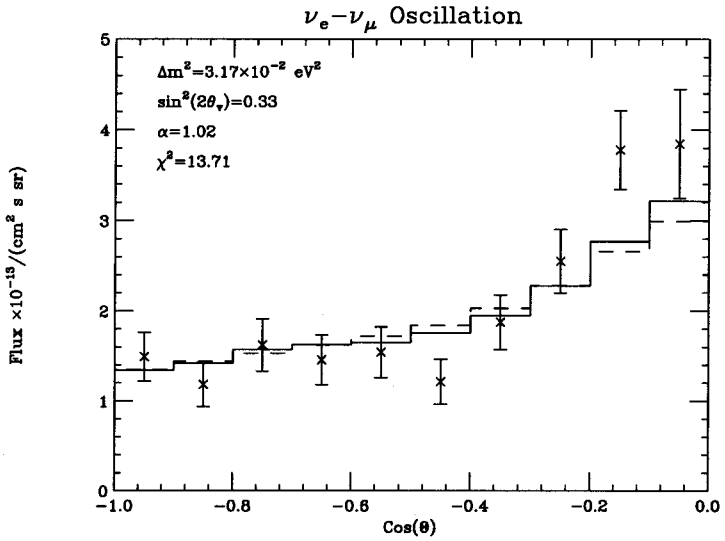

Figure 6.6: Zenith angle distribution with $\nu_e \leftrightarrow \nu_\mu$ oscillation taken into account (solid). Data : Kamiokande II+III combined. The null oscillation case (dashed line) is also shown for comparison. These histograms are fitted to the data under each assumption.

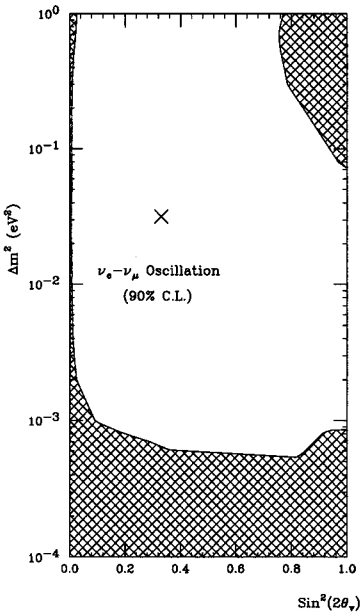

Figure 6.7: The excluded regions at 90 % C.L. obtained from the Kamiokande II+III combined result drawn on the ($\sin^2 2\theta_v$, Δm^2) plane for $\nu_e \leftrightarrow \nu_\mu$ oscillation. Statistical and systematic errors are taken into account. The cross point represents the best fit point and the cross-hatched area is the excluded region derived by this analysis.

using "contained events".

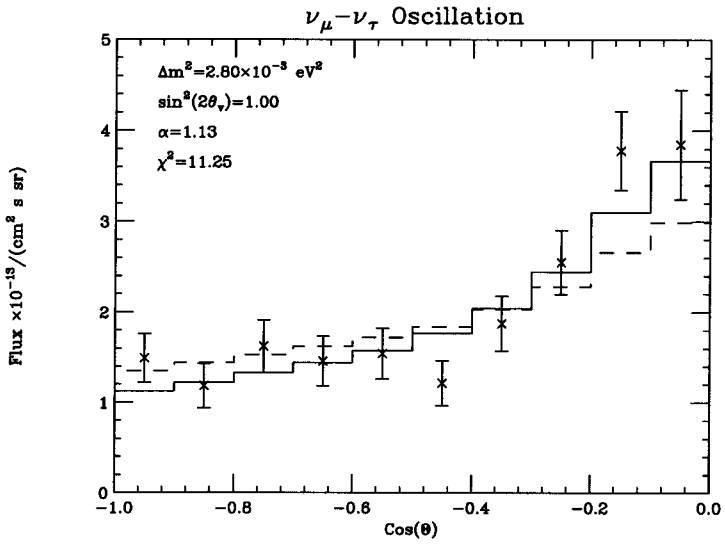

Figure 6.8: Zenith angle distribution with $\nu_\mu \leftrightarrow \nu_\tau$ oscillation taken into account. Data : Kamiokande II+III combined. The solid and dashed histograms represent the $\nu_\mu \leftrightarrow \nu_\tau$ oscillation and the null oscillation, respectively. These histograms are fitted to the data under each assumption.

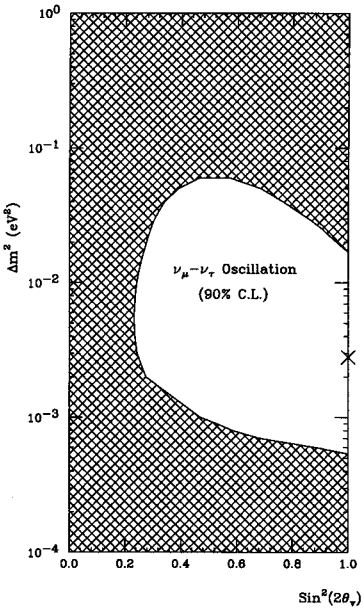

Figure 6.9: The excluded regions at 90 % C.L. obtained from the Kamiokande II+III combined result drawn on the ($\sin^2 2\theta_v$, Δm^2) plane for $\nu_\mu \leftrightarrow \nu_\tau$ oscillation. The cross point represents the best fit point and the cross-hatched area is the excluded regions derived by this analysis.

6.4 Copmarison with previous experiments

In this section, our result is compared with previous neutrino oscillation experiments.

6.4.1 $\nu_e \leftrightarrow \nu_\mu$ oscillation

The present best negative constraints on the $\nu_e \leftrightarrow \nu_\mu$ oscillation parameters is given by Gösgen experiment [56]. The Gösgen experiment employed electron antineutrinos of energies up to 8 MeV emitted from the core of a light water power reactor. Reaction $\overline{\nu}_e + p \rightarrow e^+ + n$ is detected with detectors which consist of sandwiches of scintillation cells and ^{3}He wire chambers located 37.9 m and 45.9 m from the core of the reactor. The event rate was consistent with no oscillation and $\Delta m^2 \geq 0.016$ eV^2 (90 % C.L.) is excluded for the maximum mixing and $\sin^2 2\theta_v \geq 0.16$ (90 % C.L.) is excluded for large Δm^2.

A positive result for $\nu_e \leftrightarrow \nu_\mu$ oscillation was previously obtained by Kamiokande-II and Kamiokande-III using "contained events" [12]. Both fully-contained events and the partially-contained events were employed. In this "contained" event analysis, the double ratio $(\mu/e)_{data}/(\mu/e)_{MC}$ was obtained as $0.57^{+0.08}_{-0.07}\pm0.07$, and the zenith-angle dependence of this ratio (see Fig. 6.10) provided a positive constraint in the neutrino oscillation parameter space.

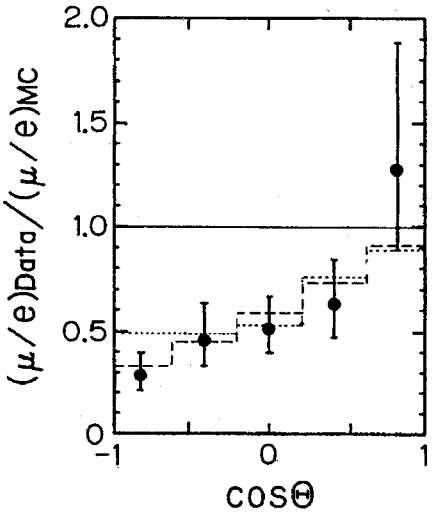

Figure 6.10: Zenith angle distribution of $(\mu/e)_{data}/(\mu/e)_{MC}$, where both fully- and partially-contained events are included. The circles with error bars show the data (Kamiokande II+III). Also shown are the expectation from the MC simulations with neutrino oscillations for parameter sets $(\Delta m^2, \sin^2 2\theta_v)$ corresponds to the best-fit values to the data for $\nu_e \leftrightarrow \nu_\mu$ ($(1.8\times10^{-2}\mathrm{eV}^2, 1.0)$, dashes) and $\nu_\mu \leftrightarrow \nu_\tau$ ($(1.6\times10^{-2}\mathrm{eV}^2, 1.0)$, dots) oscillations.

The constraints on the oscillation parameters are shown in Fig. 6.11 and the regions inside the dashed line give the 90 % C.L. allowed regions. According to these results, only black region are left as an allowed one.

Our new result using upward through-going muons does not reduce the already allowed region, but it confirms that the positive effect observed in the low energy region (E_ν : 1 $\sim$ 10 GeV) is also real in the high energy region ($E_\nu \sim 100$ GeV).

6.4.2 $\nu_\mu \leftrightarrow \nu_\tau$ oscillation

Kamiokande reports a positive result based on "contained event" analysis [12]. The sizable zenith angle dependence is again observed (see Fig. 6.10). The region inside of the dashed-curve gives the allowed regions for $\nu_\mu \leftrightarrow \nu_\tau$ oscillation.

The dot-dashed curve in Fig. 6.11 is given by the CDHSW experiment [31]. The region above the line is excluded. They used a ν_μ beam around 1 GeV which is made from the 19.7 GeV/c CERN Proton Synchrotron proton beam. Two detectors which are made of sandwiches of iron plates and plastic scintillator hodoscopes are located 130 m and 885 m downstream from the neutrino source. Muons generated by charged current interactions are measured, and the neutrino fluxes at the two location are compared. The result is consistent with no-oscillation.

Another negative result is provided by the IMB experiment(U.S.A) using upward-going muons [8]. The IMB detector is of the same type as the Kamiokande detector (ring-imaging water Cherenkov detector). They observed the upward through-going muons and upward-stopping muons simultaneously. The ratio of the latter to the former as a function of energy is used to search for possible neutrino oscillations. The IMB collaboration reported no evidence for oscillations and the excluded region is shown as that inside the dot-dash-dashed line in Fig. 6.11. Figure 6.12 shows the angular distribution of the observed upward through-going muons in the IMB detector. Recently, Lipari claimed that the neutrino-nucleon

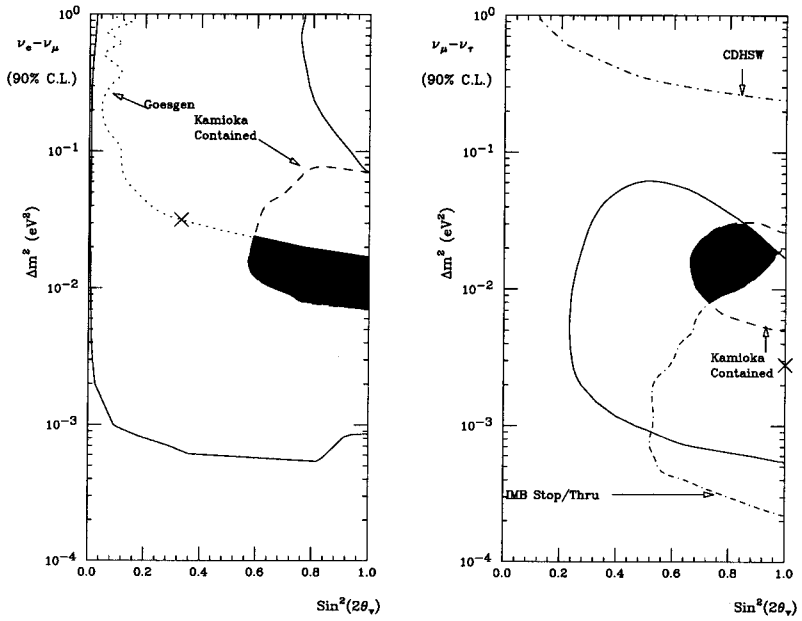

Figure 6.11: The excluded regions at 90 % C.L. obtained from the Kamiokande II+III combined result with other experiments. Only filled area in each figure is left as an allowed region. The cross point represents the best fit point derived from this experiment.

cross-section they used in this analysis considered only the deep inelastic scatterings [57]. Furthermore, they did not apparently estimate the experimental systematic errors.

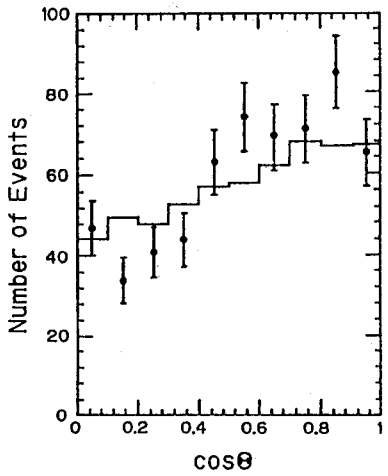

Figure 6.12: Zenith angle distribution of upward through-going muons observed in the IMB detector. The histograms is calculated from Volkova's flux.

At present, two experiments other than Kamiokande and IMB reported measurement of the upward through-going muon flux (see Table 6.1).

The result from the Baksan neutrino telescope(Russia) is shown in Fig. 6.13 [59]. They only used events with $\cos\Theta < -0.6$, i.e., vertically upward through-going muons, to calculate the flux and to seach for neutrino oscillations. Their result is shown in Table 6.1 and Fig. 6.13, but no constraint in the $\Delta m^2 - \sin^2 2\theta_v$ plane has been reported.

Lately, the Macro experiment (Italy) reported the upward through-going muon flux,too [60]. Figure 6.14 shows the angular distribution of upward through-going muons observed in the Macro detector. Macro detector has a very large effective area for vertically upward through-going muons, but for horizontally muons, it is small. Therefore, the statistical uncertainty is large in the horizontal region (see

Experiment	Observed	Expected
Kamiokande[a]	$(1.93 \pm 0.10 \pm 0.03) \times 10^{-13}\mathrm{cm}^{-2}\mathrm{s}^{-1}\mathrm{sr}^{-1}$	$(2.20^{+0.39}_{-0.34}) \times 10^{-13}\mathrm{cm}^{-2}\mathrm{s}^{-1}\mathrm{sr}^{-1}$
IMB[b]	617 events	600.0 events
Baksan[c]	$(2.75 \pm 0.15) \times 10^{-13}\mathrm{cm}^{-2}\mathrm{s}^{-1}\mathrm{sr}^{-1}$	$(2.50 \sim 2.84) \times 10^{-13}\mathrm{cm}^{-2}\mathrm{s}^{-1}\mathrm{sr}^{-1}$
MACRO[d]	74 ± 9(stat) $\pm$ 8(sys)events	101 ± 15(sys)events

Table 6.1: Summary of upward-going muon. a:this experiment, b:[58], c:[59] and d:[60].

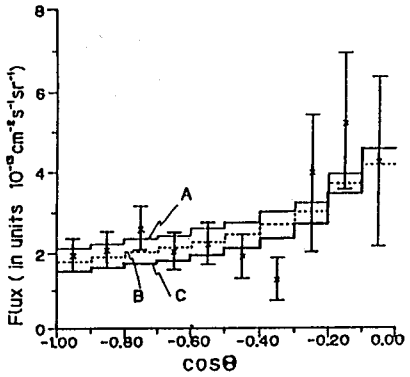

Figure 6.13: Zenith angle distribution of upward through-going muons observed in the Baksan detector. The histograms, A, B and C are calculated from Volkova's flux, Butkevitch's flux, and the $\nu_\mu \leftrightarrow \nu_\tau$ oscillations with $\Delta m^2 = 0.01\mathrm{eV}^2$ and $\sin^2 2\theta_v = 0.8$, respectively. $\cos\Theta = -1.0$ corresponds to upward. The events with $\cos\Theta > -0.6$ are omitted.

Fig. 6.14). They only estimated systematic errors of detector origin, but not the errors caused by the neutrino-nucleon interactions. They can not quote possible neutrino oscillations at the 90 % C.L., because of the large experimental uncertainty.

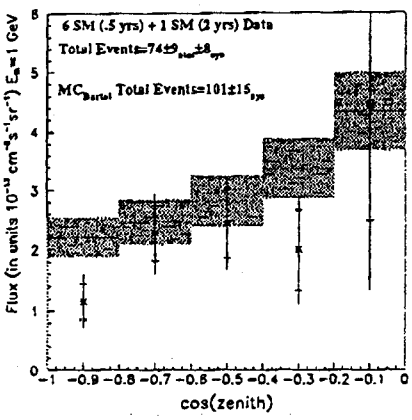

Figure 6.14: Zenith angle distribution of upward through-going muons with energy larger than 1 GeV observed in the Macro detector. The histograms is calculated from the Gaisser's flux. The extensions of the statistical error bars are the point-by-point estimates of the systematic error.

In summary, only Kamiokande-II and Kamiokande-III have given consistently positive signals on the neutrino oscillation. All other groups that have measured atmospheric neutrinos do not confirm nor deny Kamiokande result derived from the contained event analysis.

Though our result can not extend the already excluded regions effectively, we find that the zenith angle dependence of the upward through going muons is consistent with the neutrino oscillation interpretations. The result of this thesis supports the contained event analysis of the Kamiokande.

6.5 Future prospect

The absolute flux of the observed upward through-going muon is in good agreement with the theoretical expectation, but the theoretical ambiguity in the absolute flux value is large (~18 %). This

ambiguity is mainly caused by the uncertainties in the primary cosmic-ray flux and modeling of the neutrino production. In the case of contained events, both electrons and muons can be obtained. By taking the double ratio $(\mu/e)_{data}/(\mu/e)_{MC}$, the systematic uncertainty is largely canceled. For upward through going muons, the double ratio can not be obtained. However, in the future, one can measure the (upward-stopping muon)/(upward through-going muon) fraction, which cancel out much of the theoretical uncertainties.

All the measurements that have been done with Kamiokande can be repeated with the next-generation experiment, i.e., "Super-Kamiokande[3]", more sensitively and precisely.

In this section, the future prospect for observations of upward-going muons in the Super-Kamiokande is presented.

6.5.1 Expected upward-going muon flux in Super-Kamiokande

The parameters and performances of the Super-Kamiokande detector is summarized in Table 6.2, together with the Kamiokande detector. As can be seen from Table 6.2, the Super-Kamiokande detector is much bigger than and superior to the Kamiokande detector.

The expected event rate of the upward-going muons also increase significantly.

Figure 6.15 shows the effective area of the Super-Kamiokande detector (dashed-line) for the upward-going muon with track length longer than 7 m together with that of the Kamiokande detector (solid-line), for comparison.

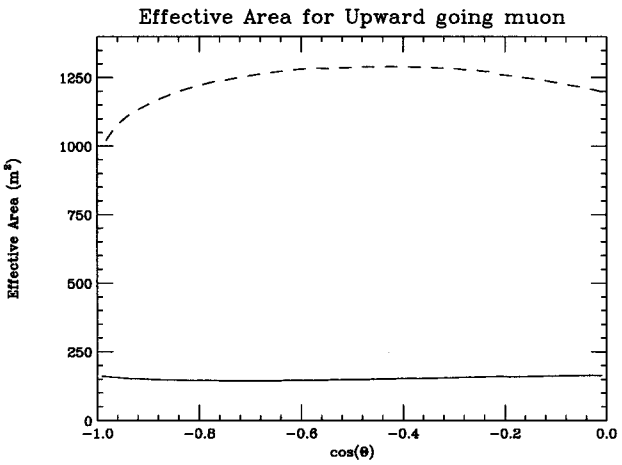

Figure 6.15: Effective area as a function of zenith angle for the upward-going muons with track length longer than 7 m in the Super-Kamiokande detector (dashed-line) together with the Kamiokande's effective area (solid-line). The upward direction is given by $\cos\Theta = -1$.

Using this effective area, the expected upward-going (through-going and stopping) muon event rate can be estimated. Figure 6.16 shows the expected number of events The expected event rate is 616.9 events/year[4] in Super-Kamiokande, which is roughly 9 times larger than that in Kamiokande (67.1 events/year).

6.5.2 Upward-stopping muon fraction in the Super-Kamiokande

In the Super-Kamiokande, upward-stopping muons will be observed together with upward through-going muons. Upward-stopping muons are produced by relatively low-energy atmospheric neutrinos. Fig-

[3]Super-Kamiokande started data-taking in April 1996.

[4]Of which 424.5 events/year for through-going muons and 192.4 events/year for stopping muons.

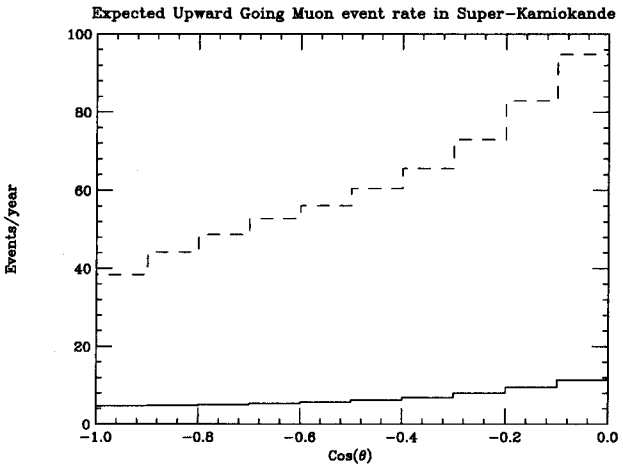

Figure 6.16: Expected number of the upward-going muons. The dashed-line corresponds to Super-Kamiokande and also shown is the event rate in Kamiokande as solid-line. This is calculated using the Honda's atmospheric neutrino flux, the CTEQ quark distribution and the Lohmann's muon energy loss. Minimum muon track length is set to 7 m.

Parameters	Super-Kamiokande	Kamiokande	Remarks
Total size	42mh×39mϕ	16.1mh×15.6mϕ	
Total mass	50,000t	4,500t	
Fiducial mass	32,000t	2,140t	supernova ν burst
	22,000t	1,040t	proton decay
	22,000t	680t	solar ν
Thickness of anticounter	2m	1.2m∼1.5m	
Number of PMTs	11,200	948	inner detector
	1,867	123	anticounter
Photosensitive coverage	40%	20%	
PMT timing resolution	2.5nsec	4nsec	at 1 photoelectron
Energy resolution	$2.6\%/\sqrt{E}$	$3.6\%/\sqrt{E}$	e of E(GeV)
	2.5%	4%	$\mu(\lesssim 1\text{GeV})$
	$16\%/\sqrt{E}$	$20\%/\sqrt{E}$	e($\lesssim$20MeV)
Position resolution	50cm	110cm	10MeV
	∼10cm	15cm	$p \leftarrow e^+\pi^0$
Angular resolution	28°	28°	10MeV
	∼ 1°	∼ 2°	Through-going μ
E_{th}(trigger)	4∼5MeV	5.2MeV	
E_{th}(analysis)	5MeV	7.5MeV	solar ν
e/μ separation	99%	98±1%	0.03< p_e <1.33GeV/c
			0.2< p_μ <1.5GeV/c

Table 6.2: Performances of the Super-Kamiokande detector together with those of the on-going Kamiokande detector for comparison.

ure 6.17 shows the parent neutrino energy distributions of upward-stopping muons and upward through-going muons expected in Super-Kamiokande.

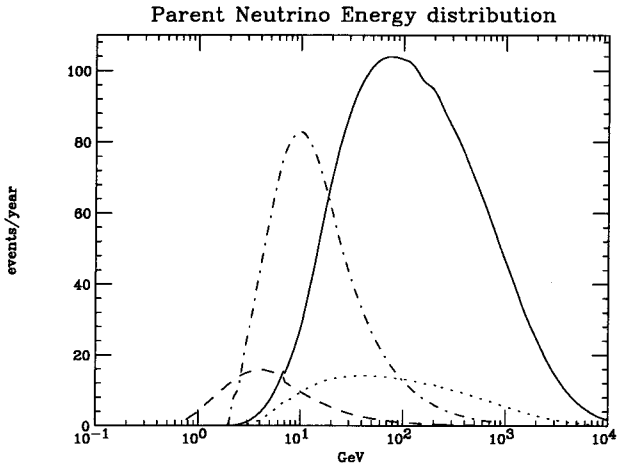

Figure 6.17: Parent neutrino energy distributions of upward-stopping muons and upward through-going muons in Super-Kamiokande and Kamiokande. The dot-dashed, solid, dashed and dotted line correspond to upward-stopping and upward through-going muons in Super-Kamiokande, upward-stopping and upward through-going muons in the Kamiokande, respectively.

The minimum track length for both upward-stopping and upward through-going muons is also set to 7 m. Accordingly, the nominal parent neutrino energy of upward-stopping muons in Super-Kamiokande is ~10GeV and that of upward through-going muons is ~80 GeV. At these energies, deep-inelasitic scattering (DIS) cross section (the main mechanism of the muon production) is well measured by ν-beam experiments [61]. The contributions of the quasi-elastic reaction ($\nu_\mu N \rightarrow \mu N'$), Δ production ($\nu N \rightarrow lN'\pi$) and other hadronic resonances are less than a few percent. On the other hand, in the case of Kamiokande, the minimum track length for upward-stopping muons was set to 1m (0.4 GeV), as one needs as much statistics as possible. However, the trade-off was a large uncertainty (~20 %) in the absolute value of neutrino-nucleon interaction cross sections due to the contributions of the quasi-elastic reaction, Δ production and other hadronic resonances. Therefore, even if the (upward-stopping muon)/(upward thorugh-going muon) ratio in Kamiokande is taken, the theoretical systematic error can not be reduced effectively.

In the Super-Kamiokande, the ratio calculated for various models are summarized in Table 6.3, and it is found

$$\frac{\text{Upward-stopping muon}}{\text{Upward through-going muon}} = 0.45 \pm 0.04(\text{theo.sys.})$$

The theoretical systematic error is evaluated to be ~9 %.

νflux \ σ_ν	EHLQ	Owens	CTEQ	MRS
Butkevitch	0.463	0.463	0.460	0.484
Gaisser	0.429	0.429	0.426	0.449
Lipari	0.417	0.417	0.414	0.436
Honda	0.457	0.456	0.453	0.476

Table 6.3: the expected (upward-stopping muon)/(upward through-going muon) ratio at the Super-Kamiokande.

When the $\nu_\mu \leftrightarrow \nu_\tau$ oscillation is taken into account, with the oscillation parameters $\Delta m^2 = 1.6 \times 10^{-2}\text{eV}^2$ and $\sin^2 2\theta_v$=1.0 (the best fitted neutrino oscillation parameters derived from contained event

analysis from Kamiokande), the expected ratio of (upward-stopping muon)/(upward through-going muon) is estimated as:

$$\frac{(\text{Upward-stopping muon})_{\text{osc}}}{(\text{Upward through-going muon})_{\text{osc}}} = 0.34 \pm 0.02(\text{stat})$$

taken over 3-year operation. The double ratio as defined below is found to be:

$$\frac{\left(\frac{\text{Upward-stopping muon}}{\text{Upward through-going muon}}\right)_{\text{osc}}}{\left(\frac{\text{Upward-stopping muon}}{\text{Upward through-going muon}}\right)_{\text{no-osc}}} = 0.76 \pm 0.08$$

Since this effect is 3σ deviation from unity, we can confirm possible neutrino oscillations suggested by Kamiokande, using Super-Kamiokande data, with better confidence.

6.5.3 Angular distribution of Upward-going muons in Super-Kamiokande

The angular distribution of the upward-going muons (stopping and through-going) with track length longer than 7 m is also useful to confirm the neutrino oscillations in Super-Kamiokande.

Figure 6.18 shows the angular distribution of upward-going muons normalized bin-by-bin with null oscillation. The points with solid error bars and dashed ones represent the Super-Kamiokande and Kamiokande for comparison under $\nu_\mu \leftrightarrow \nu_\tau$ oscillation assumption with $\Delta m^2 = 1.6 \times 10^{-2}\text{eV}^2$ and $\sin^2 2\theta_v$=1.0. These parameters are the best fitted values derived from the contained event analysis from Kamiokande. The theoretical systematic error and the statistical error expected during 5-year operation of the Super-Kamiokande detector are taken into account. After 5-year operation, the distortion in the zenith angle distribution will be more clearly observed than Kamiokande case.

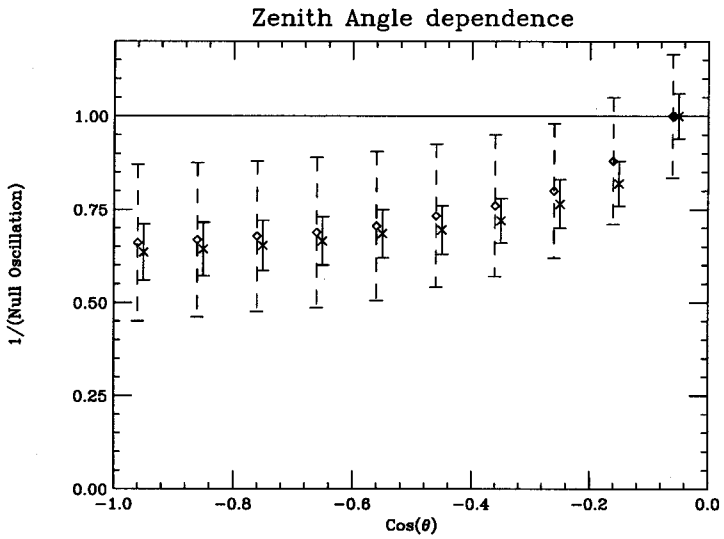

Figure 6.18: The angular distribution of the upward-going muons (through-going and stopping) with track length longer than 7 m. The points with solid error bar and dashed ones correspond to Super-Kamiokande and Kamiokande. The $\nu_\mu \leftrightarrow \nu_\tau$ oscillation cases is assumed. The oscillation parameters, Δm^2 and $\sin^2 2\theta_v$ are set to $1.6 \times 10^{-2}\mathrm{eV}^2$ and $\sin^2 2\theta_v$=1.0. The error bar includes the theoretical systematic error and the statistical error corresponding to 5-year detector operation time. These distribution are normalized bin-by-bin with null oscillation.

Chapter 7

Conclusion

The flux of the upward through-going muons produced (with its track length longer than 7 m) in the rock layers surrounding the detector by atmospheric neutrinos is measured by the Kamiokande detector. A total of 373 upward through-going muon events are observed, of which 185 events and 188 events are recorded during Kamiokande-II (1115 days) and Kamiokande-III (1332 days) experimental periods respectively.

The angular dependence of upward through-going muons is obtained. Using the observed differential flux, possible effects of neutrino oscillations are explored. We find that the zenith angle dependence of the upward through-going muons is consistent with neutrino oscillation assumptions (Honda's atmospheric neutrino flux and CTEQ parton distribution model are used). This result is consistent the previous Kamiokande-II result and strongly supports the "contained event" analysis from Kamiokande.

Furthermore, the measured average upward through-going muon flux is evaluated to be

$$\Phi_{obs} = (1.98 \pm 0.10(\text{stat}) \pm 0.03(\text{exp.sys})) \times 10^{-13}\text{cm}^{-2}\text{s}^{-1}\text{sr}^{-1}$$

This is compared with the expected flux calculation of

$$\Phi_{theo} = (2.20^{+0.39}_{-0.34}) \times 10^{-13}\text{cm}^{-2}\text{s}^{-1}\text{sr}^{-1}$$

The observed upward through-going muon flux is in apparent agreement with the expected flux within $\sim 1\sigma$ level. But it requires more studies to reduce the theoretical uncertainty.

Appendix A

Calibration and stability

The energy calibration is divided into two parts; relative and absolute. The relative energy calibration is to adjust the gain of each PMT relative to the average. The absolute energy calibration is to find the absolute energy scale (~/MeV). In this chapter, the methods of the energy calibration and the timing calibration are presented. A method of gain stability monitoring and attenuation length (of water in the detector) measurement will be also described.

A.1 Absolute Energy Calibration

The γ-rays emitted from thermal neutron capture of nickel is used for the absolute energy calibration for low-energy range (~10 MeV). Natural nickel, which mainly contains ^{58}Ni, ^{60}Ni and ^{62}Ni, is irradiated by neutrons from a ^{252}Cf, where the following reactions occur, namely, $^{58}\mathrm{Ni}(\mathrm{n},\gamma)^{59}\mathrm{Ni}^*$, $^{60}\mathrm{Ni}(\mathrm{n},\gamma)^{61}\mathrm{Ni}^*$ and $^{62}\mathrm{Ni}(\mathrm{n},\gamma)^{63}\mathrm{Ni}^*$. The properties of these reactions are listed in Table A.1

Reaction	Energy of the γ-ray (MeV)	Natural abundance of the initial element (%)	Cross section (barn)
$^{58}\mathrm{Ni}(\mathrm{n},\gamma)^{59}\mathrm{Ni}^*$	9.0	67.88	4.4
$^{60}\mathrm{Ni}(\mathrm{n},\gamma)^{61}\mathrm{Ni}^*$	7.8	26.23	2.6
$^{62}\mathrm{Ni}(\mathrm{n},\gamma)^{63}\mathrm{Ni}^*$	6.8	3.66 * 15	

Table A.1: Properties of $\mathrm{Ni}(\mathrm{n},\gamma)\mathrm{Ni}^*$ reactions [62].

From Table A.1, we see the fractional intensities of the emitted γ-ray are as follows:

$$9.0\mathrm{MeV} : 7.8\mathrm{MeV} : 6.8\mathrm{MeV} = 0.71 : 0.16 : 0.13$$

Figure A.1 shows a schematic view of the γ-ray source. A Ni-Cf source, which consists of a cylindrical hollow nickel can with 1 mm thickness which contains a ^{252}Cf sealed source, was used as the γ-ray source. The dimension of the nickel can is 9.5 cm in diameter and 16 cm in height, and it was hung from the ceiling at the several positions in the inner detecor.

The energy spectrum obtained by the Ni-Cf source is shown in Fig. A.2(a). The 9 MeV γ-ray peak is cleary seen above the background. The Ni-Cf source contains some backgrounds such as low energy gamma rays from spontaneous fission itself and from the p(n,γ)D reaction which emits 2.2 MeV

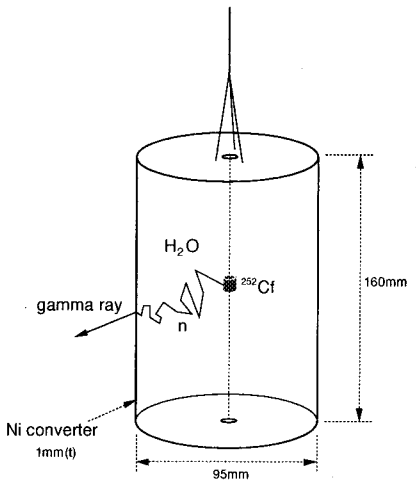

Figure A.1: Schematic view of Ni-Cf γ source.

monochromatic gamma rays. Therefore, data without the Ni converter were taken in order to subtract their contribution. The background spectrum is obtained from a Polyethylene-Cf run as shown in Fig. A.2(b).

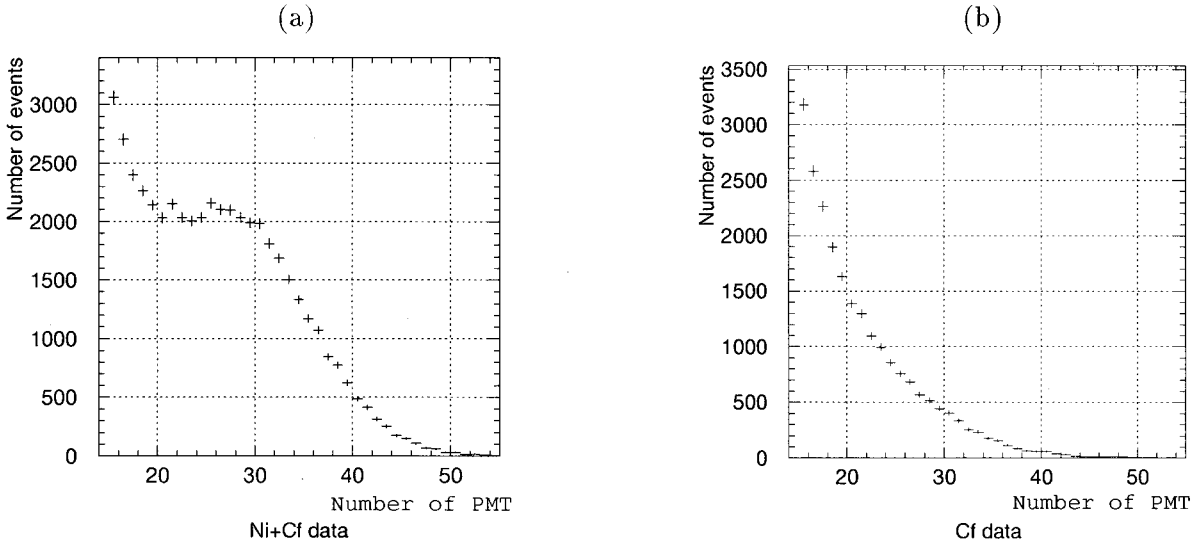

Figure A.2: Energy spectrum obtained by the Ni-Cf source. (a) and (b) corresponds to a Ni-Cf run and a Polyethylene-Cf run (background run), respectively.

After background subtraction, the 9 MeV γ-ray peak was compared with M.C. simulation.

Figure A.3 compares a typical spectrum of the real γ-ray (from Ni(n,γ)Ni*, denoted as crossed points) with the simulation (histogram). The uncertainty in the normalization of each run-time was estimated to be 2 %, which corresponds to 0.16 % of systematic error on the energy determination.

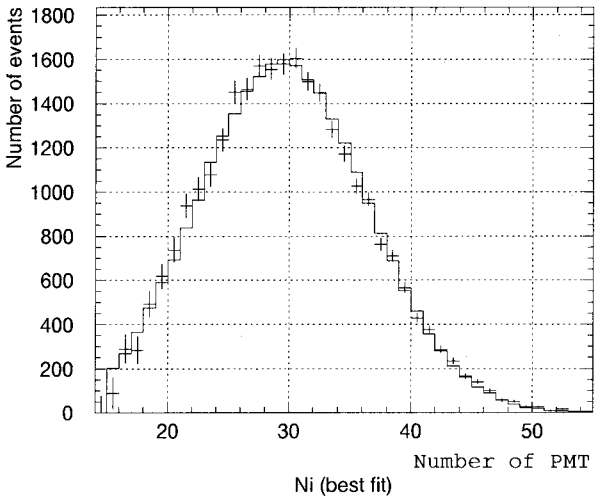

Figure A.3: Subtracted energy spectrum of the gamma rays from the reaction Ni(n,γ)Ni*. The cross points and histogram correspond to the real data and M.C. simulation, respectively.

A.2 PMT's Relative gain Adjustment

The uniformity of the gain of PMTs in the detector is necessary to preserve the isotropy of the detector. The absolute gain of all PMTs was adjusted to 3×10^6 before the installation. The PMT gain was increased to 6×10^6 on June 1988 during the Kamiokande II period. In order to adjust the absolute gain of PMTs, a suitable high voltage is supplied to each PMT.

An Ar flash lamp was used as the light source to monitor the long-term stability of the PMT gain. To obtain an isotropic light, the light is fed to a scintillator ball made of BBOT and MgO. A schematic diagram of the Ar-calibration system is shown in Fig. A.4.

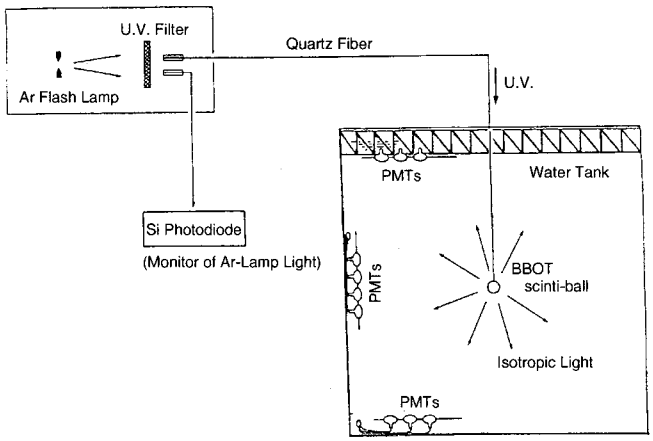

Figure A.4: Schematic view of the Ar-calibration system.

A spark gap was placed in the argon gas. Once a spark occurs, Argon gas is ionized and ultraviolet (U.V.) light is emitted. The light passing through an U.V. filter was injected into a scintillator ball via a 30 m long quartz fiber. The scintillator ball is made of acrylic resin in which 50 ppm BBOT and 500 ppm MgO powder are uniformly mixed. The BBOT and MgO were used as a wavelength shifter and a light diffuser, respectively. The wavelength spectrum of the isotropic light from the scintillator ball is shown in Fig. A.5. The intensity of the primary U.V. light is monitored by three Si photodiodes, and its temporal drift was only 0.8 % over more than 4 years.

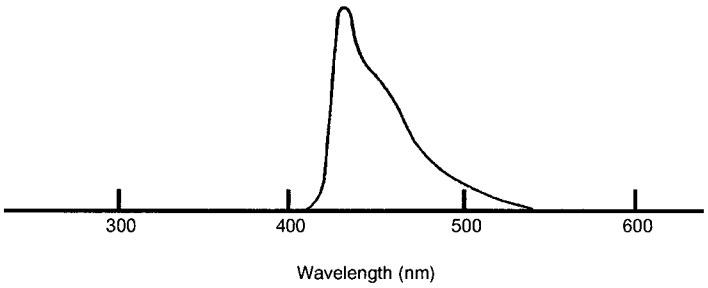

Figure A.5: Actual wavelength of emitted light from the scintillator ball.

The measured gain stability during the Kamionade II period was shown in Fig. A.6. The gains of PMTs were found to be stable to width ±3 %.

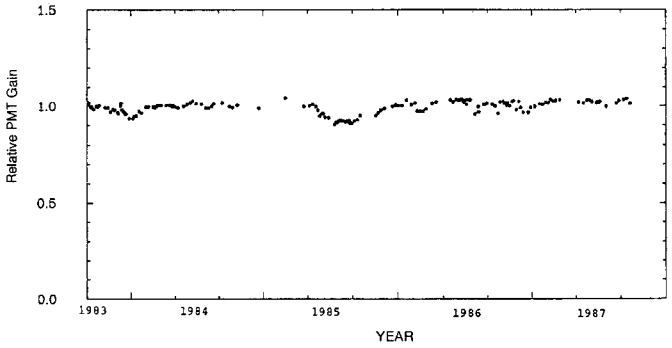

Figure A.6: Gain stability of 50 cm PMTs. Each point represents the mean gain of the 948 PMTs relative to the initial gain. These data are obtained from the scintillator ball runs.

It addition, in Kamiokande II the cosmic-ray muon data taken along with the normal runs enabled us to calibrate the gain fluctuation of PMTs and transparency of water. The study of long-term PMT gain stability by means of cosmic-ray muons is described in section A.4.

A.3 PMT's Relative timing Adjustment

Since the relative hit timing of each PMT is essential to reconstruct the muon track, it was measured with an accuracy of a few nano second. The channel-by-channel difference in relative timing originates from different transit time of PMTs, from different length of the signal cable of each PMT and from channel-dependent propagation time in electronics.

In order to measure the relative timing of each channel, an isotropic light source of which wavelength is similar to the Cherenkov light is required. Therefore, a nitrogen laser (N_2-laser) and an MgO diffuser were used for this purpose. A schematic view of the laser calibration system is shown in Fig. A.7.

The N_2-laser has a very narrow light pulse less than approximately 3 ns in width and its wavelength is 337 nm. The wavelength was converted by the BPBD365 dye from 337 nm into 366 nm at the peak value and 360-390 nm in width. The light pulse from the dye-laser was split into 2 beams by a quartz half mirror; one was for the trigger and the other was fed into a MgO diffuser via 70 m long quartz fiber. The

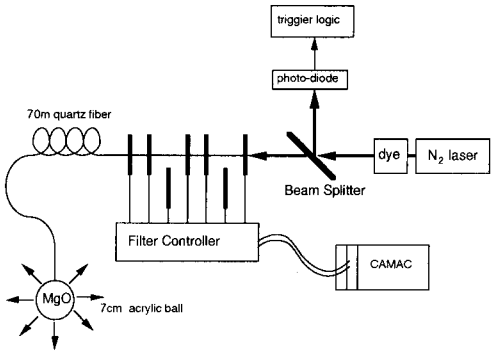

Figure A.7: Schematic view of the N_2-laser calibration system.

intensity of the pulse was adjusted to various levels in a calibration run by changing the filters between the beam splitter and the quartz fiber. The diffuser was placed at the center of the inner detector.

The time interval between a firing of the laser and the timing of the global trigger is common to all the PMTs. Thus, the relative time walk due to finite discriminator threshold and relative time bias of each PMT were measured by a laser run. The timing correction was performed so as to make the relative hit time of each PMT by a laser flash equal among all the channels. A typical data of the laser run is shown in Fig. A.8. The scatter plot in Fig. A.8 shows the timing variation as a function of pulse height for one electronics channel. A timing correction table, called T-Q maps, was made from the similar plots for each electronics channel.

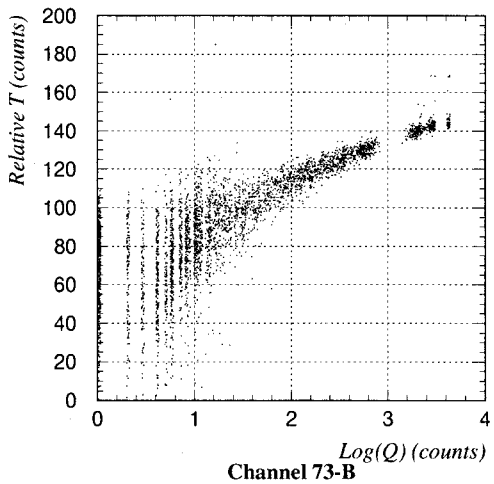

Figure A.8: Typical correlation between pulse height (Q) and timing (T) obtained from a laser run. This plot corresponds to the data of one PMT-electronics channel. The horizontal and vertical axes corresponds to log of the QAC count and relative TAC count, respectively, where the expected time of flight from the position of the diffuser to that of the PMT is subtracted. The offset of vertical axis is 2040-count.

A.4 Stability of Kamiokande III Detector

The long-term stabilities of the relative PMT gain and the attenuation length of the water was monitored by means of cosmic-ray muons which penetrate the detector. Since the event rate of cosmic-ray muons is stable, we can monitor the stabilities using the data from ordinary runs.

Since the number of Cherenkov photons emitted from a through-going cosmic-ray muon is proportional to its track length, the ratio of the total number of photoelectrons to the track length should be constant for each muon if the detector gain is stable. Figure A.9 shows the fluctuation of the PMT gain obtained

from the cosmic-ray muon events. From the Fig. A.9, it is proved that the relative gain is stable enough during Kamionade-III, because 5% change in the PMT gain will affect the detection efficiency for upward through-going muons (>1.7 GeV) by $\ll$1%. Therefore, the correction of relative PMT gain is not made in the upward through-going muon analysis.

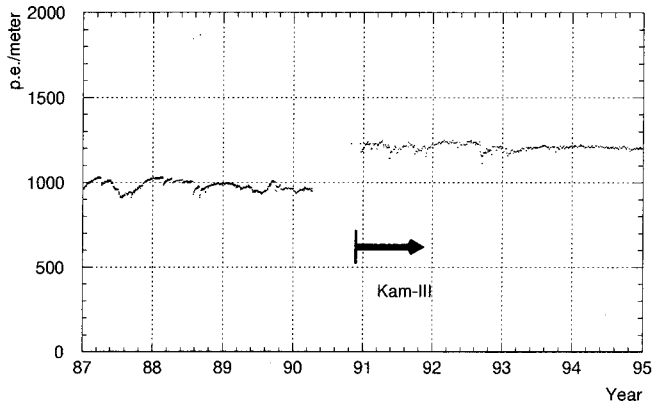

Figure A.9: Time-dependent fluctuation of the detector gain. This data are obtained from the cosmic-ray through-going muon events. The vertical axis corresponds to the relative fluctuation of the PMT gain.

The Cherenkov light attenuation length in the water is also monitored by means of cosmic-ray muon events. In the case of through-going muon events, the pulse height of the i-th PMT, Q_i, is represented as follows:

$$Q_i = A_i \times \frac{f(\theta_i)}{L_i} \times \exp(-\frac{L_i}{L_O}) \tag{A.1}$$

where A_i is a factor of the i-th PMT related with the PMT gain, $f(\theta_i)$ is the effective surface area of the photocathode as shown in Fig. A.11, L_i is the distance between the track of the muon and the i-th PMT (Fig. A.10), and L_O is the mean attenuation length of the Cherenkov light in water. Equation A.1 can be rewritten as

$$\log\left(\frac{Q_i L_i}{f(\theta_i)}\right) = -\frac{L_i}{L_O} + \log A_i \tag{A.2}$$

We obtained the Q_i and L_i from the cosmic-ray through-going muon data, and $f(\theta_i)$ from calculation. Equation A.2 indicates that $\log\left(\frac{Q_i L_i}{f(\theta_i)}\right)$ versus L_i should lie on a line as shown in Fig. A.12. The attenuation length was derived from the slope of Fig. A.12, and its time-dependent variation is shown in Fig. A.13. The observed mean attenuation length(55 m) is stable during the Kamiokande III operation. The resultant change in the detection efficiency is expected far less than 1 %, therefore, the correction of the water transparency was not included in analysis of upward through-going muons. The large dip in 1987 was due to introduction of sodiumhypoclorite into the detector water to kill bacteria.

The input parameter of the attenuation length for M.C. simulation is set to about 55m.

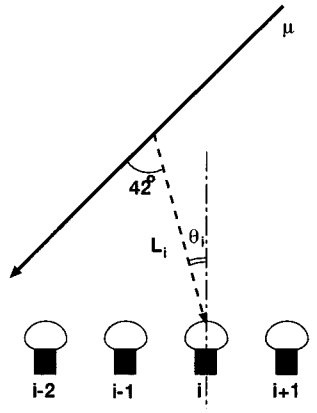

Figure A.10: Relation between i-th PMT and a muon.

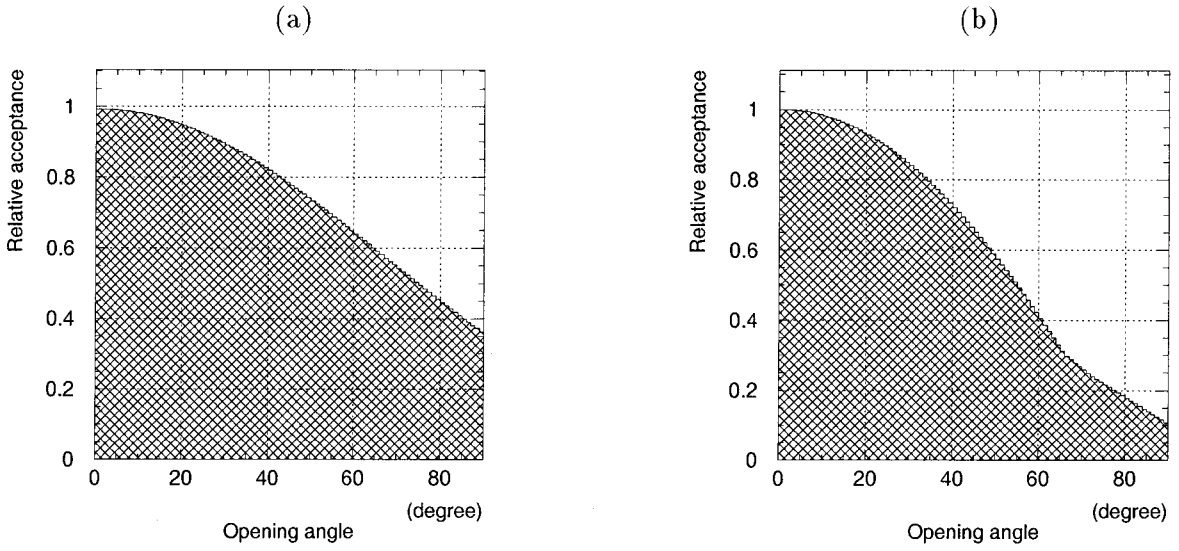

Figure A.11: Effective PMT surface as a function of angle between the incident photon and the PMT direction. (a) is for Kamiokande II and (b) is for Kamiokande III. The difference between (a) and (b) is due to the effect of the Al-PEP light reflector on the Kamiokande III PMT

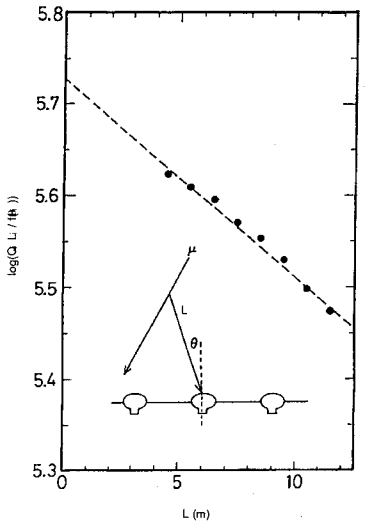

Figure A.12: Typical 2-dimensional plot of through-going muon events. The vertical and horizontal axes correspond to $\log\left(\frac{Q_i L_i}{f(\theta_i)}\right)$ and L_i, respectively. The dashed line is the best fit to the data points.

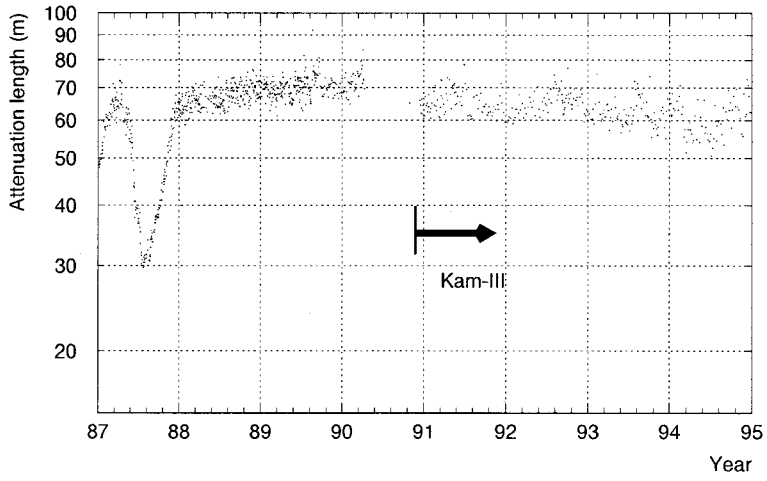

Figure A.13: Stability of the mean attenuation length of Cherenkov light in the inner detector water. The large dip in 1987 was due to introduction of sodiumhypocloryte into the detector water to kill bacteria.

Appendix B

Pre-reduction

Upward through-going muons are detected in Kamiokande III at a rate of ~1 event/week. On the other hand, the event rate of downward-going muons is 0.37 Hz and constitutes a overwhelming background against the upward-going muons. Though the muon direction can be determined by the method described in section 4.3, the process becomes much easier if the number of background is reduced in advance. In this chapter, the pre-"Muon direction cut" to reduce downward-going muons is introduced.

This pre-reduction is composed of two processes, "Fast muon fit" and "Point fit".

Fast muon fit

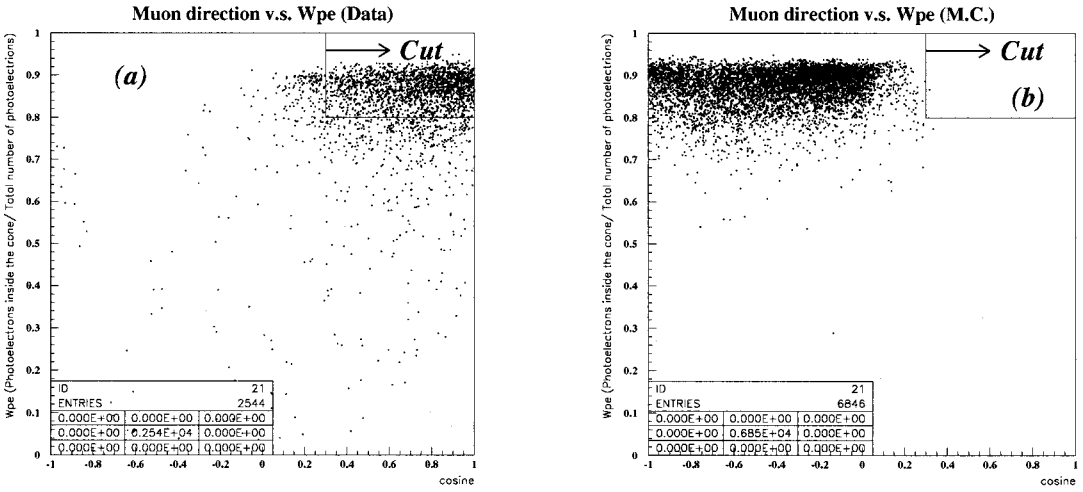

Figure B.1: (a) is the 2-dimensional plot of muon direction(zenith angle) v.s. W_{pe} for cosmic-ray downward through-going muons, where W_{pe} is defined as the ratio of the photoelectrons summed inside the Cherenkov cone to the total number of photoelectrons in an event. The muon direction is determined using the earliest firing PMT and the one with the maximum photoelectrons in an event. (b) is for the upward through-going muons generated by a Monte Carlo simulation.

When a muon enters the detector, the first Cherenkov photons usually hit PMTs near the muon entrance point. Therefore, the muon entrance point candidate is found out by searching for the earliest firing PMT. To eliminate PMTs fired by an accidental noise such as a dark pulse, a requirment is imposed

that at least one adjacent PMT should have signal within a time interval of 10 nsec. When a muon exits the detector, a large pulse height is recorded near the exit point (see Fig. 2.10). So the PMT which records the maximum number of photoelectrons in an event is assumed to be the exit point candidate. The direction of the muon can be crudely determined by connecting those entrance and exit position. Then we introduce W_{pe} as the ratio of the sum of the total number of photoelectrons inside the Cherenkov cone to the total number of photoelectrons deposited in the inner detector and Θ as the zenith angle ($\cos\Theta = 1$ corresponding to downward-going events). Figure B.1 shows the correlation between the fitted muon direction and the ratio W_{pe} of the cosmic-ray data and upward through-going muon Monte Cralo data, respectively.

The selction criteria for upward-going muons are set from this plot as follows;

(1) $W_{pe} < 0.8$

(2) $\cos\Theta < 0.3$

When the requirments (1) or (2) above are satisfied, they are saved. This criteria reject most of downward-going muons. The data reduction factor is $\sim 1/3$.

Point fit

To reduce the data more, one needs to have more accurate muon direction. This fitting algorithm, which we call "Point fit", was developed initially to reconstruct the interaction position of low-energy events.

The principle of the spatial reconstruction program using timing information of lit PMTs is to find out the interaction position by minimizing the timing residuals of t_i (difference between expected photon arrival time and the actual hit time t_i^0). It is defined as;

$$t_i = t_i^0 - \frac{n}{c} \times \sqrt{(x - x_i)^2 + (y - y_i)^2 + (z - z_i)^2} - \langle t \rangle \tag{B.1}$$

where

t_i^0	:	firing time of the i-th PMT
n	:	refractive index of water (=1.334)
c	:	light velocity
(x_i, y_i, z_i)	:	position of th i-th PMT
(x, y, z)	:	interaction position
$\langle t \rangle$	:	mean value of t_i

If the point (x, y, z) gives the correct interaction position, the timing residuals should give a sharp peak as shown in Fig. B.2. On the other hand, if it gives a wrong interaction position, a corresponding histogram will look more like Fig. B.3. The goal of the spatial reconstruction is to find out the vertex position which makes the timing residual histogram the sharpest.

The finite peak width in Fig. B.2 is due to the finite timing resolution of the PMTs which depends on the number of photoelectrons recorded by each PMT. The long tail in the histogram is due to the scattering Cherenkov photons in the water. In fact, the PMTs inside the Cherenkov ring count direct photons and the PMTs outside it count scattered photons. However, it is assumed that all photons are emitted from an interaction position.

The estimator indicating the *goodness*, G, of the fitting is defined as follows:

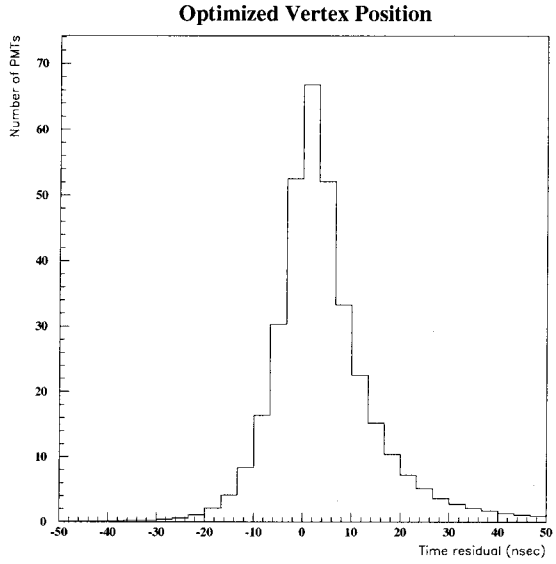

Figure B.2: Time residual histogram for a typical event after optimization of the vertex position. The tail in the histogram is due to the scattering of the Cherenkov photons in the water

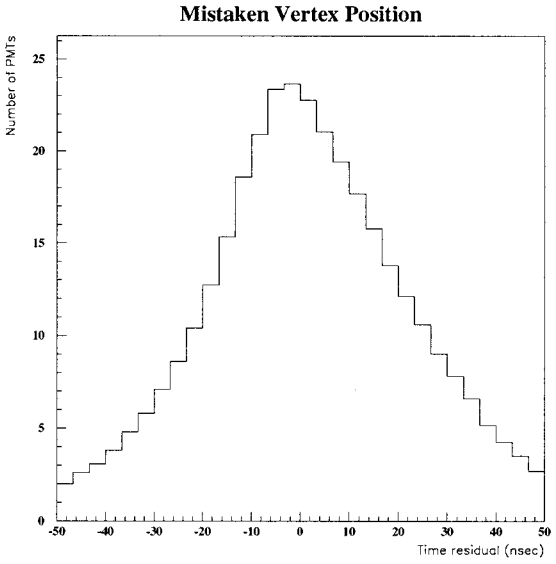

Figure B.3: Time residual histogram for a typical event in the case of a mistaken vertex position

$$G = \frac{\sum_i \frac{1}{\sigma_i^2} \exp\left(-\frac{(t_i - \langle t \rangle)^2}{2 \cdot (\langle \sigma \rangle \cdot factor)^2}\right)}{\sum_i \frac{1}{\sigma_i^2}}, \text{with} \quad factor = 1.5 \tag{B.2}$$

where σ_i is the timing resolution of the i-th PMT as a function of its photoelectrons recorded, and $\langle \sigma \rangle$ is the average of σ_i. $\Sigma_i \frac{1}{\sigma_i^2}$ normalizes the range of G from 0 to 1. For the inside PMT's, ones located in the long tail of the timing residual distribution are neglected with an effective cut-off of $\sim 3\sigma$ represented by the $factor = 1.5$. On the other hand, if the i-th PMT is tagged as outside of a Cherenkov ring with $t_i > \langle t \rangle$, the effect of scattered light is taken into account in G as a long exponential tail in the timing residual distribution. The timing distribution of scattered light is calculated based on the Monte Carlo simulation.

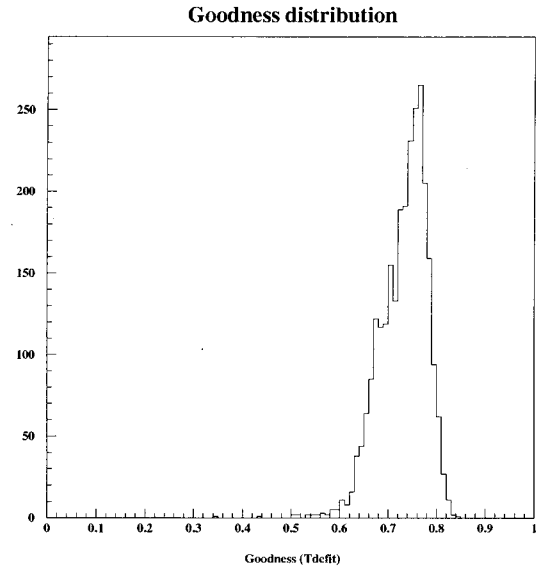

Figure B.4: Goodness using all PMT's information

The goodness distribution of cosmic-ray downward-going muons data is presented in Fig. B.4. Its value is mostly larger than 0.4. On the other hand, the goodness of electric noise events distributes in the region less than 0.4, so we can eliminate such noisy events by the following selection criteria;

$$G \geq 0.4$$

Once the vertex position is determined, the next step is to determine the muon direction. The vertex position found by the Point-fit is defined as $\vec{V}$ and is considered as the entrance position of the muon. The exit position denoted $\vec{C}$ of the muon is assumed to be the center of the Cherenkov ring, which is initially estimated by the average of the hit PMT positions weighted by the number of photoelectrons recorded by each PMT. So the initial muon track direction, $\vec{D}_0$, can be written,

$$\vec{D}_0 = \frac{\vec{C} - \vec{V}}{|\vec{C} - \vec{V}|} \tag{B.3}$$

A coarse fit starts, based on the initial condition given above, where, the muon velocity β is fixed to 1. The exit position is moved successively until the summed photoelectrons inside the assumed Cherenkov cone reaches the maximum.

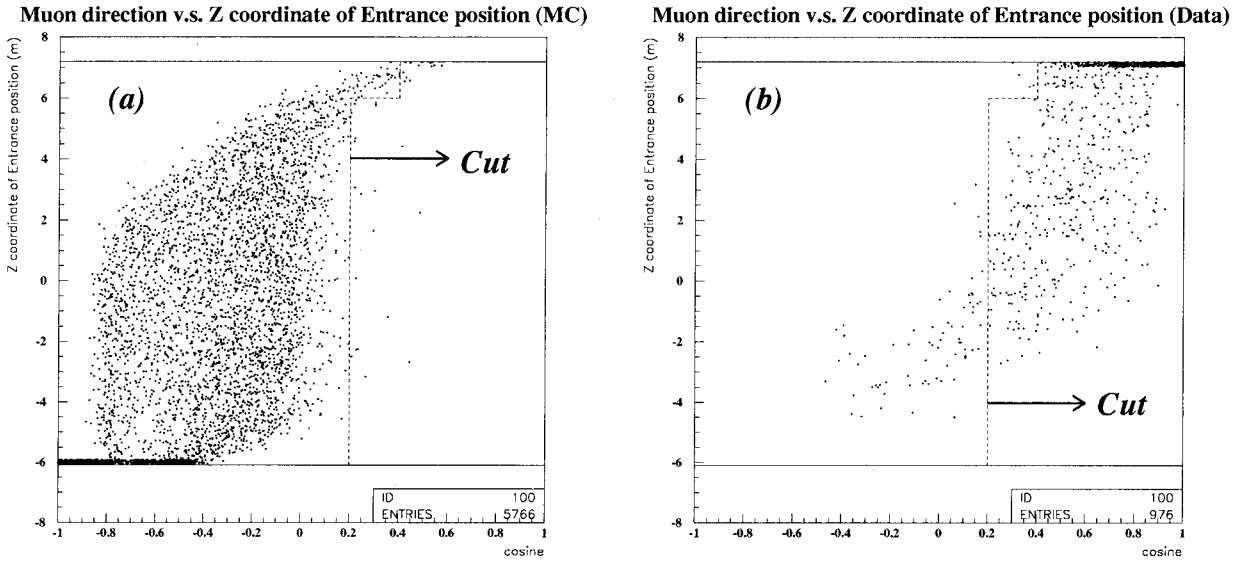

Figure B.5: (a) is the fitted direction v.s. Z component of the entrance position (Monte Carlo upward through-going muons). The solid line stands for the detector height (Z_{top} = 7.14 m, Z_{bottom} = −5.94 m). (b) is for real data.

Figure B.5 show the correlation between the fitted direction and the Z-coordinate of the fitted entrance position of the Monte Carlo upward through-going muon events and of the real cosmic-ray downward through-going muon events, respectively.

The selection criteria for the upward through-going muons are chosen as follows,

$$\cos\Theta \leq 0.2 \qquad for Z < 6\ m \tag{B.4}$$

$$\cos\Theta \leq 0.4 \qquad for Z > 6\ m \tag{B.5}$$

where Θ is the angle between the nadir and the muon direction, and the Z coordinate of the entrance position. For the upward through-going muons with Z>6 m is that the calculated direction tends to be slightly "downward". About half of the Cherenkov pattern of these muons are recorded on the top plane of the inner detector. The initial exit position is calculated to lower than the real one, for Z component is limitted to 7.14 m. In the succeeding grid search for mximum number of photoelectrons inside the assumed Cherenkov cone, the exit position is captured at the local maximum near the initial one.

To avoid this effect, a looser cut is adopted in this case.

By a Monte Carlo study, the survival efficiency through this pre-reduction step is estimated to be 97.7 % for upward through-going muons, and the reduction factor for the raw data is typically 1 %.

Appendix C

Monte Carlo simulation

The procedure of the Monte Carlo simulation is divided into two parts, one is the neutrino-induced muon generation process and the other is the simulation of the generated muon inside the detector. In this chapter, these Monte Carlo simulation processes are presented.

C.1 Neutrino-induced muon simulation

An upward through-going muon is produced via charged current neutrino-nucleon interaction uniformly in the Earth. Because the maximum energy of parent neutrinos producing upward through-going muons is $\sim 10^4$ GeV (see the dotted line in Fig. 6.17), the maximum energy of induced muons is less than this. So, the maximum distance from the muon production position to the detector is ~10 km, However, muons produced farther than 2 km have negligible probability of arriving at the detector. Therefore, the production points are randomly generated only within a sphere of radius 2 km centered at the detector location. The neutrino energy and direction are decided according to Fig. C.1 and C.2, respectively. Figure C.1 shows the (Atmospheric neutrino flux(Honda))×(Cross section(CTEQ)) as a function of neutrino energy. The angular distribution of atmospheric neutrinos is shown in Fig. C.2.

Once the neutrino energy is determined, the energy of the muon which is induced via νN interaction is determined according to the y[1] distribution as shown in Fig. C.3. The production angle between the neutrino and the muon is generated using Eq. 5.3 and 5.4.

If the muon ranges out before reaching the detector or does not hit the detector, this event is abandoned and the steps described above are iterated. In this way, the vector of the muon momentum and the entrance position at the detector are determined.

After entering the detector, muon track generation program including three physical processes (ionization loss, multiple Coulomb scattering and knock-on electron process) traces the muon which emits Cherenkov light photons. Since other processes such as pair production, bremsstrahlung and nuclear interaction are found to be negligible, they are not included. When an knock on occurs, subsequent shower development was simulated by EGS[2]. The more detail description of the detector simulation is presented in [6].

[1] Bjorken scaling parameter discussed in Section 3.3.

[2] Standard electromagnetic shower simulation program.

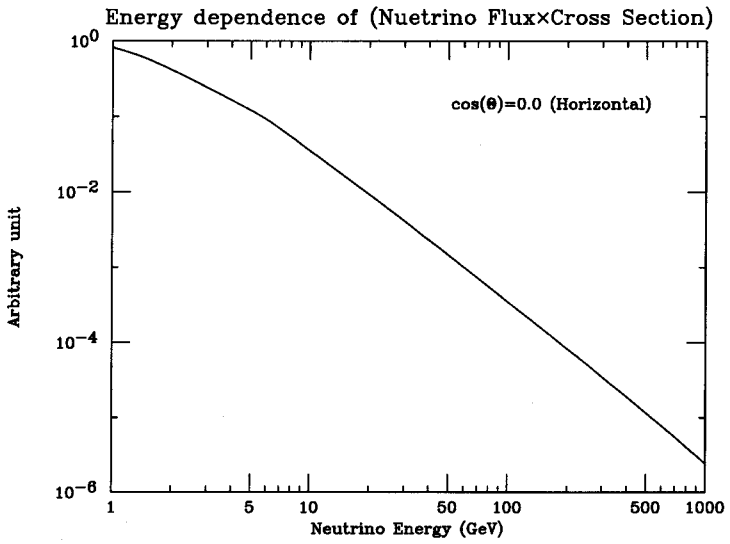

Figure C.1: Energy dependence of (Nuetrino Flux (Honda) × Cross Section(CTEQ)). The solid line correponds to $\nu_\mu + \overline{\nu}_\mu$.

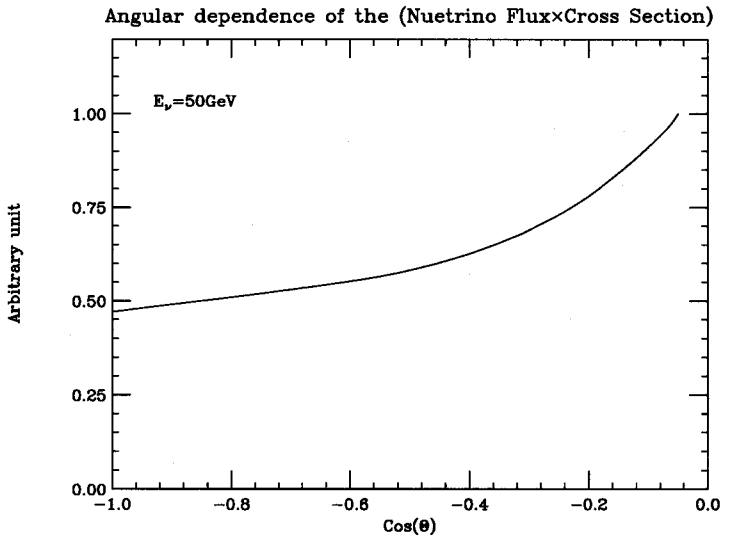

Figure C.2: Angular dependence of the (Nuetrino Flux (Honda) × Cross Section(CTEQ)).The solid line correponds to $\nu_\mu + \overline{\nu}_\mu$.

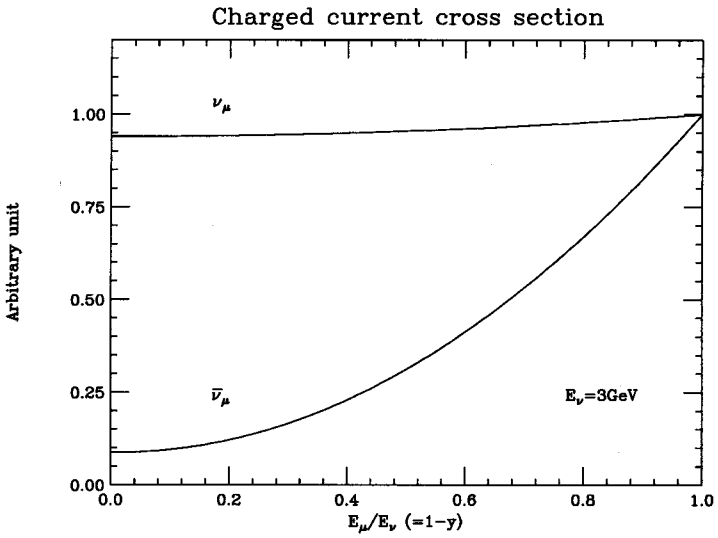

Figure C.3: Charged current cross section as a function of $E_\mu/E_\nu(=1-y)$, y is a Bjorken parameter.

Bibliography

[1] P.Lipari, Astroparticle Phys. 1(1993)195.

[2] M.Honda et al., ICRR-Report-336-95-2(1995), to be published in Phys. Rev. D

[3] T.K.Gaisser, M.Honda, K.Kasahara, H.Lee, S.Midorikawa, V.Naumov and Todor Stanev, Phys. Rev. D54(1996)5578.

[4] M.Kawasaki and S.Mizuta, Phys. Rev. D43(1991)2900.

[5] K.S.Hirata et al., Phys. Lett. B205(1988)416.

[6] M.Takita, Ph. D. thesis, Fac. of Science, Univ. of Tokyo(1989), ICR-Report-186-89-3.

[7] D.Casper et al., Phys. Rev. Lett. 66(1991)2561.

[8] R.Becker-Szendy et al., Phys. Rev. D46(1992)3720.

[9] T.Kafka Talk at the TAUP 93 Conf., Gran Sasso, Sep.1993.

[10] Ch.Berger et al., Phys. Lett. B227(1989)489.

[11] N.Aglietta et al., Europhys. Lett. 8(1989)611.

[12] Y.Fukuda et al., Phys. Lett. B335(1994)237.

[13] C.Weinheimer, et al., Phys. Lett. B300(1993)210.

[14] K.Assamagan, et al., Phys. Rev. D53(1996)6065.

[15] Aleph Collaboration, D.Buskulic et al. Phys. Lett. B349(1995)238.

[16] M.Kobayashi and K.Maskawa, Prog. Theor. Phys. 49(1973)652.

[17] Z.Maki, M.Nakagawa and S.Sakata, Prog. Theor. Phys. 28(1962)870.

[18] B.Pontecorvo, Sov. Phys. JETP 26(1968)984.

[19] L.Wolfenstein, Phys. Rev. D17(1978)2369.

[20] S.P.Mikheyev and A.Yu.Smirnov, Sov. J. Nucl. Phys 42(1985)913.

[21] G.Zaceck et al., Phys. Rev. D34(1986)2621.

[22] L.Borodovsky et al., Phys. Rev. Lett. 68(1992)274.

[23] L.A.Ahrens et al., Phys. Rev. D31(1985)2732.

[24] V.V.Ammosov et al., Z. Phys. C40(1988)487.

[25] L.S.Durkin et al., Phys. Rev. Lett. 61(1988)1811.

[26] C.Angelini et al., Phys. Lett. B179(1986)307.

[27] R.Divis, Prog. Part. Nucl. Phys. 32(1994)13.

[28] Gallex Collaboration, P.Anselmann et al., Phys. Lett. B327(1994)377.

[29] J.N.Abdurashitov et al., Phys. Lett. B328(1994)234.

[30] Y.Takeuchi, Ph. D. thesis, Tokyo Institute of Technology(1995), TIT-HEP-95-01.

[31] F.Dydak et al., Phys. Lett. B134(1984)281.

[32] F.Bergsma et al., Phys. Lett. B142(1984)103.

[33] N.Ushida et al., Phys. Rev. Lett. 57(1986)2897.

[34] I.Frank and I.Tam, C. R. Acad. Sci. USSR14(1937)109.

[35] K.Arisaka et al., J. Phys. Soc. Jpn. 54(1985)3213 ; Arisak K, Ph. D thesis, Fac. of Science, Univ. of Tokyo(1985), UT-ICEPP-85-01.

[36] T.Kajita et al., J. Phys. Soc. Jpn. 55(1986)711 ; Kajita T, Ph. D thesis, Fac. of Science, Univ. of Tokyo(1996), UT-ICEPP-86-03.

[37] M.Nakahata, Ph. D thesis, Fac. of Science, Univ. of Tokyo(1988), UT-ICEPP-88-01.

[38] J.N.Bahcall and R.K.Ulrich, Rev. of Mod. Phys. 60(1988)297.

[39] K.S.Hirata et al., Phys. Rev. Lett. 58(1987)1490 ; K.S.Hirata et al., Phys. Rev. D38(1988)448.

[40] R.M.Bionta et al., Phys. Rev. Lett. 58(1987)1494.

[41] W.Zhang et al., Phys. Rev. Lett. 61(1988)385.

[42] K.S.Hirata et al., Phys. Rev. Lett. 63(1989)16.

[43] K.S.Hirata et al., Phys. Rev. D44(1991)2241.

[44] A.V.Butkevitch, L.G.Dedenko and I.M.Zhelenznykh, Yad. Fiz. 50(1989)90 [Sov. J. Nucl. Phys. 50(1989)142].

[45] T.K.Gaisser, private communication (1993).

[46] E.Eichten E. et al., Rev. Mod. Phys. 56(1984)579 ; ibid. 58(1986)1065 (Erratum).

[47] J.F.Owens., Phys. Lett. B266(1991)126.

[48] J.Botts et al., Phys. Lett. B304(1993)159. ; Lai H.L. et al., Phys. Rev. D51(1995)4763.

[49] A.D.Martin, W.J.Stirling and R.G.Roberts, Phys. Rev. D51(1995)4756 ; A.D.Martin, R.G.Roberts and W.J.Stirling, Rutherford Preprint RAL-95-021(1995).

[50] Particle Data Group, K.Hikasa et al., Phys. Rev. D45(1992)III.82.

[51] W.Lohmann, R.Kopp and R.Voss, CERN Report No. 85-03(1985)(unpublished).

[52] F.James, CERN Program Library Long Writeup D506. "MINUIT" Function Minimization and Error Analysis, Reference Manual.

[53] Y.Oyama, Ph. D thesis, Fac. of Science, Univ. of Tokyo(1989), ICR-Report-193-89-10.

[54] V.S.Berezenskii, C.Castagnoli and P.Galeotti, Nuovo Cimento C, 8(1985)185.

[55] M.Mori et al., Phys. Lett. B270(1991)89.

[56] K.Gabathuler et al., Phys. Lett. B134(1984)449.

[57] P.Lipari, M.Lusignoli and F.Sartogo, Phys. Rev. Lett 74(1995)4384.

[58] R.Becker-Szendy et al., Phys. Rev. Lett. 69(1992)1010.

[59] M.M.Boliev et al., Proc.of the 3rd International Conf. on Neutrino Telescope, Venice, Italy, Ed. Baldo Ceolin M,p.235, 1991.

[60] D.G.Michael (MACRO Collaboration) Conference on High Energy Physics, Glasgow, UK, 20-27 July 1994 p.961.

[61] D.B.McFarlane et al. Z. Phys. C26(1984)1.

[62] G.A.Bartholomew et al., Nucl. Data A3(1967)367.

List of Figures

List of Tables